UNIVERSITY OF OKLAHOMA

GRADUATE COLLEGE

DETERMINATION OF S_{Hmax} USING DRILLING INDUCED FRACTURES AND FOCAL MECHANISM

A THESIS

SUBMITTED TO THE GRADUATE FACULTY

in partial fulfillment of the requirements for the

Degree of

MASTER OF SCIENCE

By

YUAN FANG
Norman, Oklahoma
2023

DETERMINATION OF S_{Hmax} USING DRILLING INDUCED FRACTURES AND FOCAL MECHANISM

A THESIS APPROVED FOR THE
MEWBOURNE SCHOOL OF PETROLEUM AND GEOLOGICAL ENGINEERING

BY THE COMMITTEE CONSISTING OF

Dr. Ahmad Ghassemi, Chair

Dr. Zhi Ye

Dr. Mashhad Fahes

ACKNOWLEDGEMENTS

I would like to express my gratitude to Dr. Ghassemi and Dr. Ye who guided me through my graduate studies at The University of Oklahoma. Dr. Ghassemi trusted me and accepted me as a graduate research student and Dr. Ye provided crucial assistance in the completion of my research projects.

I would also like to thank my family who had supported me to complete both of my bachelor's and master's degrees in the United States. They are my greatest guidance and source of wisdom.

Also, thanks to all my colleagues and friends who supported and helped me to make my journey straightforward and full of life.

Finally, I would like to thank the staff and faculties in the University of Oklahoma and the Mewbourne School of Geological and Petroleum Engineering for providing me with all the assistance and resources for me to become successful.

Yuan Fang

Table of Contents

ABSTRACT

Knowledge of in-situ stress is essential to well development technologies such as wellbore stability, hydraulic fracturing, well spacing design, and the monitoring of induced seismicity. As energy exploration has become more prevalent in unconventional reservoirs and as it has shifted focus to sustainable energy such as geothermal energy, the knowledge of in situ stresses plays a crucial role in the success of energy production. In this project, the in-situ stress S_{Hmax} in the geothermal reservoir of Utah FORGE is computed and analyzed using multiple stress analysis methodologies in both vertical and horizontal wells.

In a stress analysis, the understanding of three principal stresses is needed and they are vertical stress (S_v), minimum horizontal principal stress (S_{hmin}), and maximum horizontal principal stress (S_{Hmax}). In general, S_v is calculated by integrating the density log over the depth, while S_{hmin} is determined by hydraulic fracturing-based tests such as DFIT, leak-off test, and micro frac test. The direction of S_{hmin} and S_{Hmax} can be interpreted from the azimuth of drilling induced fractures and/or borehole breakouts. However, the determination of the magnitude of maximum horizontal principal stress (S_{Hmax}) is challenging especially in an inclined wellbore. Traditionally, S_{Hmax} can be estimated using hydraulic fracturing data and the Kirsch solution. However, this method of using hydraulic fracturing data imposes uncertainties as it is sensitive to the models and the assumption to rock formation is too sample (Schmitt and Zoback, 1989; Zi et al., 2022). With the gaining use of image log tools such as FMI and UBI, the method of using borehole failures such as breakouts and drilling induced fractures gives rise to more access to assess in situ stresses (Zoback, et al., 2003). Thus, the need of integrating multiple stress analysis methods and the incorporation of drilling induced fractures and breakouts around the wellbore is required to constrain a more comprehensive S_{Hmax} magnitude estimation.

In this paper, we present the wellbore in-situ stress models of the vertical and deviated wells in Utah FORGE based on the drilling-induced fractures and breakouts observed from borehole image logs. We also applied an in-situ stress inversion program based on focal mechanism and validated the program using the data from the Geyser geothermal reservoirs. This program can be used for the Utah FORGE reservoir once its focal mechanism data is available.

In Utah FOREG, we integrated multiple methods such as fracture mechanics, and wellbore failure analysis with the incorporation of drilling-induced fractures, borehole breakouts, and thermal stresses to constrain the wellbore stress model and input parameters. The validated wellbore in-situ stress models and parameters were then applied to establish the in-situ stress profiles of wells. The stress results in all wells yield a range of S_{Hmax} of 0.80 – 1.05 psi/ft, suggesting a normal faulting regime in Utah FORGE. The orientation of S_{Hmax} has a range of N20E to N40E with a mean of N33E based on drilling induced fractures in vertical wells.

In Geyser, an in-situ stress inversion program based on the focal mechanism has been applied and validated. The stress variation analysis confirmed that the Geyser reservoir has a mixture of normal and strike-slip fault regimes sandwiched by strike-slip fault regimes on the top and bottom of the reservoir. The Geyser injection test also was shown to alter the stress regimes of the reservoir and cause the stress regime to transit from strike slip to normal and to transtensional fault during a cycle of injection activities.

INTRODUCTION

EGS AND UTAH FORGE RESERVOIR

The increasing demand for cleaner energy and the quest for transition to renewable energy has led to the thriving of geothermal energy development. Geothermal technology is a cutting-edge technology to extract hydrothermal energy from the "hot dry rock" (HDR) reservoirs. The "hot dry rock" reservoirs are characterized by high temperature, deep depth, and dry and impermeable formation. These natural conditions of hot dry rock are called enhanced geothermal systems (EGS). EGS reservoirs offer to bring low permeability HDR reservoirs into economic geothermal reservoirs by conducting hydraulic fracturing stimulation. There are more EGS resources in the world than conventional recourse and EGS reservoir can potentially bring geothermal resources to its greatest deployment. However, EGS reservoir requires advanced technology in drilling, reservoir characterization, monitoring, hydraulic fracturing stimulation, etc. to be able to be commercially available (Podgorney et al., 2021). In the U.S., the U.S. Department of Energy has funded EGS projects such as the Desert Peak in Nevada and the Geysers in Northern California. The Frontier Observatory for Research in Geothermal Energy (FORGE) site in Utah is a currently funded geothermal project, where EGS technology is being studied and developed to allow hydrothermal energy to become economically profitable.

Utah FORGE is located near Milford in Beaver County, Utah. FORGE geothermal reservoir consists of low permeable crystalline rocks (granite) and is naturally fractured. The preferable drilling target is the formation with a temperature range of 448 to 498 K, and the reservoir is about 5.4 ft^2 in area and is 6 to 10 ft into the granite which is about 660 ft to 2000 ft below the surface (Allis et al. 2016). In EGS reservoir Utah FORGE, stimulation such as hydraulic fracturing in the reservoir is required to produce more permeability and increase hydrothermal productivity. Hydraulic fracturing often needs the knowledge of in situ stresses such as S_v, S_{Hmax} and S_{hmin}. In

FORGE, using hydraulic fracturing data, drilling data, well logs data, and the observation of drilling induced fractures, the in-situ stresses profile can be successfully established. In FORGE, there are 6 current wells, and they are 56-32, 58-32, 68-32, 78B-32, 78-32, and 16(A)78-32. 2 more new wells are planned to drill in the future. Horizontal well 16(A)78-32 is drilled in a total depth of 10,987 ft and is the deepest well in FORGE. 58-32 has a total depth of 7536 ft. 78B-32 is drilled to 9500 ft total depth. Well 56-32 has about 9145 ft in total depth (Utah FORGE). Among them, 4 wells have observed drilling induced fractures and they are the studying wells in this project since the drilling induced fractures are needed to establish S_{Hmax} estimation.

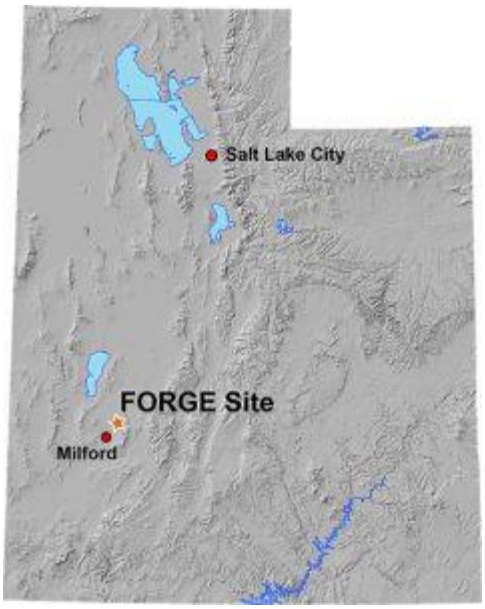

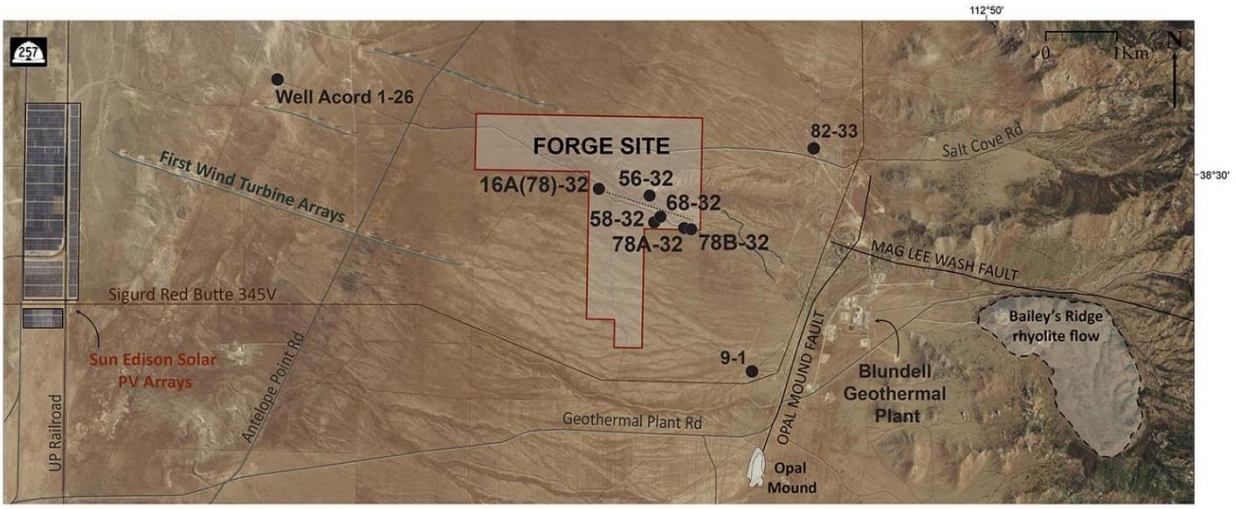

Fig. 1. a) The state of Utah and the location of FORGE site. b) the zoom in of FORGE site and location of each well (Utah FORGE).

S_{Hmax} STRESS CALCULATION

In-suit stress tensor usually consists of 3 orthogonal components, S_{hmin}, S_{Hmax}, and S_v. Vertical stress can be relatively reliably found from $\sigma_v=\rho g Z$, in which the density ρ is obtained from logs. S_{hmin} is determined using tests such as Leak of Test (LOT), Extended Leak-Off Test (XLOT), Diagnostic Fracture Injection Test (DFIT), and mini-frac test. They estimate minimum stresses by

creating fractures in the wellbore and using the instantaneous shut-in pressure (ISIP) or closure pressure to obtain the minimum horizontal stress. The other stress component, $\boldsymbol{S_{Hmax}}$, is challenging to estimate because it requires on set drilling induced fractures but not all well present such data. Even though with the availability of image logs, the measurement and interpretation of drilling induced fractures from image logs can be inaccurate and have uncertainties. Although the direction of S_{Hmax} can be found from breakout or drilling-induced cracks, its magnitude remains challenging to estimate.

In this report, multiple stress inversion methods are integrated to establish the best and most accurate in situ model for Utah FORGE. S_{Hmax} is estimated using observed drilling induced fractures (DIFs) and borehole breakouts. The methods used fracture mechanics method (Rummel, 1987; Zoback, and Peska, 1995), fracturing based Kirsch solution (Stephen and Voight, 1982), and breakout based S_{Hmax} determination (Barton et al.,1988). Lastly, S_{Hmax} estimation method based on the focal mechanism will be established by using a case study in Geyser's geothermal reservoir. S_{Hmax} can be estimated from stress inversion using focal mechanism data. This method requires the moment tensor from seismic events as input data.

VERTICAL WELLS

In vertical wells, two methods are used to determine the maximum principal stress (S_{Hmax}): drilling induced fractures (DIFs) and borehole breakouts. DIFs are analyzed using the Kirsch solution (Kirsch, 1898) and the fracture mechanics method (Rummel, 1987), while borehole breakouts are analyzed using a method developed by Barton et al. (1988) that is based on Kirsch's solution. In Utah FORGE, the analyzed vertical wells are 78B-32, 58-32, 56-32, and as well as the vertical section of the deviated well 16(A)78-32. There are 546 drilling induced fractures and 3 breakouts in well 78B-32. There are 295 DIFs in well 58-32 and 260 DIFs and 1 breakout in well

56-32. In the vertical section of 16(A)78-32, there are 26 observed drilling induced fractures. For DIFs data, we removed the fractures that have less than 75 degrees of fracture azimuths. Fracture azimuths that are less than 75 degrees has less reliable measurement because their orientation relative to true north is small and is pore to errors. Since the observed fractures have measurement and misinterpretation during logging and feature identification, it is intrinsic for fracture azimuth to possess uncertainties. However, fracture orientations with less than 75 degrees tend to have more uncertainties due to their small orientation and it can be more difficult to capture the accurate orientation of the fractures.

METHODOLOGY FOR S_{Hmax} ANALYSIS

Stress Around a Vertical Wellbore (Kirsch's Solution)

Kirsch's Solution describes the stresses around a wellbore in relation to the far field stresses and it also describes wellbore failure in terms of wellbore stresses. The equations in Eqs.1 through 6 describe the complete Kirsch solution. In general, Kirsch solution gives stresses in the axial (σ_{zz}), shear ($\sigma_{r\theta}$), radial (σ_{rr}), and tangential ($\sigma_{\theta\theta}$) directions for distance a in a wellbore. θ is measured counterclockwise from S_{Hmax} to the point of interest on the wellbore in a cylindrical coordinate. σ_x, σ_y, σ_z, σ_{xy}, σ_{yz}, σ_{zx} are six stress tensors components of in situ stresses and they are driven by rotating the principal stress tensor. The sign convention for the Kirsch solution is compression is positive and tensile is negative.

$$\sigma_{rr} = \frac{(\sigma_x+\sigma_y)}{2}\left(1-\frac{a^2}{r^2}\right) + \frac{(\sigma_x-\sigma_y)}{2}\left(1+3\frac{a^4}{r^4}-4\frac{a^2}{r^2}\right)\cos 2\theta + \tau_{xy}\left(1+3\frac{a^4}{r^4}-4\frac{a^2}{r^2}\right)\sin 2\theta + P_w\frac{a^2}{r^2} \quad \text{Eq. 1}$$

$$\sigma_{\theta\theta} = \frac{(\sigma_x+\sigma_y)}{2}\left(1+\frac{a^2}{r^2}\right) - \frac{(\sigma_x-\sigma_y)}{2}\left(1+3\frac{a^4}{r^4}\right)\cos 2\theta - \tau_{xy}\left(1+3\frac{a^4}{r^4}\right)\sin 2\theta - P_w\frac{a^2}{r^2} \quad \text{Eq. 2}$$

$$\sigma_{zz} = \sigma_z - \upsilon[2(\sigma_x-\sigma_y)\frac{a^2}{r^2}cos2\theta + 4\tau_{xy}\frac{a^2}{r^2}\sin 2\theta] \quad \text{Eq. 3}$$

$$\tau_{r\theta} = \frac{(\sigma_x - \sigma_y)}{2}\left(1 - 3\frac{a^4}{r^4} + 2\frac{a^2}{r^2}\right)\sin 2\theta + \tau_{xy}\left(1 - 3\frac{a^4}{r^4} + 2\frac{a^2}{r^2}\right)\cos 2\theta \quad \text{Eq. 4}$$

$$\tau_{\theta z} = \left(-\tau_{xz}\sin\theta + \tau_{yz}\cos\theta\right)\left(1 + \frac{a^2}{r^2}\right) \quad \text{Eq. 5}$$

$$\tau_{rz} = \left(\tau_{xz}\cos\theta + \tau_{yz}\sin\theta\right)\left(1 - \frac{a^2}{r^2}\right) \quad \text{Eq. 6}$$

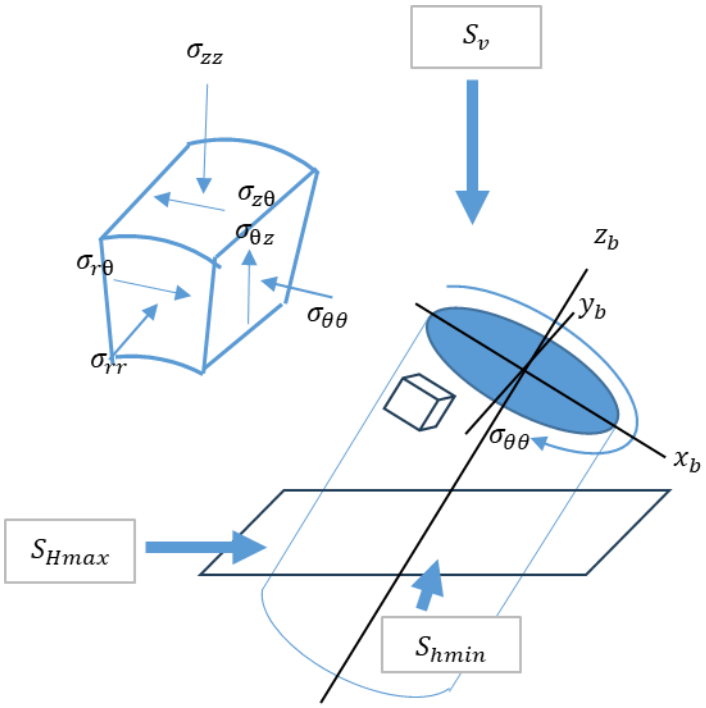

Fig. 2. An instruction of the relationship between in situ stresses and 6 wellbore stress components in cylindrical coordinates for Kirsch solution. S_{Hmax} and S_{hmin} are on the same horizontal plane and S_v is vertical.

When $r = a$, the equations simplify to Eq. 7. Pore pressure P_p is subtracted only from normal stress components to get effective stresses because effective stresses describe in-situ reservoir conditions (Eq. 8).

$$\begin{cases} \sigma_{rr} = P_w \\ \sigma_{\theta\theta} = \sigma_x + \sigma_y - 2(\sigma_x - \sigma_y)\cos 2\theta - 4\tau_{xy}\sin 2\theta - P_w \\ \sigma_{zz} = \sigma_z - 2\upsilon(\sigma_x - \sigma_y)cos2\theta - 4\upsilon\tau_{xy}\sin 2\theta \\ \tau_{r\theta} = 0 \\ \tau_{\theta z} = 2(-\tau_{xz}\sin\theta + \tau_{yz}\cos\theta) \\ \tau_{rz} = 0 \end{cases} \quad \text{Eq. 7}$$

$$\begin{cases} \sigma_{rr} = P_w - P_p \\ \sigma_{\theta\theta} = \sigma_x + \sigma_y - 2(\sigma_x - \sigma_y)\cos 2\theta - 4\tau_{xy}\sin 2\theta - (P_w - P_p) \\ \sigma_{zz} = \sigma_z - 2\upsilon(\sigma_x - \sigma_y)cos2\theta - 4\upsilon\tau_{xy}\,sin\,2\theta \\ \tau_{r\theta} = 0 \\ \tau_{\theta z} = 2(-\tau_{xz}\sin\theta + \tau_{yz}\cos\theta) \\ \tau_{rz} = 0 \end{cases} \quad \text{Eq. 8}$$

For a vertical well in the direction of the vertical principal direction, the shear stress components disappear, and the Kirsch solution further simplifies and becomes Eq. 9.

$$\begin{cases} \sigma_r(r=a) = P_w - P_p \\ \sigma_{zz}(r=a) = \sigma_v - 2v(\sigma_{Hmax} - \sigma_{hmin})\cos 2\theta \\ \sigma_{\theta\theta}(r=a) = \sigma_{Hmax} + \sigma_{hmin} - 2(\sigma_{Hmax} - \sigma_{hmin})\cos 2\theta - (P_w - P_p) \\ \tau_{r\theta} = \tau_{\theta z} = \tau_{rz} = 0 \end{cases} \quad \text{Eq. 9}$$

$$\sigma_{min} = \sigma_{\theta\theta}(r=a, \theta=0) = -\sigma_{Hmax} + 3\sigma_{hmin} - (P_w - P_p) \quad \text{Eq.10}$$

$$\sigma_{max} = \sigma_{\theta\theta}\left(r=a, \theta=\frac{\pi}{2}\right) = 3\sigma_{Hmax} - \sigma_{hmin} - (P_w - P_p) \quad \text{Eq. 11}$$

The stress field around the wellbore is only defined by tangential stresses and vertical stresses. Since drilling-induced fractures occur on the circumference of the wellbore, we are then only interested in tangential stress $\sigma_{\theta\theta}$ in Eqn. 9. This equation can be used to describe the occurrences of drilling-induced failure on a vertical wellbore and determine the direction of principal stresses.

Tensile fractures such as drilling induced fractures occur when the tensile stress is maximum. In Fig. 3, based on the sign convention that compression is positive and tensile is negative, maximum

tensile develops where tangential stress is at the minimum. The minimum tangential stress can be represented by Eq. 10 where θ is the angle measured from S_{Hmax} direction. The maximum tensile stress occurs in the direction of S_{Hmax}, so the tensile fracture is often in the direction of S_{Hmax}. On the other hand, breakout occurs when the compression is the maximum and it occurs when the tangential stress is the maximum. The maximum tangential stress is represented by Eq.11 and it occurs in the direction of S_{hmin}. So, the breakout axis is often in the direction of S_{hmin} (Gough and Bell, 1982; Fjær et al, 1992).

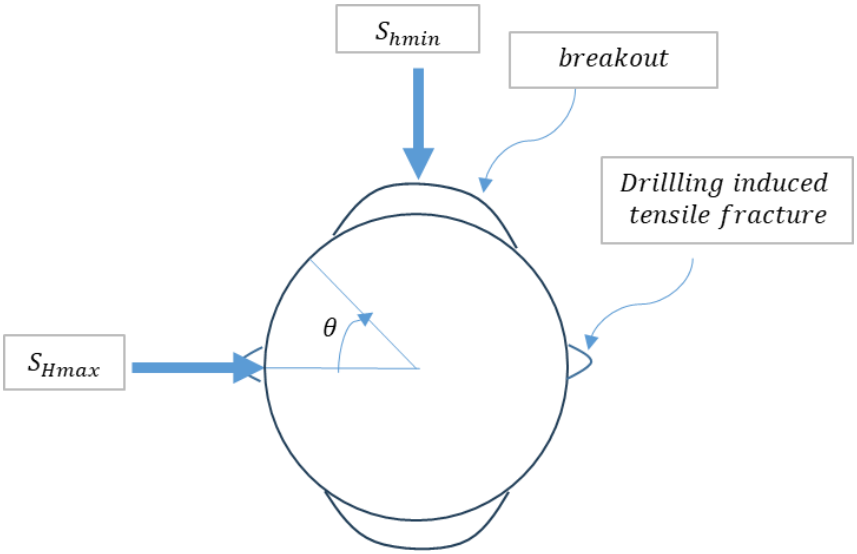

Fig. 3. This cartoon shows the wellbore stresses and their relationship with wellbore failures. Tensile fractures tend to occur parallel to S_{Hmax} where tensile stress on the wellbore is the maximum. Breakout tends to occur parallel to S_{hmin} where tensile stress is the minimum.

S_{Hmax} DIRECTION

The direction of S_{Hmax} can be found by using drilling included fractures such as breakout and drilling induced fractures. The breakout axis is the direction of S_{hmin} and drilling included fracture azimuth is the direction of S_{Hmax} . However, drilling induced fractures can only be an indicator of

the horizontal stress axis in a vertical wellbore. In a horizontal wellbore, principal stress in the vertical direction also contributes to the failure of the borehole and thus drilling induced fractures and breakouts cannot be used as indicators of horizontal principal directions.

In this work, drilling induced fractures azimuth in vertical wells of 78B-32, 56-32, and 58-32 and the vertical part of 16(A)78-32 are used to identify the orientation of the maximum horizontal stress. In the rose diagram below showing DIFs' azimuths, the majority of the azimuths are in the range of N20E to N40E degrees and have a mean value of N33E degrees. Thus, N33E is the proximate best S_{Hmax} azimuth based on the rose diagram. In the making of the rose diagram, Krumbein's mean is used to calculate the mean azimuth of S_{Hmax}, meaning the mean value treats fractures as non-directional significant and the rose diagram is symmetric, and the SW region is the reflection of the NE region. This means the mean value of 33 degrees is calculated only based on the azimuths in the NE region of the rose diagram (Allmendinger, 2020). This range also confirms with the S_{Hmax} range concluded from the study of Finnila and Podgorney (2020). They used drilling induced fractures in well 58-32 to estimate the S_{Hmax} orientation and their range is N10E to N40E and they recommended the best value of N25E (Finnila and Podgorney, 2020). Since their analysis of S_{Hmax} direction is solely based on the DIFs in well 58-32, their estimation might be less accurate than the estimation based on the DIFs from the 4 vertical wells in our analysis.

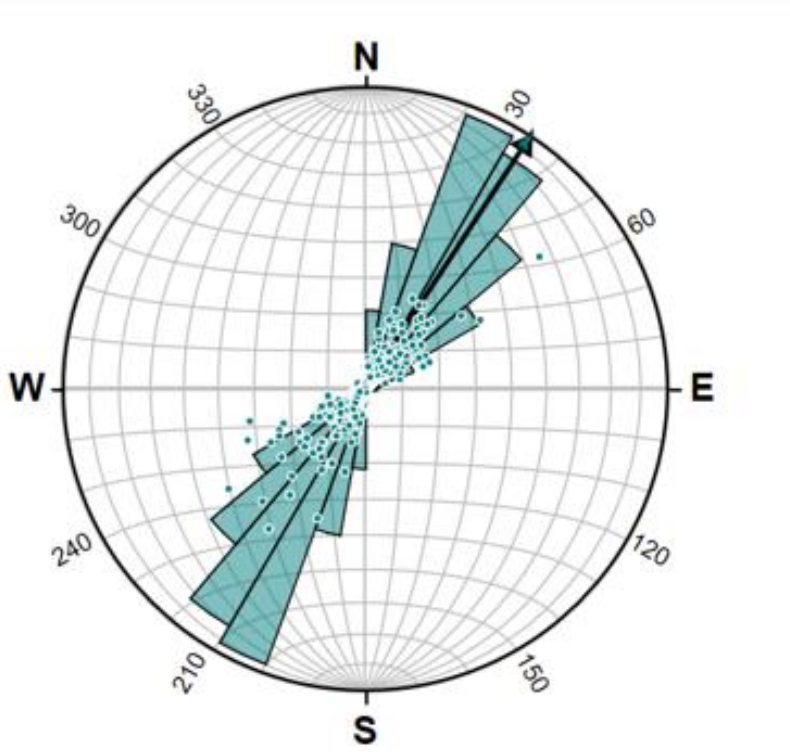

Fig. 4. The range of orientation of S_{Hmax} is N20E to N40E based on the rose diagram analysis (Allmendinger, 2020). DIFs in vertical wells are used to plot the rosea diagram and the mean of the azimuth of DIFs is N33E indicating the direction of S_{Hmax}.

KIRSCH SOLUTION BASED S_{HMAX} ANALYSIS

Tensile fractures form when tensile stress around the wellbore is greater than the tensile strength of the rock and when it is lower than the minimum tangential stress. Hubbert and Willis conclude a method where they use Kirsch solution and rock elasticity to find far field S_{Hmax} (1957). In a vertical well where one of the maximum horizontal stresses is less than vertical stress, the minimum value of tensile stress around the wellbore takes place at S_{Hmax} direction (Eq. 10). If wellbore pressure P_w accedes the minimum tangential stress, $\sigma_{\theta\theta}$, which is also equal to the rock's tensile strength $-T_o$, the tensile fracture will initiate (Eq. 12). During hydraulic fracturing, the fluid pressure P_b equals the minimum effective tangential stress plus the rock's tensile strength, a

tensile fracture(s) initiate (Eq. 13). The same is true while drilling with the "breakdown pressure" being the wellbore pressure during drilling (Jaeger et al 2007). In a geothermal reservoir, the temperature difference between cool drilling fluid and hot formation induces thermal stresses. Thermal stress adds to the stress around the wellbore and thus contributes to the induction of drilling-induced fractures. As a result, the thermal stress term is also added to the Kirsch solution in Eq. 13. The final equation in Eq. 14 is used to calculate the magnitude of S_{Hmax}.

$$-T_o = -S_{Hmax} + 3S_{hmin} - (P_w - P_o) \quad \text{Eq. 12}$$

$$P_b = -S_{Hmax} + 3S_{hmin} - P_o + T_o \quad \text{Eq. 13}$$

$$S_{Hmax} = 3S_{hmin} - P_w - P_o + T_o + \sigma^{\Delta T} \quad \text{Eq. 14}$$

FRACTURE MECHANICS BASED S_{HMAX} ANALYSIS

S_{Hmax} can be estimated from the stress intensity factor and Kirsch solution with the use of drilling-induced fractures (Eq. 15). This method was developed by Rummel (1987). Later the method was modified by Brudy and Zoback by adding the thermally induced stresses to the equation (1999). Eq. 15 uses type model I stress intensity factor (K_I) to compare with rock toughness (K_{IC}). K_I defines the state of stresses at the tip of a fracture and is a function of stress loading and geometry; K_I superposes various stresses loading on a fracture by summing various types of stress loading (Nygren and Ghassemi, 2005). For example, each stress loading K_I is defined in Eq. 17 to Eq. 21. By rearranging Eq. 15, Eq. 16 will be used to calculate S_{Hmax}. The sign convention is the same as used in the Kirsch solution above where positive is compression and negative is tension.

$$K\left(S_{Hmax}, S_{hmin}, P_w, P_{frac}, \sigma_{\theta\theta}\Delta T\right) = K(S_{Hmax}) + K(S_{hmin}) + K(P_w) + K\left(P_{frac}\right) + K(\sigma_{\theta\theta}\Delta T) + K_{IC} \quad \text{Eq. 15}$$

$$S_{Hmax} = \frac{[-S_{hmin}g(b)+p_w h_w(b)+ p_f h_f(b)+Dj(b)]\sqrt{R}-K_{IC}}{\sqrt{R}f(b)} \quad \text{Eq. 16}$$

$$K(S_{Hmax}) = S_{Hmax}\sqrt{R}f(b) = -2S_{Hmax}\sqrt{R}\left(b^2 - \frac{1}{\pi b^7}\right)^{\frac{1}{2}} \quad \text{Eq. 17}$$

$$K(S_{hmin}) = -S_{Hmin}\sqrt{R}g(b) = -S_{Hmin}\sqrt{R}\left[\sqrt{\pi b}\left(1 - \frac{2}{\pi}\text{asin}\left(\frac{1}{b}\right)\right)\right] + 2(b^2+1)\sqrt{\frac{b^2-1}{\pi b^7}} \quad \text{Eq. 18}$$

$$K(p_w) = \sqrt{R}p_w h_w(b) = \sqrt{R}p_w\left[1.3\frac{b-1}{1+\sqrt{b}} + 7.8\frac{sin\left(\frac{b-1}{2}\right)}{2\sqrt{b}-1.7}\right] \quad \text{Eq. 19}$$

$$K(p_{frac}) = \sqrt{R}p_f h_f(b) = \sqrt{R}p_f\left[\sqrt{\pi b}\left(1 - \frac{2}{\pi}\text{asin}\left(\frac{1}{b}\right)\right)\right] \quad \text{Eq. 20}$$

$$K(\sigma_{\theta\theta}{}^{\Delta T}) = \sqrt{R}Dj(b) = \sqrt{R}D\left(\frac{1}{2}+\frac{1}{2}I_o^{-1}\right)\sqrt{\pi b}\left(1 - \frac{2}{\pi}\text{asin}\left(\frac{1}{b}\right)\right) + (1 - I_o^{-1})\sqrt{\frac{b}{\pi}}\sqrt{b^2-1} -$$

$$I_o^{-1}\sqrt{\pi b}\ln(b) \quad \text{Eq. 21}$$

$$I_o^{-1} = \frac{1}{\pi}\text{asin}\left(\frac{\pi}{B}\right) - \frac{0.5772}{\pi^2+B^2} + \frac{1.9781B}{(\pi^2+B^2)^2} \quad \text{Eq. 22}$$

Eq. 17 and 18 are stress intensity functions for in-situ principal stresses and they consider the loads due to the far filed stresses S_{Hmax} and S_{hmin} on the wellbore by using Kirsch solutions. The b value is the dimensionless radius and is defined as the ratio of initial fracture length, a, over wellbore radius r. Eq. 19 is the stress intensity from well pressure (p_w), the wellbore pressure is the dynamic wellbore pressure and is calculated as (0.95×pump pressure + static wellbore pressure (P_{hydr}). This method of calculating dynamic wellbore pressure is based on Zoback et al. and is then used in Eq. 20 as (P_f)(1999). Fracture pressure can be replaced by static wellbore pressure and pore pressure (P_p). Static wellbore pressure is the hydrostatic mud pressure and is calculated from mud weight. Pore pressure is calculated from the hydrostatic gradient of 0.433 psi/ft. Eq. 21

is the thermally induced stress intensity factor. In this term, D is thermal stress, and its equation is $D = {\sigma_{\theta\theta}}^{\Delta T} = \frac{\alpha_T * E * \Delta T}{1-v}$. α_T is the linear expansion coefficient. E is Young's modulus, ΔT is the temperature differences between disturbed and undisturbed. v is Poisson's ratio. In Eq. 22, $B\ is \ln\left(1.26094\frac{KT_c}{r^2}\right)$, in which *K* is thermal diffusivity, T_c is cooling time, and r is the wellbore radius.

Lastly suing Eq. 16, S_{Hmax} is plotted verses dimensionless radius b. The minimum point on the plot indicates that there will be no fracture extension below the value of minimum S_{Hmax}. For the values greater than the minimum S_{Hmax}, the initial fracture length a can be extended (Brudy and Zoback, 1999). Thus, the minimum S_{Hmax} represents the minimum in-situ stress to initiate a fracture. Then the lower bound of S_{Hmax} can be found by searching for the minimum value of the stress curve. For example, in Fig. 5, the black dots at the lowest point on the curve is the lower bound of S_{Hmax} value.

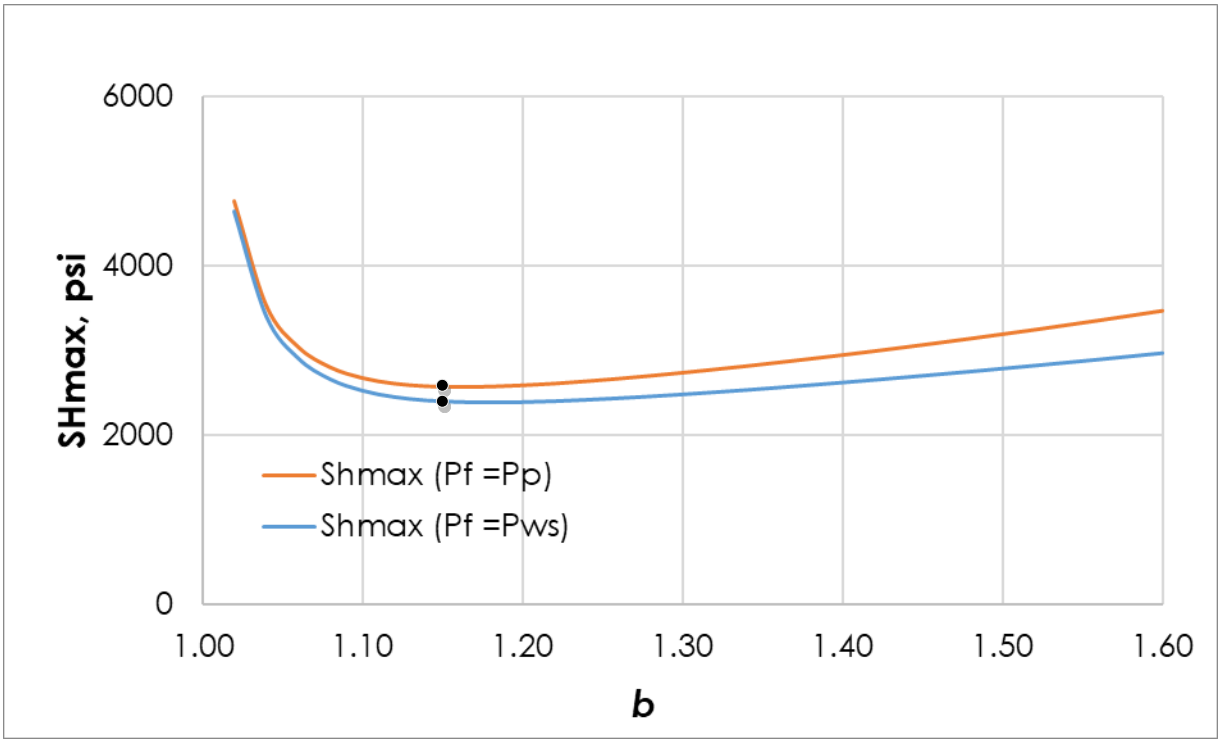

Fig. 5. The plot of maximum horizontal stresses versus dimensionless wellbore radius. The orange line is the S_{Hmax} calculated when the pressure in DIF equals the pore fluid pressure. The blue line is the S_{Hmax} calculated when the pressure in DIF equals the static wellbore pressure. The lowest point on the curve is the lower bound of S_{Hmax} value for each case.

CONSTRAINING S_{Hmax} USING BREAKOUTS

In a vertical well, S_{Hmax} can be estimated using breakout geometry and Kirsch solution (Bell and Gough, 1983; Barton et. al., 1988; Brudy and Zoback, 1998; Zoback et al, 2003). Breakout forms when the tangential stress on a wellbore is at the maximum and stress exceeds the rock's compressive strength: C_o. The maximum tangential stress occurs at about 90 degrees from S_{Hmax} and this relationship can be seen in Fig.3 and is described in Eq. 11. Then equating compressive strength C_o to maximum tangential stress in Eq. 9. A relationship between S_{Hmax}, S_{hmin}, C_o, and

angle θ_b is shown in Eq. 23. In Eq. 23, θ_b is breakout angle with respect to S_{Hmax} and it is half of the breakout angle: φ_b. φ_b is the half angle measured (from S_{hmin}) on breakout observed from image logs such as FMI and UBI logs. For example, in Fig. 7, $2\varphi_b$ is about 60 degrees, so φ_b is 30 degrees and $\theta_b$would be 60 degrees. Eq. 23 also integrates thermal stress contribution to the tangential stress. In Utah FORGE, thermal induced stress is also important to consider because of temperature differences between the drilling mud and the rock.

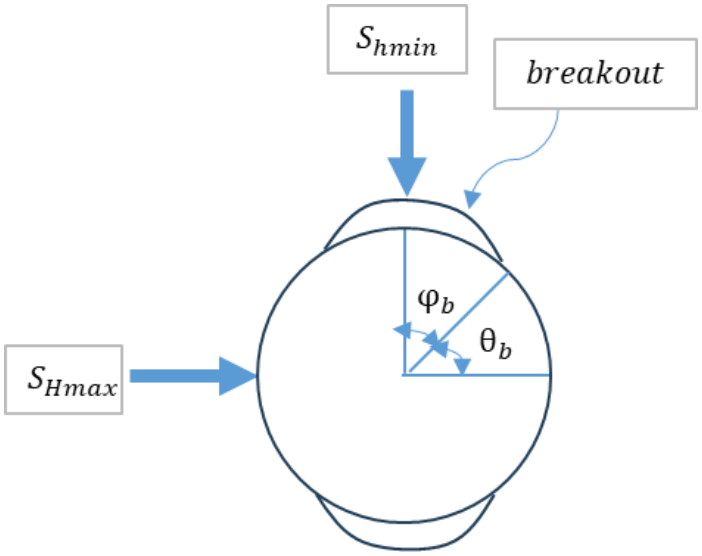

Fig. 6 The cartoon shows the measurement of half angle: φ_b. It can be found by measuring the width of the breakout from the FMI log. Then θ_b is found from φ_b.

With the known measurement of breakout half angle and compressive strength of the rock and minimum horizontal stress, S_{Hmax} can be calculated. The rock strength C_o is usually measured from the lab using an intact rock sample taken from the reservoir. However, a study done by Ye et al. shows that S_{Hmax} solution based on the breakout is heavily dependent on rock strength C_o, and a more representative rock strength should be constrained using an existing S_{Hmax} result based on DIF (2022).

$$S_{Hmax} = \frac{(C_o + 2P_P + \Delta P + \sigma^{\Delta T}) - S_{hmin}(1 + 2cos2\theta_b)}{1 - 2cos2\theta_b}$$ Eq. 23

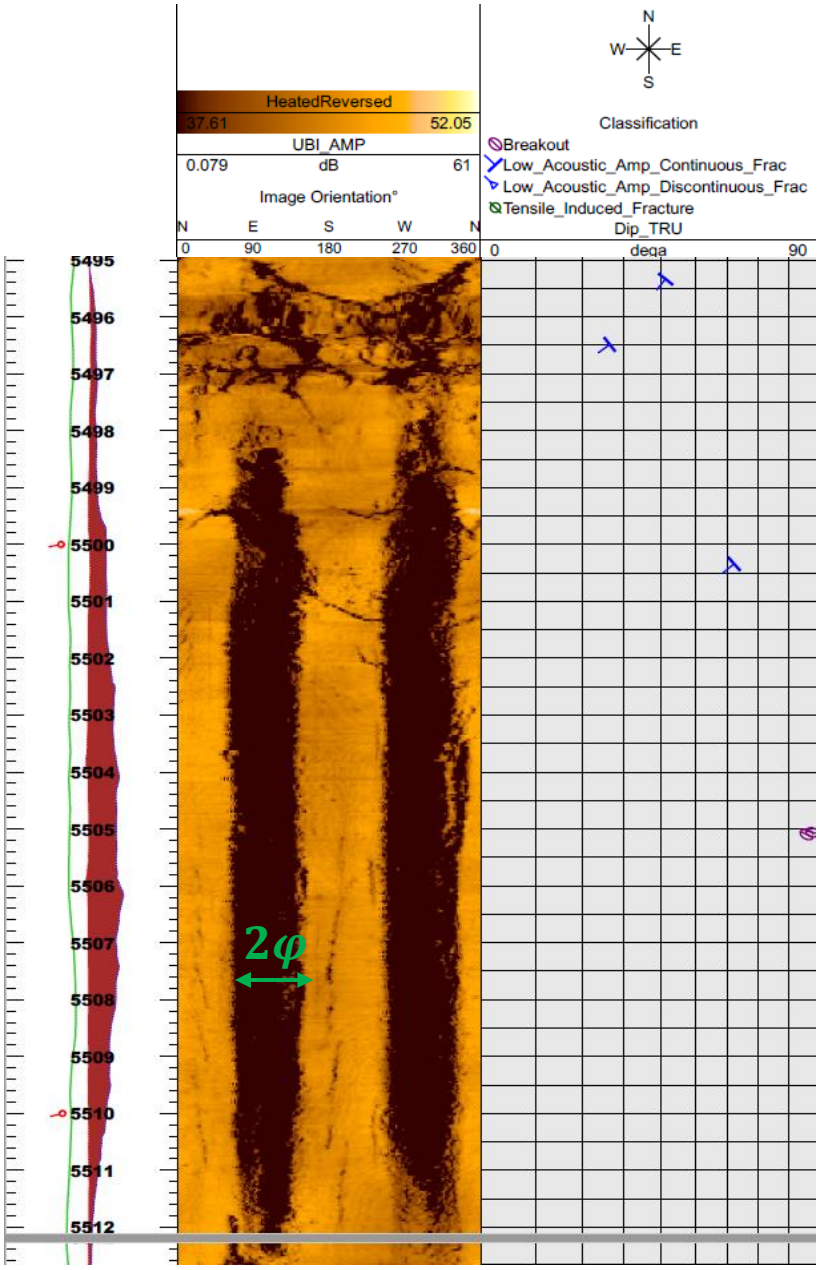

Fig. 7. The FMI log shows the observed breakout in well 78B-32. The green arrow indicates the 2 times half angle. Since half angle is measured from the failure initiation point of the breakout to the axis of the breakout, the double of the half angle is the width of the breakout (U.S. Department of Energy the GDR Geothermal Data Repository).

In Utah FORGE, the lab test result from intact rock taken from well 58-32 gives a compressive strength in the range of 13200 psi to 18300 psi (Ye et al., 2022 and McLennan, 2018). When using this range of compressive strength, the result of S_{Hmax} gradient is significantly greater than the S_{Hmax} gradients from DIF based Kirsch and fracture mechanics based S_{Hmax} analysis. For example, the S_{Hmax} ranges from 0.83 - 0.98 psi/ft from the methods of using DIFs in well 78B-32 a depth of around 8336 ft, but when using breakouts with these compressive strength values, the S_{Hmax} can range from 1.2 – 1.47 psi/ft. This range of S_{Hmax} lead to a strike slip fault regime. However, based on previous studies and multiple datasets, Utah FORGE is a normal fault dominated reservoir (Ye et al, 2022).

If the fault regime is restricted in the normal regime, then there are two possible reasons for such large S_{Hmax} ; one is a very large S_{Hmax} stress and another one is that the breakout occurs in a weak formation zone. From the FMI log, if the S_{Hmax} is large there would be multiple breakouts in the well however, there are only 3 observed breakouts in well 78B-32 and it can be concluded that the strong S_{Hmax} is not likely the cause. On the other hand, there are 2900 observed naturally occurring continuous and non-continuous fractures in 78B-32. Continuous fractures form naturally and non-continuous fractures can form due to thermal stresses. Natural fractures indicate the formation is weak and it can initiate breakout easily. Another indicator of weak formation is the irregular shape of the breakout in well 78B-32 as can be seen in Fig. 8. The breakout is asymmetric and irregular suggesting that the breakout occurs in a weak zone of the formation due to naturally occurring fractures or inclusions and thus the rock strength resulting from an intact rock sample is not realistic to represent the true compressive strength in the formation (Ye et al, 2022).

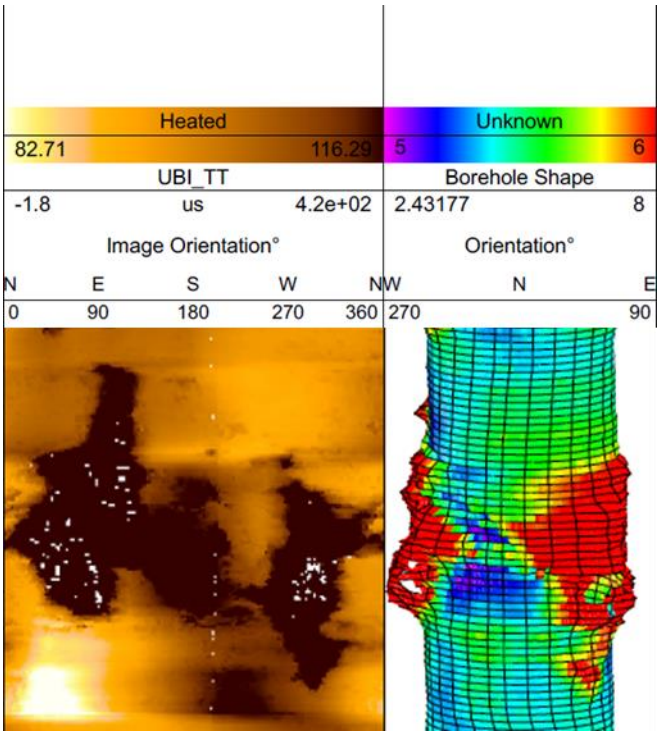

Fig. 8. The asymmetric breakout shown on the FMI log and its 3D model. The left and right pair of breakouts are irregular and asymmetric with each other (U.S. Department of Energy the GDR Geothermal Data Repository).

A more realistic compressive strength value can be obtained by estimating the compressive strength with an existing S_{Hmax} result based on DIF that is observed at the same depth as the breakout at the same depth. In Utah FORGE, for example in well 78B-32, there are occurrences of both breakout and DIFs at the same depth interval at 8336 ft. The S_{Hmax} based on DIFs is then used to calculate the new compressive strength using the breakout based equation in Eq. 23. Then the new compressive strength is a more realistic compressive strength that represents effective compressive strength in Utah FORGE. This effective compressive strength is then used to calculate S_{Hmax} based on breakout observation from other wells. The new result of breakout based S_{Hmax} calculation is then plotted in the result section. For example, in Fig. 10 the breakout values

in well 78B-32 are very close to the S_{Hmax} values estimated based on fracture mechanics and fracturing based Kirsch solution. The result indicates a normal stress fault regime and this confirms with the corresponding stress regime in Utah FORGE.

Finally, a new range of effective compressive strength in Utah FORGE is constrained and ranges from 5300- 8000 psi. It is constrained using upper and lower bounds of S_{Hmax} based on DIFs that are observed at the same depth of breakout in 8336 ft. (Fang et al., 2022; Ye et al., 2022). The upper and lower bounds of S_{Hmax} are 0.83 to 0.98 psi/ft and they are calculated based on the range of 0.71 to 0.75 psi/ft of S_{hmin}. The effective compressive rock strength is usually 1/3 of the lab measured compressive strength according to Brady and Brown (2006). Based on our calculation, the effective compressive rock strength in Utah FORGE is ½ of the intact rock compressive strength (Ye et al., 2022).

INPUTS AND DATA FOR VERTICAL WELLS

The input data of Utah FORGE wells are mainly collected from literature and experimental lab tests. Some parameters are calculated based on assumptions that are used by other researchers. For the method using fracture mechanics the input parameters are: $S_{hmin}, P_{pore}, P_{stc}, P_{dyn}, R, E, v, K_{IC}, k, \alpha_T, \Delta T, T_c$. The parameters used for hydraulic fracturing based Kirsch solution are: $S_{hmin}, P_{pore}, P_{dyn}, E, v, k, \alpha_T, \Delta T \; and \; \tau$. The parameters used for the breakout based Kirsch solution are: $S_{hmin}, P_{pore}, P_{dyn}, E, v, k, \alpha_T, \Delta T, \varphi_b, \theta_b, C_o$. These parameters used and their sources are listed in Table.1. In Table.1, S_{hmin} gradient in Utah FORGE is 0.73 psi/ft. This result is from the DFIT test and is conducted by Xing et al (2020). Pore pressure is calculated by using hydrostatic pressure and is 0.433 psi/ft. static wellbore pressure is calculated using 0.052 × mud weight multiplied by TVD. Maximum well pressure is calculated by using

0.95*pump pressure + static wellbore pressure (P_{stc}). This assumption was used by Brudy and Zoback (1999). The wellbore radius is found from the drilling activities log as bit size.

Young's modulus, poison's ratio, tensile strength and thermal diffusivity, and Model 1 fracture toughness are lab tested results from well 58-32(McLennan, 2018). The final parameter to use is the average lab tested results from variable samples.

For the temperature differences of the reservoir, we assumed that the temperature difference is the wellbore fluid temperature differences before and after the well is drilled. When the well is in the process of drilling or soon after drilling, the wellbore fluid temperature can represent the temperature of the disturbed reservoir because the heat from the reservoir is brought away by the constant fluid circulating during drilling activities. When a well is shut in for a long time, the temperature of the well fluid can represent the formation temperature when it is undisturbed since the well temperature reaches equilibrium with the wellbore fluid. For instance, in well 16(A)78-32, the disturbed formation temperature is the well fluid temperature on 12/26/2020 which is logged immediately after the previous drilling activities; the previous drilling activity stopped on 12/26/2020. Since we were only interested in the vertical section of the well in 16(A)78-32, the depth of this temperature log ran up to the depth of 7000 ft. The temperature measured during this time can effectively represent the disturbed formation temperature since the logging date is immediately run after drilling and circulating activities and during drilling, the well is cooled by circulating mud constantly. The undisturbed formation temperature is set as the well temperature on 8/16/2021 which is about 216 days after the rig release date which is on 1/12/21. This amount of time allows the formation temperature to reach equilibrium with the surrounding formation.

Lastly, the cooling time is calculated by using the differences between drilling time and FMI logging time (Brody, M., and Kjorholt, 1999). The cooling time is assumed to be the time the formation uses to reach temperature equilibrium after a disturbance of the formation temperature. The last circulation is conducted when the well was drilled and the heat was circulated out of the formation form wellbore. Since the measurement of DIFs are taken at well logging time, the time it is used to reach equilibrium is between the last circulation and the well logging time.

Table.1. Parameters used for all methods for stress analysis in vertical wells. They are collected from lab testing, well tests, and literature.

Parameter	Value	Description	Source
$S_v, psi/ft$	1.13	Vertical stress	(Moore et al., 2020)
$S_{hmin}, psi/ft$	0.71-0.75	Minimum horizontal stress	(Xing et al, 2020)
$P_{pore},\ psi/ft$	0.433	formation/pore pressure	(McLennan, 2018b)
P_{stc}, psi	$MW \times TVD$	static wellbore pressure	Drilling reports
P_{dyn}, psi	$0.95 \times\ P_{surf} + P_{stc}$	maximum wellbore pressure	Brudy & Zoback, 1999
R, in	4.38	wellbore radius	Bit size
E, psi	7970000	Young's modulus	Average values from the laboratory core tests (McLennan, 2018)
v	0.26	Poisson ratio	
T, psi	1295	Tensile strength	
K_{IC}, $psi - in^{0.5}$	2257	mode-1 fracture toughness	FORGE Website (https://utahforge.com/data/)
$k, in^2/s$	0.00218	Thermal diffusivity	58-32 core test (Gwynn et al., 2019
$\alpha_T, 1/K^{\circ}$	0.000002	Thermal expansion coefficient	FORGE Website (https://utahforge.com/data/)
$\Delta T, K$	The temperature difference between the disturbed and undisturbed formation	Wellbore temperature	Temperature logs
T_c, hr	The difference between drilling and logging time	Cooling time	(Brudy and Kjorholt, 1999)
C_o, psi	13200 - 18300	Uniaxial compressive strength	Laboratory core tests (McLennan, 2018)
φ_b, degree	Half of the breakout width	Half of the breakout width	UBI logs
θ_b, degree	$\theta_b = 90 - \varphi_b$	Angle between $S_{Hmax}$and the edge of the breakout	

RESULTS

The figures below display the stress profiles of the four wells: 16(A)78-32, 78B-32, 58-32, and 56-32. The plot shows S_v, S_{hmin}, P_p and calculated S_{Hmax} based on all methods discussed above. The profile also shows S_{hmin} from different DFITs to show the reliability of S_{Hmax} profile. For instance, all wells have a S_{Hmax} profile that is greater than most of the S_{hmin} value and lower than S_v value. This complies with the stress regime of a normal fault regime in the Utah FORGE.

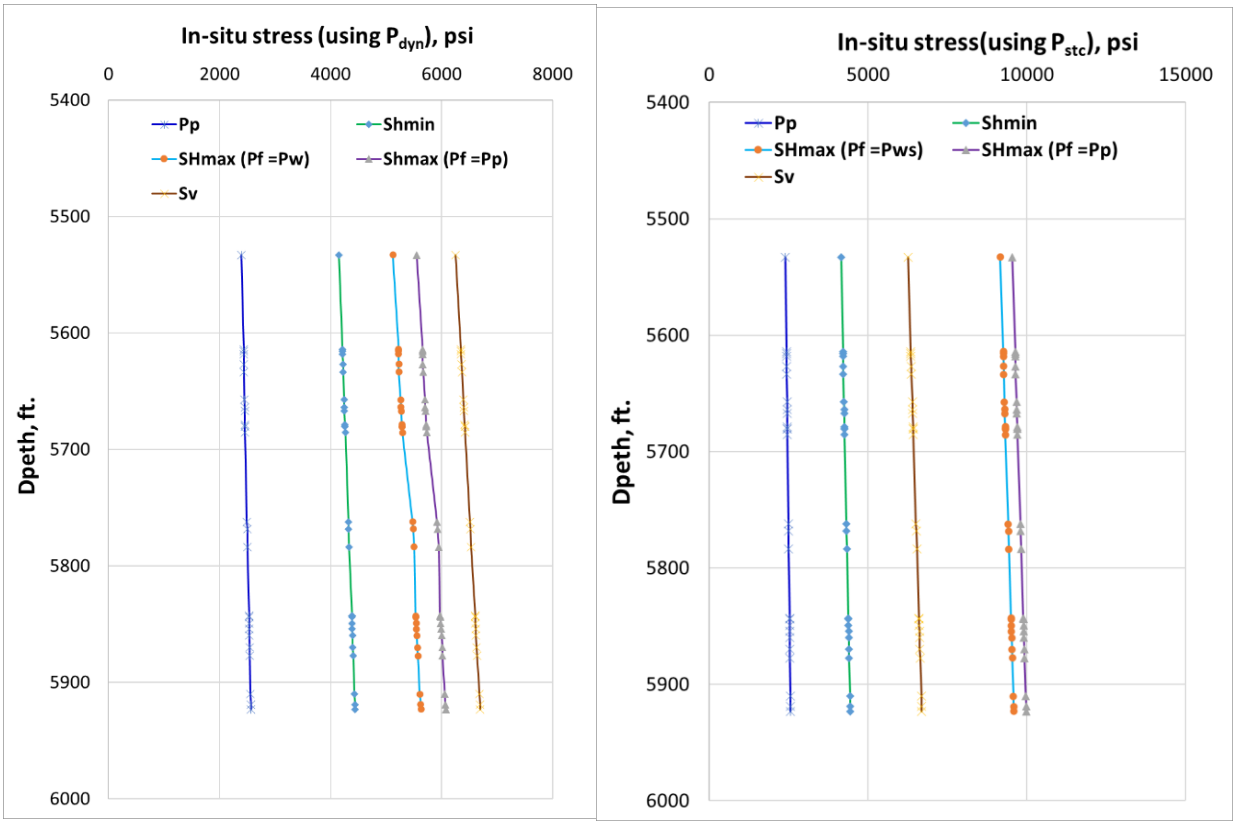

Fig. 9. The in-Situ Stress Profile of Well 16(A)78-32. The green line is the S_{Hmax} using the method of fracture mechanics and the red line is S_{Hmax} using Kirsch solution based on hydraulic fracturing mechanism. The gradients of S_v and P_p are 1.13 psi/ft and 0.433 psi/ft. The S_{hmin} gradient is the average of DFIT from the injection zone in well 16(A)78-32 which is 0.73 psi/ft.

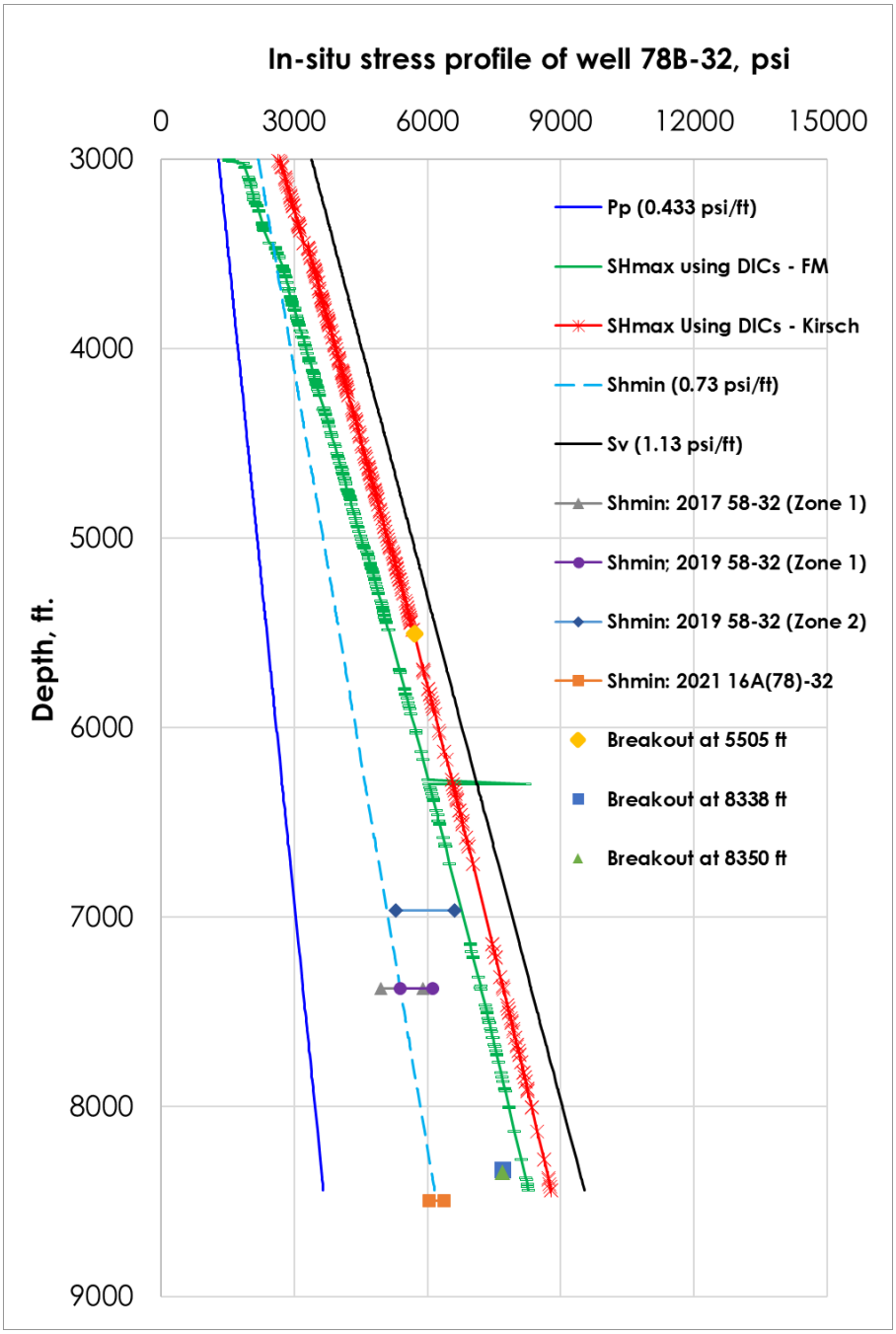

Fig. 10. In situ stress profile of well 78B-32. The green line is the S_{Hmax} using the method of fracture mechanics and the red line is S_{Hmax} using Kirsch solution based on hydraulic fracturing mechanism. The dots are the S_{Hmax} result using the breakout based Kirsch solution. The gradient of S_v and P_p are 1.13psi/ft and 0.433psi/ft. The S_{hmin} gradient is the average of DFIT from the injection zone in well 16(A)78-32 which is 0.73 psi/ft.

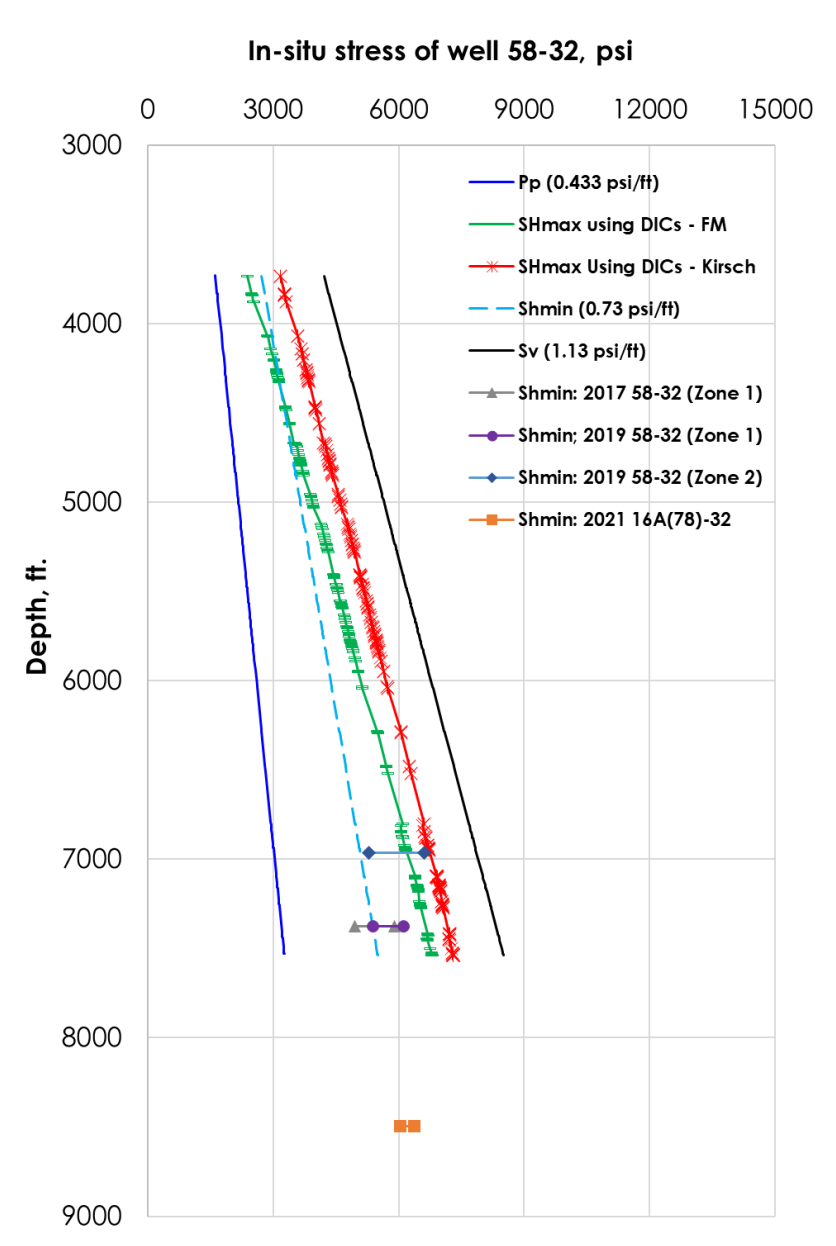

Fig. 11. In situ stress profile in well 58-32. The green line is the S_{Hmax} using the method of fracture mechanics and the red line is S_{Hmax} using Kirsch solution based on hydraulic fracturing mechanism. The gradient of S_v and P_p are 1.13psi/ft and 0.433psi/ft. The S_{hmin} gradient is the average of DFIT from the injection zone in well 16(A)78-32 which is 0.73 psi/ft.

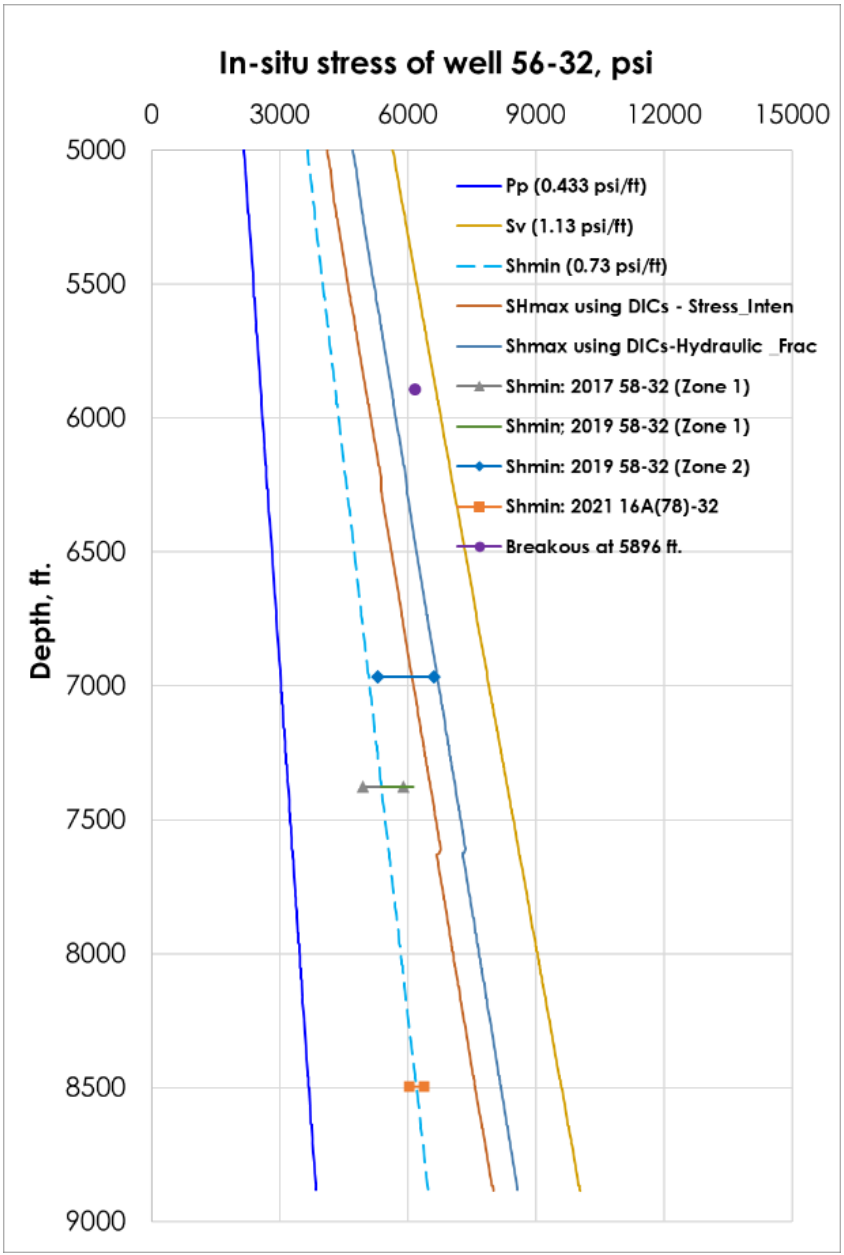

Fig. 12. In situ stress profile in well 56-32. The brown the S_{Hmax} using the method of fracture mechanics and the blue line is S_{Hmax} using Kirsch solution based on hydraulic fracturing mechanism. The dots are the S_{Hmax} result using breakout based Kirsch solution. The gradient of S_v and P_p are 1.13psi/ft and 0.433psi/ft. The S_{hmin} gradient is the average of DFIT from the injection zone in well 16(A)78-32 which is 0.73 psi/ft.

INCLINED WELLS

In an inclined wellbore, the Kirsch solution is not applicable if none of the principal stress is aligned with the wellbore direction. Kirsch's solution describes the wellbore stresses in relationship to far field principal stress based on a circular vacancy in a homogenous and elastic plane. In a vertical wellbore, the maximum and minimum tangential stresses are only functions of horizontal principal stresses. And the value of S_{Hmax} can be easily found based on tangential stress equations with the use of drilling induced fractures. In an inclined wellbore, however, the tangential wellbore stresses are not only the functions of horizontal stresses but a function of vertical principal stress, so the direct use of the Kirsch solution is not applicable. Therefore, a new method to calculate S_{Hmax} requires principal stress rotations, maximum tangential stress equation on the wellbore, and the observation of drilling induced fractures to solve the problems in inclined wellbore.

This method is developed and confirmed by Hiramatsu and Oka (1962), Hayes (1965), and Fairhurst (1967). They rotate far field principal stress to the wellbore coordinate using stress rotation tensors. Then based on the Kirsch solution they found the maximum and minimum tangential principal stress on the wellbore wall with respect to in far field principal stresses. Max and min tangential equation then describes the stress on the wellbore that causes the formation of drilling induced fractures, and then using the drilling induced fractures data, in situ stress such as S_{Hmax} can be found. Kirsch equations are listed from Eq. 1 to Eq. 6 and the max and min tangential stresses on an inclined wellbore are in Eq. 24 to Eq. 25. These relationships can be used for both point failure and plane failure methods which will be discussed further.

S_{Hmax} ANALYSIS BASED ON POINT FAILURE

In this method, fractures are viewed as points on the wellbore, and their occurring locations θ is used as the input parameter to estimate in situ principal stress such as S_{Hmax}. After the principal

stress tensor rotation from principal stress to wellbore coordinate, the Kirsch solution can be modified to find the maximum and minimum effective principal stress on a tangential plan on the wall (Eqs 24 to 25). By following the convention that compression is positive and tensile is negative, fractures form when tangential stress is the minimum. Thus, the maximum tensile stress can be found by taking the derivative of minimum effective principal tangential stress with respect to θ. When fracture forming location θ is known as the input, the minimum tangential stress equation can help calculate the unknown principal stress S_{Hmax}. This relationship is described in Eq. 26 (a).

Maximum and Minimum Tangential Stress on an Inclined Wellbore.

In a vertical wellbore, Kirsch solutions can be used to calculate maximum and minimum tangential wellbore stresses equations by using only two principal stresses: S_{hmin} and S_{Hmax} directly (Blanksma et al.). However, in an inclined wellbore all three principal stresses act on the circumference of the wellbore; meaning the maximum and minimum tangential stresses on the wellbore are contributed by all three fat field principal stresses. This invalidates the direct use of Kirsch's solution discussed in the earlier chapter.

Fortunately, Hiramatsu and Oka (1962), Hayes (1965), and Fairhurst (1967) calculate tangential stress on an inclined wellbore by calculating the plane of maximum and minimum stress on the wellbore with the incorporation of σ_{zz} (Eq. 24 and Eq. 25)

$$\sigma_{maxD} = \frac{1}{2}\left[\sigma_{zz} + \sigma_{\theta\theta} + \sqrt{(\sigma_{zz} - \sigma_{\theta\theta})^2 + 4{\tau_{\theta z}}^2}\right] \quad \text{Eq. 24}$$

$$\sigma_{minD} = \frac{1}{2}\left[\sigma_{zz} + \sigma_{\theta\theta} - \sqrt{(\sigma_{zz} - \sigma_{\theta\theta})^2 + 4{\tau_{\theta z}}^2}\right] \quad \text{Eq. 25}$$

In Eq. 24 and 25, θ is the wellbore central angle and it is measured from fractures counterclockwise. The angle θ is shown in the wellbore geometry in Fig. 14. On the wellbore at the location where the magnitude of σ_{maxD} is maximum, the breakout can form when the rock compression strength is exceeded. However, if compression is negative and tension is positive, σ_{maxD} can also be seen as maximum tensile stress and drilling induced fracture forms when σ_{maxD} reaches this maximum. This is how Okabe, T., et al, used σ_{maxD} in their study to calculate in situ stress using drilling induced fractures (1998). In this work, compression is assumed positive and tension is negative. Eq. 26 is used to calculate the locations where drilling induced tensile fractures occur. When σ_{minD} is the minimum tangential stress on the wellbore, and compression is positive, tensile stress is then the most, and drilling induced fracture could form when tensile strength is exceeded. This allows Eq. 25 to be used as the least tensile stress and can indicate the occurrence of drilling induced fractures.

σ_{maxD} and σ_{minD} are periodic functions with a period of 180 degrees. By using their sinusoidal properties, the maximum and minimum points of the function can represent borehole failure stress by taking the derivative with respect to θ (Eq. 26 a). However, σ_{maxD} and σ_{minD} do not always have one extreme value in the degree between 0 and π and it is impossible to find the maximum compression or minimum tensile stress by finding the extreme points from the equations (Zoback and Peska et al, 1995. Blanksma, et al, 2018, and Mastin, L,1988). According to Mastin, L., even though σ_{maxD} is sinusoidal functions, it deviates away from sinusoidal behavior as wellbore inclination changes. There are multiple extreme values on the maximum stress equation such as when the inclination is at 35 degrees in Fig. 13. Drilling induced fractures can occur at any location where the extreme value lies. Due to this reason, the maximum or minimum tensile stress cannot be found directly using Eq. 26 a) (1988).

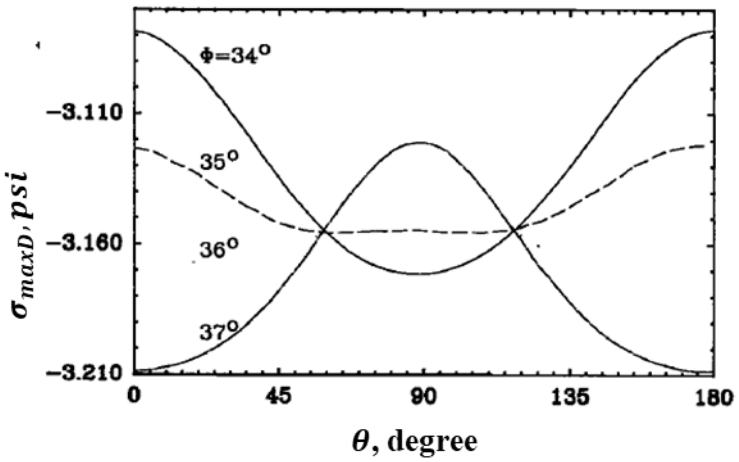

Fig. 13. σ_{maxD} magnitude becomes a non-sinusoidal function as the inclination of the wellbore changes. For instance, when phi is at 90 degrees, there is more than one extreme value even though it has a period of 180 degrees. In the case of point failure where only one drilling induced fracture forms, its location can be at either extreme value (Mastin, L,1988).

However, in our problem, the values of the θ_m , which is the direct measurement of the DIF location, is observed from FMI logs directly. Knowing that θ_m satisfies Eq. 25 such that θ_m is the location on the wellbore where one of the extreme values occurs, the equation of derivatives of σ_{maxD} or σ_{minD} can be used to describe the relationship between drilling induced fractures and far field principal stresses S_{Hmax}. They can be used in combination with other parameters or equations to calculate S_{Hmax} and this will be addressed in later sections.

On a wellbore, θ_m is the angle measured from x_b counterclockwise toward fracture, but this cannot be read directly from the FMI log. θ_{mD} is the central angle measured from the north clockwise to the location where DIFs occur and it can be read from the FMI log. Then Eq. 26 (b)

is used to convert θ_{mD} to θ_m. In Eq. 26 (b), δ and φ are wellbore azimuth and wellbore inclination separately and they are represented in the Fig. 14 below.

$$\begin{cases} \frac{d\sigma_{maxD}}{d\theta} = 0 \\ \theta_{mD} = tan^{-1}(cos\delta \times tan\varphi) + \frac{\pi}{2} - \theta_m \end{cases}$$ Eq. 26 (a), (b)

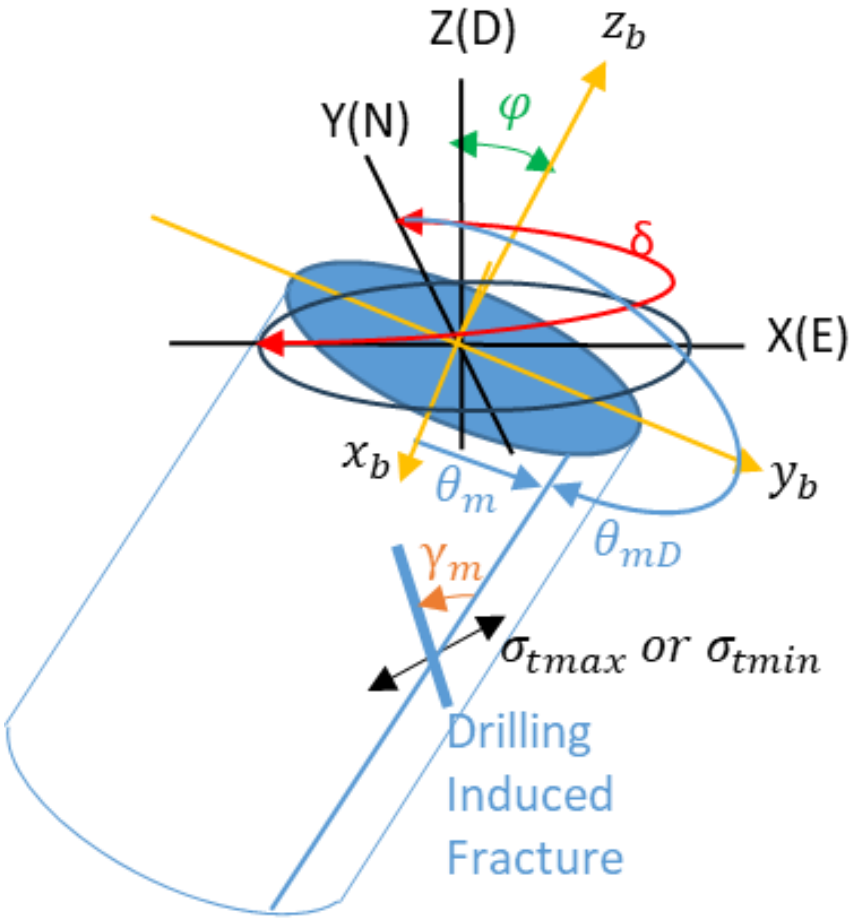

Fig. 14. Notations used for Eq. 24 to 28. θ_{mD} is the fracture azimuth measured clockwise from the north. θ_m is the central angle of the wellbore measured from maximum tensile stress σ_{mD}, where the drilling induced fracture occurs. In the picture, x_b, y_b, and $z_b$are wellbore coordinates. x_b points to the downside of the wellbore. X, Y, and Z are geographic coordinates, and they correspond to east, north, and down.

Incorporating Tensile Strength to Tangential Wellbore Stress

According to Okabe et al in a system where compression is positive, tensile failure tends to occur when the tangential stress is the minimum, which is also the maximum tensile stress. Fractures form when tensile stress accesses the tensile strength of the rock material. From this relationship, the least tangential stress equation in Eq. 25 can be equipped to the minus of the tensile strength (T) of the rock material. The new equation in Eq. 27 can be used to describe the relationship between fractures and tensile strength and far field principal stresses.

$$-T = \sigma_{minD} = \frac{1}{2}\left[\sigma_{zz} + \sigma_{\theta\theta} - \sqrt{(\sigma_{zz} - \sigma_{\theta\theta})^2 + 4{\tau_{\theta z}}^2}\right] \quad \text{Eq. 27}$$

S_{Hmax} Analysis based on Plane failure.

In the previous section, the stress inversion method is based on point failure, where the fracture is considered a point and its location on the wellbore is used as input data to calculate in suit stresses. There is another method that treats a fracture as a plane, and its inclination from the borehole axis is used to establish a relationship between in situ stresses and drilling induced fracture. This angel is called trace angel. In Eq. 28, the angle Υ_m is the trace angle of the drilling induced fracture plane and is measured from the wellbore axis towards the fracture plane counterclockwise. During the calculation, however, the value of $2\Upsilon_m$ has to be between -90 to 90 degrees as the inverse of tangent has its limits of -90 to 90 degrees. To avoid tangent limits, one reduces a 180 degree to an angle that is greater than 90 degrees.

For en echelon fractures, however, the sign of gamma at two locations of θ_m will be opposite to each other and can be determined from the FMI log. For example, in Fig. 15, the failure trace angles α (Υ_m) on the left side of the log are positive and the failure trace angle on the right side are all negative. Υ_m can then be used as an input parameter to help calculate stresses such as S_{Hmax}.

$$\Upsilon_m = \frac{1}{2} tan^{-1}\left(\frac{2\tau_{\theta z}}{\sigma_{\theta\theta} - \sigma_{zz}}\right)$$ Eq. 28

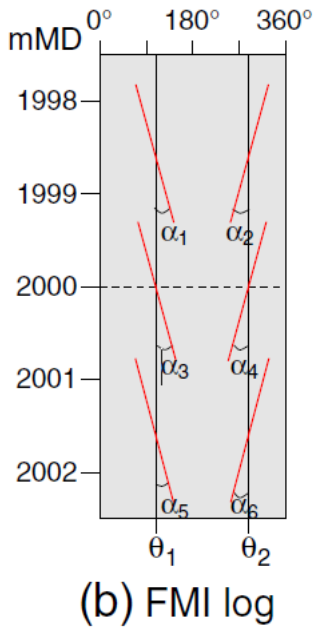

Fig. 15. Failure trace angles α on an en echelon fracture. Here α is the Υ_m in this paper (Thorsen, 2011).

S_{Hmax} IN VERTICAL WELLBORES

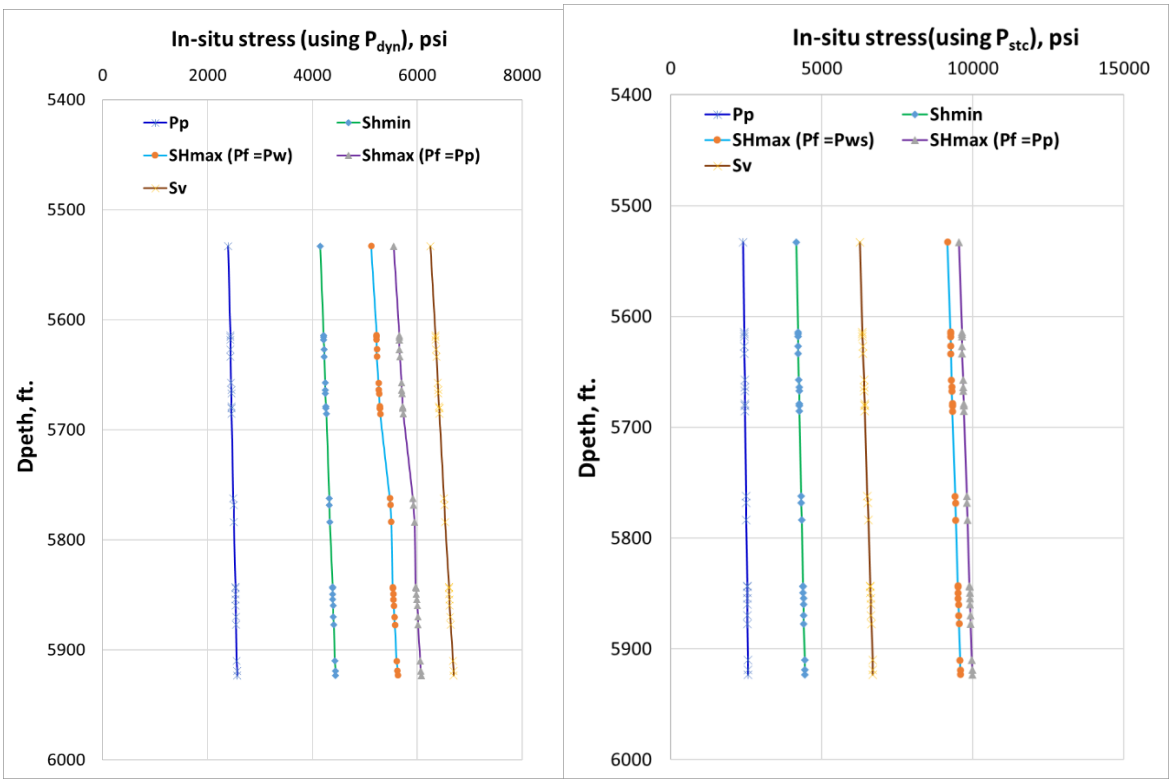

Fig. 20. In situ principal stresses in the vertical section of well 16(A)78-32. The blue and purple line shows S_{Hmax} results using fracture mechanics and blue line using wellbore static pressure being as fracture pressure. The purple line is the S_{Hmax} results using pore pressure as fracture pressure. A) shows the stress profile of S_{Hmax} when using P_{dyn} as wellbore pressure. B) shows the stress profile of S_{Hmax} when using static wellbore pressure as wellbore pressure. The gradient of S_v and P_p are 1.13 psi/ft and 0.433 psi/ft. The S_{hmin} gradient is the average of DFIT from the injection zone in well 16(A)78-32.

Table. 2 S_{Hmax} gradients in the vertical section of well 16(A)78-32. The average stresses gradient when using P_{stc} are greater than the S_{Hmax} gradient using P_{dyn}.

well name	Well Pressure Types	S_{Hmax} gradient (Fracture mechanics based; P_f=P_p), psi/ft	S_{Hmax} gradient (Fracture mechanics based; P_f=P_{stc}), psi/ft
16(A)78-32 Depth: 5500-5900 ft	Using P_{dyn}	1.00-1.03 Avg: 1.02	0.93-0.95 Avg: 0.94
	Using P_{stc}	Avg: 1.70	Avg: 1.64

For well 16(A)78-32, S_{Hmax} is estimated using fracture mechanics with the incorporation of thermal stress. There are two possible solutions of S_{Hmax} depending on the preferable well pressure. In the Fig. 31 A), the S_{Hmax} is calculated when well pressure is dynamic well pressure, meaning the pressure is the sum of static drilling fluid pressure and surface pump pressure. Its S_{Hmax} profiles are in between S_{hmin} and S_v, indicating a normal fault regime. This result is reasonable because in Utah FORGE the normal stress regime is the most common. In Fig. 20 B), the well pressure used is static well pressure, meaning the fluid in the well is calculated by the mud weight when not being circulated. However, the S_{Hmax} results are greater than S_v, which indicates a strike slip fault regime. This result is possible but not preferable because when drilling induced fracture forms, the well pressure is likely to be dynamic pressure rather than static pressure. The strike slip fault mechanism is possible in Utah FORGE but not common. Due to these reasons, the solution using static wellbore pressure is disregarded for further study. The final range of average S_{Hmax} gradient is 0.94 psi/ft to 1.02 psi/ft for the well 16(A)78-32.

It is also observed that the gradients of S_{Hmax} increases as the true vertical depth increases. This is because S_{Hmax} is a function of S_v and it increases as S_v increases (Sone and Zoback, 2014). This relationship can be explained in Eq. 32 in which S_{Hmax} is a function of Poisson's ratio and S_v.

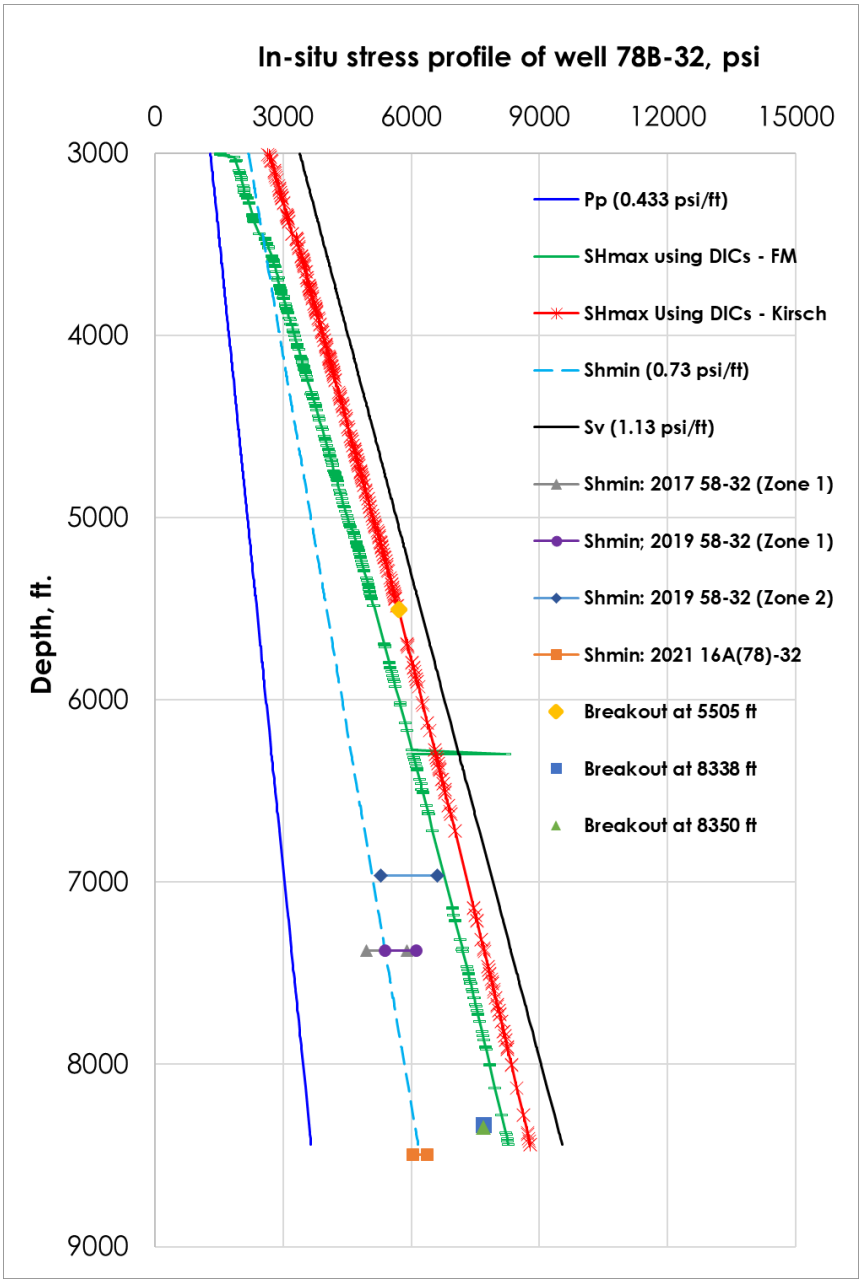

Fig. 21. In situ stress profile in well 78B-32. The green line is the S_{Hmax} using the method of fracture mechanics and the red line is S_{Hmax} using Kirsch solution based on hydraulic fracturing mechanism. The dots are the S_{Hmax} result using breakout based Kirsch solution. The gradient of S_v and Pp are 1.13psi/ft and 0.433psi/ft. The S_{hmin} gradient is the average of DFIT from the injection zone in well 16(A)78-32.

Table. 3 The range of gradient of S_{Hmax} in well 78B-32 based on all methods.

Well Name	Well pressure type	S_{Hmax} gradient (P_f=P_p), psi/ft	S_{Hmax} gradient (P_f=P_{stc}), psi/ft	S_{Hmax} gradient (Kirsch Solution Based on Hydraulic Fracturing Mechanism), psi/ft	S_{Hmax}Gradeint (Kirsch Solution Based on Breakout), psi/ft
78B-32 Depth: 3000-8440 ft	Using P_{dyn}	0.51-0.98 Avg: 0.86	0.45-0.98 Avg: 0.86	0.88-1.04 Avg: 1.00	0.92 and 1.04

In Fig. 21. the model of S_{Hmax} in well 78B-32 is presented. For this vertical well, two methods were used. One is fracture mechanics and the other uses Kirsch solution. Both stress profiles of S_{Hmax} shows a normal fault regime which is expected since Utah FORGE is most common in having normal faults. S_{Hmax} using the Kirsch method is larger than it is using the fracture mechanics method and this is reasonable considering the differences among different mechanisms. It is easier to propagate a fracture when using the fracture mechanics approach than initiate a new fracture when using the Kirsch solution. Well 78B-32 has an average S_{Hmax} gradient of 0.86 psi/ft -1.04 psi/ft based on all methods. This range is consistent with the gradient from other vertical wellbores.

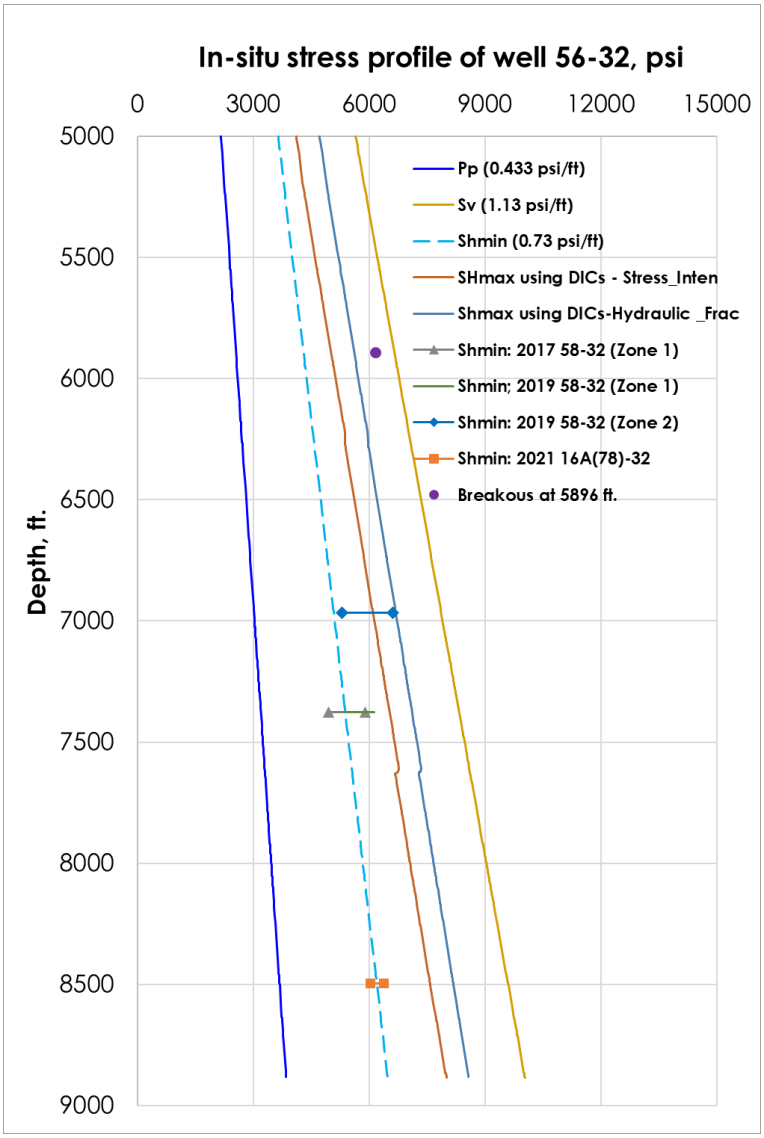

Fig. 22. In situ stress profile in well 56-32. The brown line is the S_{Hmax} using the method of fracture mechanics and the dark blue line is S_{Hmax} using Kirsch solution based on hydraulic fracturing mechanism. The gradient of S_v and P_p are 1.13 psi/ft and 0.433 psi/ft. The purple dot is the S_{Hmax} result using the breakout based Kirsch solution. The S_{hmin} gradient is the average of DFIT from the injection zone in well 16(A)78-32.

Table. 4 The average gradient of S_{Hmax} in well 56-32 range from 0.82 to 1.05 psi/ft from all methods.

Well Name	Well pressure type	S_{Hmax} gradient (P_f=P_p), psi/ft	S_{Hmax} gradient (P_f=P_{stc}), psi/ft	S_{Hmax} gradient (Kirsch Solution Based on Hydraulic Fracturing Mechanism), psi/ft	S_{Hmax} Gradient (Kirsch Solution Based on Breakout), psi/ft
56-32 Depth: 3800-8900	Using P_{dyn}	0.72-0.9 Avg: 0.86	0.68-0.85 Avg: 0.82	0.9-0.97 Avg: 0.95	1.05

In Fig. 22, the model of S_{Hmax} in well 56-32 is presented. For this vertical well, two methods were used: the green line is the S_{Hmax} results calculated from the fracture mechanics and the red line using the Kirsch solution. Both stress profiles of S_{Hmax} shows a normal fault regime. S_{Hmax} using the Kirsch method is larger than it is using the fracture mechanics method. Well 56-32 has a S_{Hmax} gradient of 0.82 psi/ft to 1.05 psi/ft and this result is consistent with other vertical wellbores.

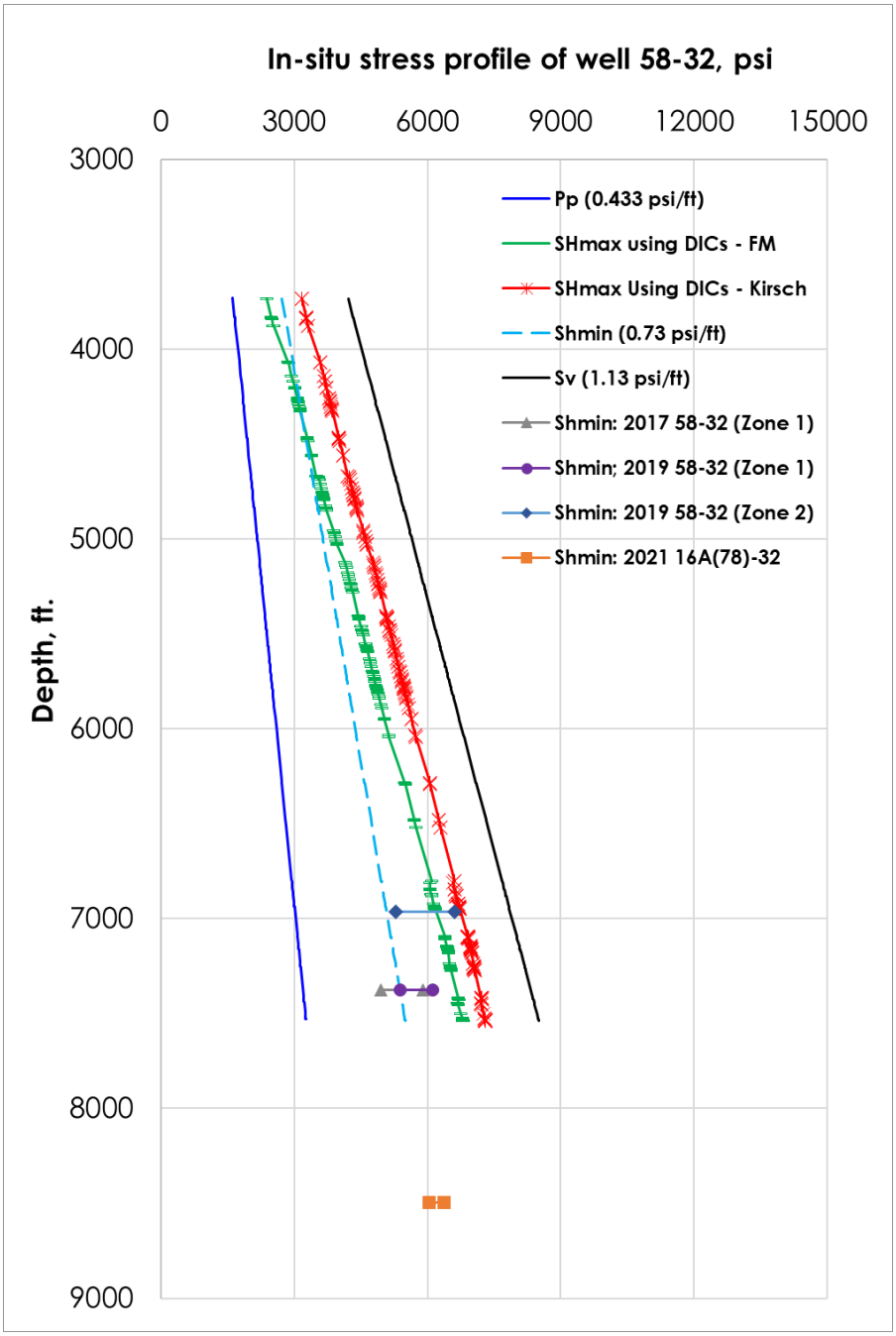

Fig. 23. In situ stress profile in well 58-32. The green line is the S_{Hmax} using the method of fracture mechanics and the red line is S_{Hmax} using Kirsch solution based on hydraulic fracturing mechanism. The gradient of S_v and Pp are 1.13psi/ft and 0.433psi/ft. The S_{hmin} gradient is the average of DFIT from the injection zone in well 16(A)78-32.

Table. 5 The average gradient of S_{Hmax} in well 58-32 range from 0.80 to 0.94 psi/ft from all methods.

Well Name	Well pressure type	Avg S_{Hmax} gradient (P_f=P_p), psi/ft	Avg S_{Hmax} gradient (P_f=P_{stc}), psi/ft	Avg S_{Hmax} gradient (Kirsch Solution Based on Hydraulic Fracturing Mechanism), psi/ft
58-32	Using P_{dyn}	0.64-0.9 0.83	0.53-0.88 0.80	0.85-0.97 0.94

In Fig. 23, the model of S_{Hmax} in well 58-32 is presented. Two methods were used: green line shows the S_{Hmax} based on the fracture mechanics and the red line is calculated using the Kirsch solution. Both stress profiles of S_{Hmax} show a normal fault regime. Well 58-32 has a S_{Hmax} gradient of 0.80 psi/ft to 0.94 psi/ft and this result is consistent with other vertical wellbores.

Table. 6 The table displays S_{Hmax} gradient results for vertical wells using fracture mechanics-based method, Kirsch, and breakout based method. The breakout based Kirsch solution has greater gradients than DIFs based method.

Well Name / Methodologies	16(A)78-32		78B-32	56-32	58-32
Well Pressure Type	Using P_{dyn}	Using P_{stc}	Using P_{dyn}	Using P_{dyn}	Using P_{dyn}
Avg S_{Hmax} gradient (Fracture mechanics based; P_f=P_p), psi/ft	1.02	1.7	0.86	0.86	0.83
Avg S_{Hmax} gradient (Fracture mechanics based; P_f=P_{stc}), psi/ft	0.94	1.64	0.86	0.82	0.80
Avg S_{Hmax} gradient (Kirsch Solution Based on Hydraulic Fracturing Mechanism), psi/ft	N/A		1	0.95	0.94
S_{Hmax} Kirsch Solution Based on Breakout	N/A		0.92 and 1.04	1.05	N/A

In all vertical wells, the S_{hmin} from zone 2 often is greater than S_{Hmax} results from S_{Hmax} based on the fracture mechanics method. This can be caused by the interaction between hydraulic fractures and natural fractures, which leads to a higher value of S_{hmin} (Kamali et al., 2019; Xing et al., 2020). Thus, the higher value of S_{hmin} from zone 2 can be seen as an exception of the S_{hmin} values. From all three vertical wells, the average S_{Hmax} gradients are between 0.80 to 1.04 psi/ft. This range is confined by using three different methods based on the observed well failures. These methods are fracture mechanicss, Kirsch solution with the use of drilling induced fractures and breakouts method, and the integration of thermal stress. It is reasonable that S_{Hmax} results based on the fracture mechanics are always less than the method based on the Kirsch solution because it is often easier to reopen a fracture than initiate a new fracture (Ye et al, 2022 and Yuan et al, 2022). Our range is also within the estimated range from a previous study in Utah FORGE which yield a S_{Hmax} range from 0.75 to 1.13 psi/ft (Finnila and Podgorney, 2020). By using the method based on DIFs and breakout in well 78B-32, the compressive strength is confined and S_{Hmax} can be constrained using breakouts. A more realistic range of effective compressive strength in Utah FORGE is 5300-8000 psi.

STRESS INVERSION ANALYSIS BASED ON FOCAL MECHANISM.

OBJECTIVE

The objective of this chapter is to calculate the magnitude and direction of in situ principal stress S_{Hmax} using the focal mechanism. The inputs to this problem are six moment tensor parameters which are obtained by the processing of seismic sensor data. The source of seismic sensor data is the seismicity from injection tests or natural earthquakes.

$$\varphi = 1 - R = \frac{\sigma_2 - \sigma_3}{\sigma_1 - \sigma_3} \quad \text{Eq. 29}$$

$$\begin{bmatrix} \sigma_1 - \sigma_3 & \sigma_{12} & \sigma_{21} \\ \sigma_{21} & \sigma_2 - \sigma_3 & \sigma_{23} \\ \sigma_{31} & \sigma_{32} & \sigma_3 - \sigma_3 \end{bmatrix} \quad \text{Eq. 30}$$

To calculate S_{Hmax}, a stress inversion method is performed to find the differential stress ratio, R or φ. Then when Sv, Sh are known, S_{Hmax} can be calculated from φ. The direction of S_{Hmax} is also calculated using the deviatoric stress tensor (Eq. 30). The detailed magnitude and direction calculation of S_{Hmax} using focal mechanism are described in the Appendix.

INTRODUCTION

Stress inversion based on focal mechanisms uses focal mechanism data to compute stresses on an active fault to estimate in-situ principal stresses. When computing in situ stresses from an active fault only differential in situ stress tensors are available. Differential (at times called deviatoric) stress tensor can only yield a relative stress ratio as the final solution of focal mechanism-based stress analysis.

The focal mechanism is driven by earthquake seismic data and is an analysis done by using the moment tensors. The focal mechanism describes the slip movement and the fault orientation in an earthquake and they are represented by beach ball plots. Fig. 17 demonstrates the beachball representation of each fault type.

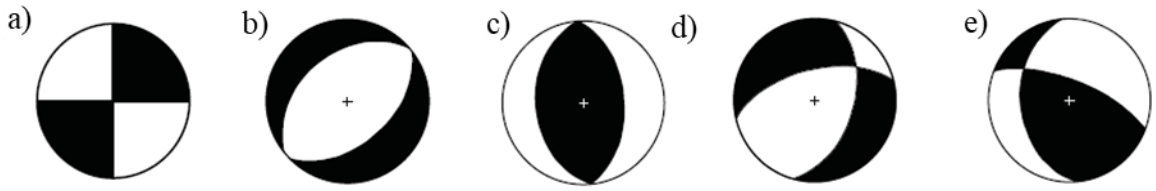

Fig. 17. Beachball plot representing the type of faults. A) strike slip fault. B) normal fault. C) reverse fault. D) oblique fault with normal slip e) oblique fault reverse slip (Cronin, 2004).

The moment tensor is a 3 by 3 matrix which tells the magnitude of the deformation of the formation in the source location. The moment tensor is produced by using Green's function. Green's function converts sensor data into fault movements (Tierney, 2023). A stress inversion analysis uses the focal mechanism to calculate the state of the stress in the formation based on the Wallace-Bott criterion, which assumes that the fault slip vector is parallel to the maximum shear stress in the fault plane. The result of stress inversion is called stress ratio and is defined as R (Martínez-Garzón, 2016). The program of MSASTI also produces the directions of principal stresses and its mechanism is to calculate the angle of horizontal principal stresses with respect to true north (Martínez-Garzón, 2016). A more detailed explanation of stress inversion analysis, the use of the Wallace-Bott criterion and principal stress direction are described in the Appendix. In a word, with the value of R and other principal stress magnitudes the value of S_{Hmax} can be computed using Eq. 29. For instance, if the value of S_v and S_{hmin} are known and they correspond to values of σ_1 and σ_2 in a normal fault regime then the vlaue of S_{Hmax} can be calculated using Eq. 29.

GEYSER EXAMPLE

Due to a lack of focal mechanism data for Utah FORGE, this research did not perform stress inversion for Utah FORGE based on focal mechanisms. However, there is a need to validate the stress inversion method so that it can be used in the future when focal mechanism data is available for the Utah FORGE reservoir. The stress inversion is conducted using two packages called MTfit and MSASTI (Pugh, 2017 and Martínez-Garzón, 2016). These packages require stress tensor or focal mechanism data as inputs. To illustrate their utility and perform a quality check, we performed a stress inversion analysis on the Geysers geothermal reservoir. By doing so we studied the principal stress variations in both temporal and spatial distributions at the Geysers geothermal field. And the results are confirmed with the existing results from reliable literature. The source of

Geysers moment tensor data and injection data used in this project is publicly available from Northern California Earthquake Data Center (https://ncedc.org/outgoing/dreger/).

First, the moment tensors data from Geyser are converted into dip directions, dip angles, and rake on the faults plane where the seismic event is present and these processes are conducted by a Python program called MTfit. Then dip directions, dip angles, and rake are called fault plane angles and are used as the input data for the consequent package called MSASTI.

MTfit has various functions that can solve fault plan angles. In this study the moment tensor is converted into T, N, and P axes vectors. Then these vectors are used to calculate the fault normal and slip vector on the fault plane by using fault plane geometry. Finally, MTfit uses fault normal and slip vectors to compute the strike, dip angle, and rake (Pugh, 2017). The details of the mathematics of MTfit and MSASTI are explained in the Appendix.

Following MTfit, the SASTI package is then used to calculate stress inversion based on the Wallace-Bott criterion. The program requires fault plane angles as input data. To reduce the overfitting of the data, the grid search algorithm is also used to address the heterogeneity of the data. Grid searches divide a set of heterogeneous data into subsets and estimate the best-fit solution on each grid. All data must be assigned to grids. Grids also represent the spatial and temporal relationships between seismic events.

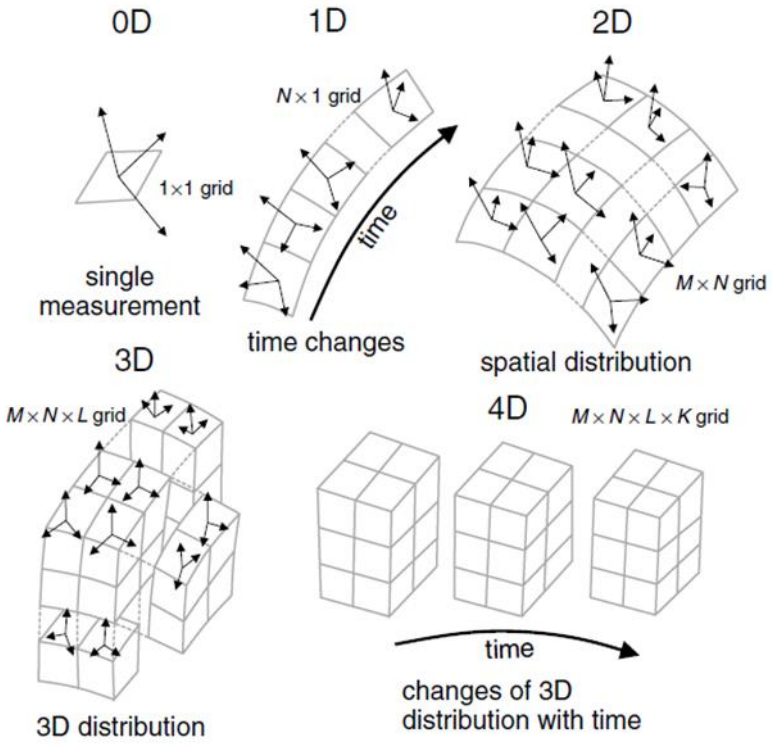

Fig. 18. 0D to a multi-dimensional representation of gids for the SASTI program (MartíNez-Garzón et al., 2013).

Grids Representation

In this project, since each seismic event happens at different depths and spans across different times, the grids are designed in spatial and temporal distributions. The spatial distribution is a 3D problem while temporal distribution is a 1D problem (Martínez-Garzón, et al, 2014).

For the spatial distribution, the input data is arranged based on the structure of the reservoir, meaning the reservoir is divided into the same depth of intervals and each interval is assigned as a grid (Garzón et al., 2013). For the first grid, the depth ranges from the surface to the top of the lower temperature zone, and the second and the third grid divide the lower temperature reservoir into two depth intervals. The last two grids divide the hot temperature reservoir into two depth

intervals up to the bottom. This led to a grid's configuration of a $1 \times 1 \times 5$ matrix in X, Y, and Z coordinates (Table. 7 and Fig. 19).

For the temporal distribution, the fault plane data are separated into 7 time windows. The time windows are ordered by the injection time. They are pre injection, during, after injection, and restarting injection (Table. 7). After the rearrangement of the input grid distribution, the fault plane data is fed into SASTI pages. (Martínez-Garzón, et al, 2015).

Table. 7 The representation of temporal and spatial configuration for this project.

Temporal Distribution	Grid Representation	Spatial Distribution	Depth Interval, km	Grid Representation
Before injection	(0, 1)	Top of LTZ	1.2-2	(0, 1)
During Injection	(0, 2)	LTZ (Lower Temp Zone)	2-2.5	(0, 2)
During Injection	(0, 3)	LTZ (Lower Temp Zone)	2.5-2.7	(0, 3)
After Injection	(0, 4)	HTZ (Hot Temp Zone)	2.7-3	(0, 4)
After Injection	(0,5)	HTZ (Hot Temp Zone)	3 to 4	(0, 5)
After Injection	(0, 6)			
Restart Injection	(0, 7)			

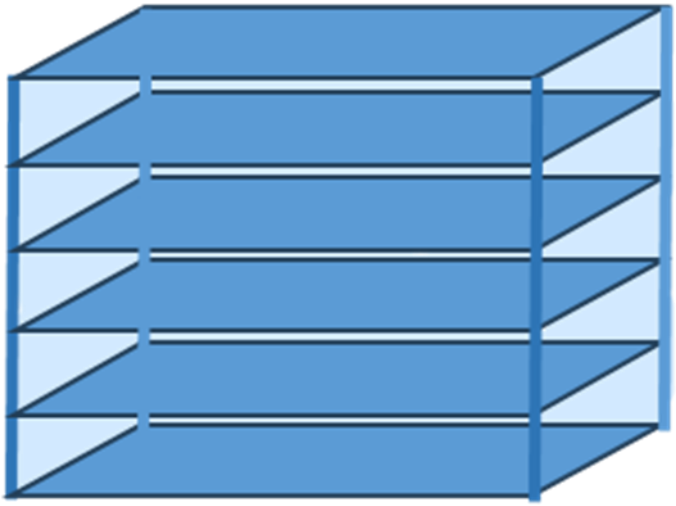

Fig. 19. The spatial representation of grids. The largest cube can represent the targeting formation and each sub deviation of the cube is a grid. Intervals are divided by the depth of the reservoir. For example, the top cube is one grid and the depth that divides this cube is from the surface to the top of the LTR (1.2 km to 2 km).

Running The Program for Geyser Data

In this project, the detailed procedure of using MTfit and SASTI package is in Appendix. The damping is not used for this project. The reason is that the purpose of this project is to study the changes of stresses within the reservoir, it is necessary to observe the precise results from each stress inversion results. Inversely, damping will remove the differences between each grid and hinder the differences between grid intervals. In addition, for the calculation of S_{Hmax} in the future, a precise result of relative stress is required as well thus it is not necessary to utilize damping for the S_{Hmax} estimation.

For the stereonet plot, the program uses bootstraps to show alternative solutions of the stresses. In this work, the number of bootstraps is reduced to at least 100. The reason I do it is because more

bootstraps prevent observation of possible alternative principal stresses. The results from 1000 bootstraps will give a fuller spectrum of possibility and there is no variation among each parameter. While the results from 100 bootstraps will show clearer alternatives between principal stresses and help to identify the variation of stereonets.

The dominant fault regime in the Geysers is the strike-slip fault regime (Boyd, et al). To calculate the relative stress ratio R accurately, I only selected the moment tensors that represents a SS fault regime for the input data. According to Boyd et al, a normal fault event has a rake angle between -45 to -135 degrees, a reverse fault has a rake between 45 and 135, and a strike slip fault has otherwise rake angles (2018). In a SS fault regime, the maximum horizontal stress is the maximum principal stress in the stress tensor. Thus, with known σ_2 and σ_3 and S_{Hmax} can be calculated using Eq. 29.

RESULTS AND DISCUSSION FOR GEYSER RESERVOIR

Stress Variations in Spatial And Temporal Distributions

In Geyser Reservoir, the approximate S_{Hmax} direction is N2E to N16E. The stress ratio, R, values are about 0.28. When knowing the S_v and S_h of the Geyser reservoir, S_{Hmax} can be calculated from $\varphi(\sigma_v - \sigma_h) - \sigma_h$. We then analyzed the results of R values and the variations of principal stresses based on the temporal and spatial distribution of the grids. The results will be compared to existing stress analysis in Geyser's reservoir. This analysis is done to confirm the correctness of this program of combined use of MTfit and SASTI programs.

In Fig. 30, the stereonet diagrams show the principal stresses σ_1 as a red dot, σ_2 as green dots and σ_3 as blue dots and each diagram represents each grid in the order of injection time. Fig. 30 is in the order of temporal distribution, σ_3 shows a tendency to approach N90E during the pre-injection to after injection. σ_1 direction shows a counterclockwise rotation from the pre injection to after

injection. These changes are also observed in the research of Boyd et al (2018). The principal stress directions show that the reservoir has a strike-slip fault regime but gradually becomes a normal fault regime as injection continues. From Fig. 30 a) to d), σ_1 is seen as red dots having an orientation of NE and σ_2 has an orientation of 90 degrees. This indicates a strike slip fault regime because S_v is vertical and is the second largest stress. Then as pointed out by Boyd et al., in the Fig. 30e), σ_1 , shown as red dots, become vertical, which means the fault mechanism becomes normal after the injection continued and stopped for a while. Martínez-Garzón et al. also confirmed this normal fault mechanism during peak injection time (2013). However, when restarting the injection again the fault regime becomes a trans tensional regime where faults are composed of both normal and strike-slip. This can be observed at the equal probability of σ_1 and σ_2 on each side of stereonet in Fig. 30 f) and g) (Boyd et al, 2018).

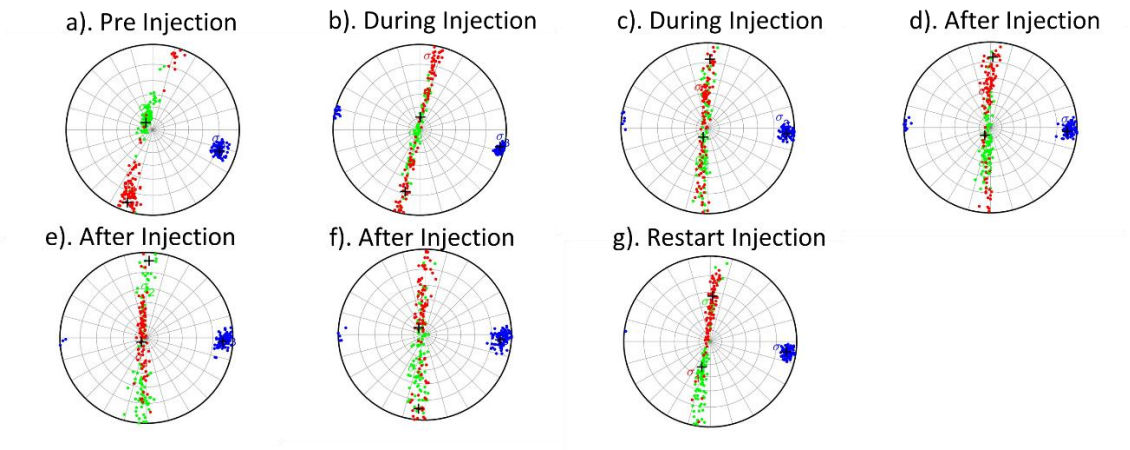

Fig. 30. Stereonet showing principal stresses directions in temporal distribution (Martínez-Garzón, et al., 2014). Before injection, the reservoir is in a strike-slip fault mechanism. As injection goes on the fault mechanism gradually becomes a mixture of normal and strike-slip. This can be seen by the uniformly mixed possibility of normal and strike slip fault in the stereonets b) and c). During injection, σ_1 has an increasing possibility of becoming vertical, which indicates an increase in the normal fault regime. Moreover, the fault mechanism then becomes normal after injection eased for not long (Boyd et al, 2018). This can be seen in e) in the after injection window. The majority of σ_1 is vertical meaning the dominant fault regime is normal after injection eased for a short time. As the injection eased for a longer time, the stress regime starts to recover as shown in the f). In g), as injection restarted the reservoir has a trans tensional fault regime (Boyd et al, 2018).

From the spatial variations of stress analysis results shown in Fig. 31. In the Lower temperature reservoir (LTR), the fault mechanism is a mixture of strike-slip and normal fault. Above and below LHR, strike slip faults are common. In Fig. 31, the first and the last 2 rose diagrams show a strike-slip fault regime. This suggested the strike slip fault is most prevalent in the top and bottom of reservoirs, and a mix of strike slip and normal fault inside LTR. Martínez-Garzón et al's results were roughly aligned with our solutions. She discovered the reservoir has a strike slip regime above the reservoirs. Then in the reservoir's depth of about 1.9 km to 3.1km, the formation transits from normal to transnational. Below the reservoir, the formation has a regime of transnational to SS again. She stated that normal faults tend to exist from 2 to 3.7km, while strike-slip faults are common above and below the reservoir (2013).

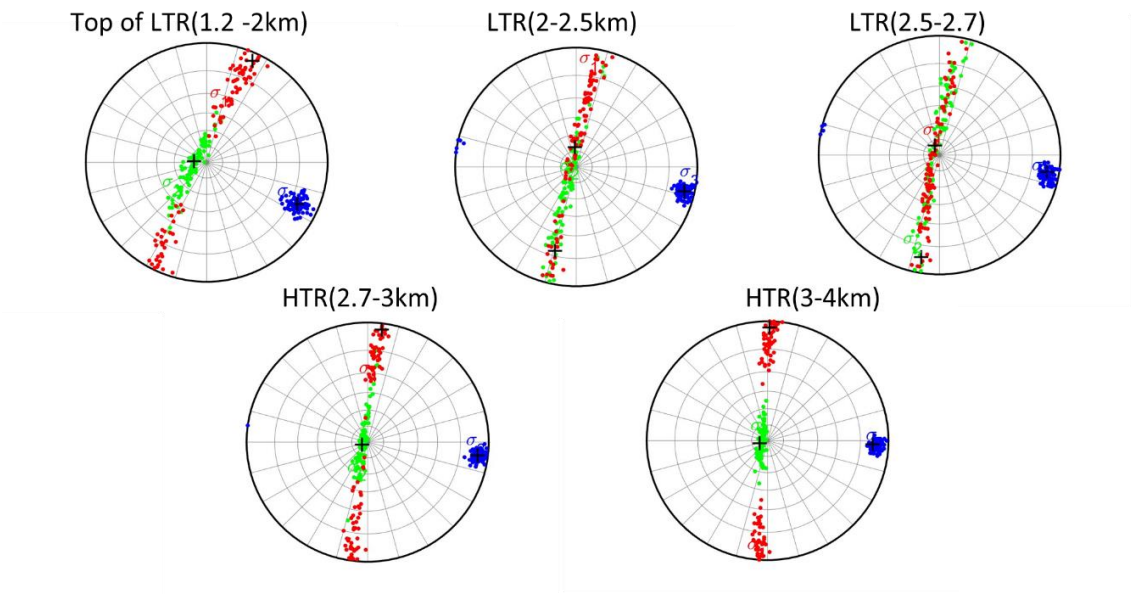

Fig. 31 Stereonet map shows principal stress variations in spatial distribution (Martínez-Garzón, et al., 2014). The top and the bottom of the LTR tend to be in a strike-slip fault regime. Within the LTR, the faulting regime is a mixture of normal and strike-slip. This roughly agrees with the result from Martínez-Garzón's result. She found that the top and bottom of the formation are in SS, and in between the fault regime transit from transtentional to normal and then to transtentional (Martínez-Garzón, et al, 2013).

Table. 8 a) and b). The R values and S_{Hmax} direction of the Geyser calculated in temporal distribution and spatial distribution. The average R is the average value of each grid. The range of S_{Hmax} direction is the value of the trend of each grid.

Temporal Distribution	Best R	Fault Regime Selected	Sig1 Direction
Before Injection	0.31	SS	N13.3E
During Injection	0.23	SS	N10.2E
During Injection	0.25	SS	N4.80E
After Injection	0.31	SS	N2.22E
After Injection	0.36	SS	N2.08E
After Injection	0.38	SS	N2.86E
Restart Injection	0.34	SS	N3.98E

a)

Spatial Distribution	Best R	Fault Regime Selected	Sig1 Direction
1km to LTZ	0.298	SS	N15.5E
LTZ (lower temp zone)	0.311	SS	N11.9E
LTZ (lower temp zone)	0.288	SS	N9.20E
HTZ (hot temp zone)	0.242	SS	N6.16E
HTZ (hot temp zone)	0.234	SS	N3.17E

b)

In Table. 8, the R value for both temporal and spatial distribution at each time window and layer. I only selected moment tensors that have strike slip fault regimes. Since in some grids the faulting regime is a mixture of normal and strike slip or trans tensional as shown in Figs 30 to 31, it is

easier to select only one type of regime and calculate the stress ratio. In this way the S_{Hmax} value can be calculated accurately with a known strike slip fault regime. The S_{Hmax} direction ranges from N2E to N16E. The range of S_{Hmax} orientation also is similar to the estimation done by Boyd et al. who concluded a S_{Hmax} orientation of 10 to 15 degrees (2018). They also stated that in Northwest Gayser, faults are complex and display different stress orientations and this causes the variety of S_{Hmax} stress estimation (Boyd et al., 2018).

CONCLUSION

For both vertical and horizontal wells, multiple methods are used to verify and constrain the results of principal stresses S_{Hmax}. A range of effective compressive strength is also estimated using DIF and breakouts in well 78B-32. In vertical wellbore, the methods used are fracture mechanics, Kirsch solution based on hydraulic fracturing mechanism, and Kirsch solution based on breakouts. In horizontal wellbore the methods used are: 3 equations and 3 unknowns using point failure and plan failure, linear regression method and focal mechanics method. Since Utah FORGE does not have moment tenor data to be used for focal mechanics based stress inversion, the result of S_{Hmax} in Utah FORGE using focal mechanism is reserved for future analysis. However, the program of MTfit and SASTI are implemented and are testified as reliable for future use.

The gradient of S_{Hmax} from each well and each method is listed below in Table. 9 The final range of S_{Hmax} in Utah FORGE based on our analysis ranges from 0.8 to 1.1 psi/ft. The direction of S_{Hmax} is estimated based on the rose diagram plotted by induced fractures in all vertical wells and has a range of N20E to N40E and an estimated average of N33E in direction. The range and orientation of S_{Hmax} coincide with the stress analysis done by Xing et al and Finnila and Podgorney. They have a range of 1.08- 1.38 psi/ft and 0.75-1.13 psi/ft respectively (2022 and 2020)

Table. 9 The table summarized average S_{Hmax} gradient using 4 different methodologies in both vertical and horizontal wells. Range of S_{Hmax} gradient ranges from 0.8 to 1.1 psi/ft based on both DIFs and breakouts.

Methodologies \ Well Name	16(A)78-32	78B-32	56-32	58-32
Well Pressure Type	Using P_{dyn}	Using P_{dyn}	Using P_{dyn}	Using P_{dyn}
Avg S_{Hmax} gradient (P_f=P_p), psi/ft	1.02	0.86	0.86	0.83
Avg S_{Hmax} gradient (P_f=P_{stc}), psi/ft	0.94	0.86	0.82	0.8
Avg S_{Hmax} gradient (Kirsch Solution Based on Hydraulic Fracturing Mechanism), psi/ft	N/A	1	0.95	0.94
Avg S_{Hmax} Kirsch Solution Based on Breakout	N/A	0.92 and 1.04	1.05	N/A
Avg S_{Hmax}Gradient (point and plan failure methods)	0.98	N/A	N/A	N/A

In Geyser geothermal reservoir, stress inversion using focal mechanisms is an example to solve the magnitude and direction of S_{Hmax} using focal mechanics. The use of combining MTfit and SASTI is successfully testified as a reliable method for stress analysis in Utah FORGE. In Geyser's reservoir our program computed the stress regime variation in the Geyser reservoir which correctly computed the stress regime change within the reservoir and during injection tests. The average R ratio in Geyser is 0.28 and a S_{Hmax} direction in the range of N2E to N16E. With known values of other major stresses, S_{Hmax} value can be computed using the R ratio.

REFERENCES

Allmendinger, Rick., 2020. Stereonet. Version11.

http://www.geo.cornell.edu/geology/faculty/RWA/programs/stereonet.html

Allis, Rick G., Joe Moore, Nicholas C. Davatzes, et al., 2016. EGS Concept Testing and

Development at the Milford, Utah FORGE Site. (2016). In *Proceedings Of 41st Workshop on Geothermal Reservoir Engineering*, Stanford University, Stanford, California, USA. February 22-24. SGP-TR-209

Barton, C. A., Zoback, M. D., and Burns, K. L., 1988. In-situ stress orientation and magnitude at

the Fenton Geothermal Site, New Mexico, determined from wellbore breakouts. *Geophysical Research Letters*, 15(5), 467-470. https://doi.org/10.1029/GL015i005p00467.

Bell, J. S., and D. I. Gough.,1983: The use of borehole breakouts in the study of crustal stress. *Hydraulic fracturing stress measurements* 201-209.

Blanksma, Derrick J., Blake, Kelly., Pettitt, Will., et al.,2018. Using Borehole Induced Structure

Measurements at Fallon FORGE Combined with Numerical Modeling to Estimate In-Situ Stresses. In *Proceedings,* Stanford University, Stanford, California, February 12-14, USA: 43rd Workshop on Geothermal Reservoir Engineering. SGP-TR-213.

Boyd, O. S., Dreger, D. S., Gritto, R., and Garcia, J., 2018. Analysis of seismic moment tensors

and in situ stress during Enhanced Geothermal System development at The Geysers geothermal field, California, *Geophysical Journal International*, vol. 215, no. 2, pp. 1483–1500. doi:10.1093/gji/ggy326.

Brudy, M. and Zoback, M. D., 1999. Drilling-induced tensile wall-fractures: implications for

determination of in-situ stress orientation and magnitude. *International Journal of Rock Mechanics and Mining Sciences.* vol. 36, no. 2, pp. 191–215. doi:10.1016/S0148-9062(98)00182-X.

Brody, M., and Kjorholt, H., 1999. The initiation of drilling-induced tensile fractures and their use for the estimation of stress magnitude. In *Vail Rocks 1999, The 37th US Symposium on Rock Mechanics (USRMS)*.

Cronin, Vincent S., 2004. A Draft Primer on Focal Mechanism Solutions for Geologists.

DE Smith, 2006. Appendix A. Equations for Translating Between Stress Matrices, Fault

Parameters, and P-T Axes. https://thesis.library.caltech.edu/2060/1/AppendixA.pdf

Duboeuf, Laure., 2018. Injections de fluide dans une zone de faille (LSBB, Rustrel): sismicité induite et déformation asismique. Sciences de la Terre. Université Côte d'Azur. Français. ffNNT : 2018AZUR4002ff. fftel-01787649f

Finnila, Aleta and Podgorney, Robert, 2020. Exploring Hydraulic Fracture Stimulation Patterns in the FORGE Reservoir Using Multiple Stochastic DFN Realizations and Variable Stress Conditions. In *Proceedings,* Stanford University, Stanford, California, February 10-12, USA: 45th Workshop on Geothermal Reservoir Engineering. SGP-TR-216.

Fjær, E., Horsrud, P., Raaen, A.M. et al. 1992. *Petroleum Related Rock Mechanics*. London: Elsevier Science.

Jaeger, John Conrad., Cook, Neville G. W., Zimmerman, Robert., 2007. fourth edition. Fundamentals of rock mechanics. *Wiley.*

Kamali, A., Ghassemi, A., McLennan, J., and Moore, J., 2019. Analysis of FORGE DFIT Considering Hydraulic and Natural Fracture Interactions. In *Proceedings: 44th Workshop on Geothermal Reservoir Engineering.*

Lund, Björn and John Townend., 2007. Calculating horizontal stress orientations with full or partial knowledge of the tectonic stress tensor. *Geophysical Journal International.* Volume 170, Issue 3, Pages 1328–1335, https://doi.org/10.1111/j.1365-246X.2007.03468.x

Mark D. Zoback.,2007. *Reservoir Geomechanics,* New York, USA: United States of America by Cambridge University Press

MartíNez-Garzón, P., Bohnhoff, M., Kwiatek, G., and Dresen, G., 2013. Stress tensor changes related to fluid injection at The Geysers geothermal field, California*, Geophysical Research Letters*, vol. 40, no. 11, pp. 2596–2601. doi:10.1002/grl.50438.

Martínez-Garzón, Patricia., Kwiatek, Grzegorz., Bohnhoff, Marco. et al., 2014, MSATSI: A MATLAB Package for Stress Inversion Combining Solid Classic Methodology, a New Simplified User‐Handling, and a Visualization Tool. *Seismological Research Letters*. 85. 896-904. DOI:10.1785/0220130189.

Martínez-Garzón, P., Y. Ben-Zion, N.Abolfathian, G. Kwiatek, and M.Bohnhoff, 2016., A refined methodology for stress inversions of earthquake focal mechanisms, *J. Geophys. Res. SolidEarth*,121, 8666–8687, doi:10.1002/2016JB013493.

Martínez-Garzón, Patricia., Kwiatek, Grzegorz., Bohnhoff, Marco. et al., 2014. MSATSI.

Mastin, L., 1988. Effect of borehole deviation on breakout orientations. *Journal Of Geophysical Research*, Vol. 93, No. Bs, Pages 9187-9195, August 10, Paper number 8B2111, 0148-0227/88/008 B-2111 $05.00.

McLennan, J., 2018a. Mechanical Properties Well 58-32. *U.S. Department of Energy the GDR Geothermal Data Repository.* Jul 22, DOI 10.15121/1557418

McLennan, John. 2018b. Utah FORGE: Stress Logging Data. United States. https://dx.doi.org/10.15121/1452760. https://gdr.openei.org/submissions/1032.

Michael, Andrew J., 1984. Determination of stress from slip data: Faults and folds. *Journal of Geophysical Research: Solid Earth, Volume 89, Issue B13, pp. 11,517-11,526.* DOI:10.1029/JB089IB13P11517

Nygren, A., & Ghassemi, A. "Influence of Cold Water Injection on Critically Stressed Fractures in Coso Geothermal Field, CA., 2005. " In *Proceedings: 40th U.S. Symposium on Rock Mechanics (USRMS)*, Anchorage, Alaska, USA.

Okabe, T., Hayashi, K., Shinohara, N., et al., 1998. Inversion of drilling-induced tensile fracture data obtained from a single inclined borehole. *International Journal of Rock Mechanics and Mining Sciences*, vol. 35, no. 6, pp. 747–758, 1998. doi:10.1016/S0148-9062(98)00001-1.

Pankow, K.L., Potter, S., Zhang, H., Trow, A.J., and Record, A.S., 2019, Micro-seismic characterization of the Utah FORGE site, in Allis, R., and Moore, J.N., editors, Geothermal characteristics of the Roosevelt Hot Springs system and adjacent FORGE EGS site, Milford, Utah: *Utah Geological Survey Miscellaneous Publication* 169-G, 10 p., https://doi.org/10.34191/MP-169-G.

Podgorney, R., Finnila, A., Simmons, S., et al. 2021. A Reference Thermal-HydrologicMechanical Native State Model of the Utah FORGE Enhanced Geothermal Site. *Energies*, 14, 4758. https:// doi.org/10.3390/en14164758

Pugh, D. J., 2016. Bayesian Source Inversion of Microseismic Events. https://doi.org/10.17863/CAM.15958

Pugh, David J, 2017, https://djpugh.github.io/MTfit/mtconvert.html

Rummel, F., 1987., Fracture Mechanics Approach to Hydraulic Fracturing Stress Measurements. *Fracture Mechanics of Rock.* Academic Press.

Schmitt, D.R., Zoback, M.D., 1989. Poroelastic effects in the determination of the maximum horizontal principal stress in hydraulic fracturing tests—A proposed breakdown equation employing a modified effective stress relation for tensile failure, *International Journal of Rock Mechanics and Mining Sciences & Geomechanics Abstracts*, Volume 26, Issue 6, Pages 499-506, ISSN 0148-9062, https://doi.org/10.1016/0148-9062(89)91427-7.

Sone, Hiroki., Zoback, Mark D., 2014. Viscous relaxation model for predicting least principal stress magnitudes in sedimentary rocks, *Journal of Petroleum Science and Engineering*, Volume 124, Pages 416-431, ISSN 0920-4105, https://doi.org/10.1016/j.petrol.2014.09.022.

Stephens, G. and Voight, B.,1982. Hydraulic Fracturing Theory for Conditions Of Thermal Stress. *In International Journal of Rock Mechanics and Mining Sciences & Geomechanics Abstracts*, 19 (6): 279-284. ISSN 0148-9062, https://doi.org/10.1016/0148-9062(82)91364-X.

Tape, Walter and Tape, Carl., 2013. The Classical Model for Moment Tensors. *Geophysical Journal International*. DOI: 10.1093/gji/ggt302

Tape, Walter & Tape, Carl., 2012. A Geometric Setting for Moment Tensors. *Geophysical Journal International*. DOI: 10.1111/j.1365-246X.2012.05491.x

Thorsen, Kjetil, 2011.In situ stress estimation using borehole failures — Even for inclined stress tensor, *Journal of Petroleum Science and Engineering*, Volume 79, Issues 3–4, Pages 86-100, ISSN 0920-4105, https://doi.org/10.1016/j.petrol.2011.07.014.

Tierney, Stuart., 2023. Moment tensors – a practical guide. *mXrap, Australian Centre for Geomechanics* (accessed 29 6 2023). https://mxrap.com/2019/07/26/moment-tensors-a-practical-guide/

Utah FORGE, 2023. Utah FORGE. https://utahforge.com/ (accessed 23 June 2023).U.S. Department of Energy the GDR Geothermal Data Repository. https://gdr.openei.org/home (accessed 23, June 2023)

Utah FORGE, 2019b. Utah FORGE: Well 78-32 Capacity Test. June 19. DOI 10.15121/1542058

Xing, Pengju., Wray, Andy., Ignacio Velez Artega, et al., 2022 In-Situ Stresses and Fractures

Inferred From Image Logs At Utah Forge. In *Proceedings of 47th Workshop on Geothermal Reservoir Engineering*, Stanford University, Stanford, California, February 7-9, Sgp-Tr-223.

Xing, Pengju, John McLennan, and Joseph Moore. 2020. In-Situ Stress Measurements at the Utah Frontier Observatory for Research in Geothermal Energy (FORGE) Site. *Energies* 13, no. 21: 5842. https://doi.org/10.3390/en13215842

Xing, Pengju. Winkler, Duane. Rickard, Bill. Et al., 2020. Interpretation of In-Situ Injection Measurements at the FORGE Site. *45th Workshop on Geothermal Reservoir Engineering*. Stanford University, Stanford, California. SGP-TR-216

Ye, Zhi., Fang, Yuan., Ghassemi, Ahmad., et al, 2022. A Preliminary Wellbore In-Situ Stress Model for Utah FORGE. 56th U.S. Rock Mechanics/Geomechanics Symposium, Santa Fe, New Mexico, USA, June 2022. ARMA-2022-0272. https://doi.org/10.56952/ARMA-2022-0272

Yuan Fang, Zhi Ye, and Ahmad Ghassemi., 2022. Preliminary Wellbore In-situ Stress Models for Utah FORGE. *GRC Transactions*, Vol. 46.

Zoback, Mark D. and Peska, Pavel., 1995. Compressive and tensile failure of inclined well bores and Determination of in situ stress and rocks strength. *Journal Of Geophysical Research*, VOL. 100, NO. B7, PAGES 12,791-12, 81, JULY 10. doi:10.1029/95JB00319.

Zoback, M.D., Barton, C.A., Brudy, M., et al., 2003. Determination of stress orientation and magnitude in deep wells, *International Journal of Rock Mechanics and Mining Sciences*, Volume 40, Issues 7–8, Pages 1049-1076, ISSN 1365-1609, https://doi.org/10.1016/j.ijrmms.2003.07.001.

APPENDIX

STRESS ROTATION BASED ON ZOBACK AND PESKA, 1995

Rotation From Principal Stress Coordinates to The Geographic Coordinate

When in a declined wellbore, the well path is not aligned with a far field principal stress and to represent the wellbore stresses in terms of far field principal stresses, the principal stresses have to be rotated from in site stress coordinate, (x_s, y_s, z_s), to wellbore coordinate (x_b, y_b, z_b).

In order to represent far field principal stress tensors in the wellbore coordinates and apply the Kirsch solution, in situ stress tensors and coordinate rotation tensors need to be defined. In situ principal stress tensor is represented by Ss. It lies in the far field coordinate system, (x_s, y_s, z_s), Geographic coordinate (X, Y, Z) represented the true north and east and down; wellbore coordinate system (x_b, y_b, z_b) represents wellbore in spherical coordinate; Rotations matrix, R_s, which rotates geographic to in situ stress coordinate; Rotation matrix: R_b, rotates geographic coordinate to wellbore coordinate. Finally, wellbore stress tensor S_b in wellbore coordinate can be calculated and then applied to Kirsch solutions.

S_s is principal in situ stress tensor represented in far field principal stresses. They contain three principal stresses S_v, S_{Hmax} and S_{hmin}. They are expressed in in situ stress coordinates (x_s, y_s, z_s), S_b is in-situ stress tensor expressed in wellbore coordinates (x_b, y_b, z_b), and S_g is the in-situ stress tensor expressed in geographic coordinates (X, Y, Z).

In the geographic system, (X, Y, Z) is defined as South, North, and Down. This definition follows the use in Okabe et al (1998), and Zoback and Peska (1995) papers to ensure the correctness of the calculation processes.

In the far field stress coordinate, (x_s, y_s, z_s), lies the in-situ principal stresses S_v, S_{Hmax} and S_{hmin}. By the definition of Zoback and Peska, x_s corresponds to the maximum principal stress direction, y_s corresponds to intermedium principal stress direction, and z_s is in the direction of the minimum principal stress (1995).

For Utah FORGE, the stress regime is normal, thus the maximum stress S_v is vertical, and its direction is in x_s. The maximum horizontal stress S_{Hmax} has an optimal direction of N25E (Finnila, and Podgorney, 2020). The minimum stress is S_{hmin} and its direction is 90 degrees from S_{Hmax}.

In the wellbore stress coordinate, (x_b, y_b, z_b), z_b is defined as along the axis of the wellbore. y_b lies horizontally and intersects with the cross sectional plane perpendicular to the z_b axis. $x_b$is defined as pointing towards the bottom of the wellbore cross section plane.

Rotational matrix R_s rotates geographic coordinates (X, Y, Z) into in-situ stress coordinates (x_s, y_s, z_s). The rotation matrix can be computed by deploying Euler angel and using y convection rotation order. In the Euler angel, three rotation angles, α, β, λ should be found during rotation from the original coordinate to the new coordinate. For example, α rotates X, Y, Z into X', Y', Z' around X axis, β rotates X', Y', Z' around Y' to X'', Y'' and Z'', and lastly, λ is the angle rotating X'', Y'' and Z'' to x_s, y_s, and z_s. around Z'' axis. The rotation matrix R_s can then be computed using the trigonometric relationship between rotated coordinates. A detailed demonstration of computing R_s is presented from Eq. A1 to Eq. A5 and from Fig. A1 to Fig. A4.

In the same manner, R_b can be computed by following the Euler angel rule. R_b rotates geographic coordinates (X, Y, Z) into wellbore coordinates (x_b, y_b, z_b) and it requires the knowledge of angels of φ and δ. φ is the inclination angle of wellbore and δ is wellbore azimuth. The

demonstration of the calculating process of R_b can be found through Eq. A9 to Eq. A13 and Fig. A6 to Fig. A8

Fig. A1 to A43 demonstrate the process of coordinate rotation from geographic coordinate (X, Y, Z) into in-situ stress coordination (x_s, y_s, z_s). The purpose of the rotation is to acquire rotation angles δ, β, and ϒ and to testify to the correctness of the existing rotation matrix Rs.

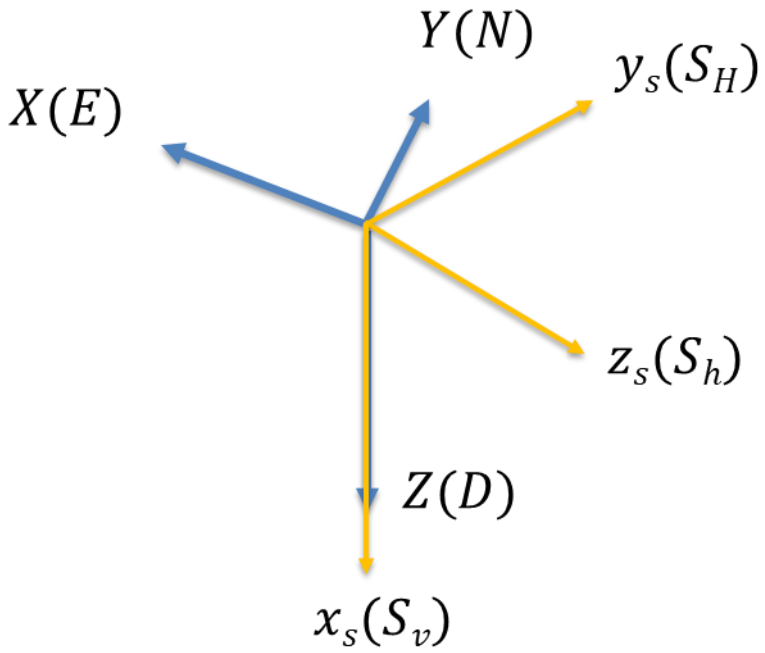

Fig. A1 The blue coordinate is the geographic coordinate and *Y* is in the true north direction, *X* is in the east direction, and *Z* is toward the downside. The yellow coordinate is in situ far field stress coordinate. x_s is the maximum principal stress and points down. y_s is maximum horizontal principal stress and it is in N25E. z_s is minimum horizontal stress it is

90 degrees apart from y_s. The stress tensor $S_s$in yellow coordinate is rotated into blue coordinate so that S_g can be calculated.

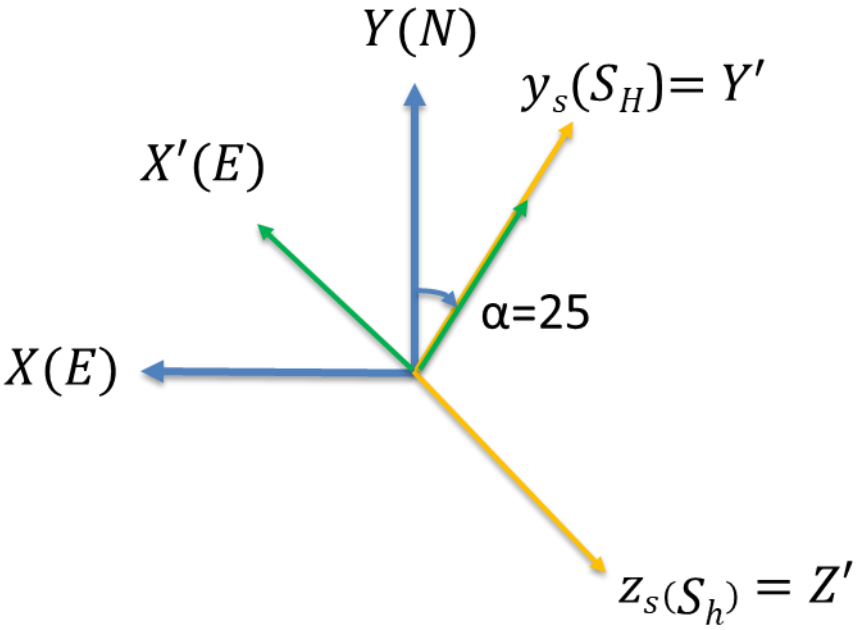

Fig. A2 The first rotation is around the *Z* axis. *X, Y, Z* rotate alpha angle to get *X', Y', Z'* so that *Y'* axis can be at y_s axis. The rotation obeys the right hand rule and σ is positive. The rotation matrix for the first rotation is $R_z(\alpha)$ and it rotates X, Y, X by an angle of alpha around *Z*-axis.

$$\begin{bmatrix} X' \\ Y' \\ Z' \end{bmatrix} = \begin{bmatrix} c(\alpha) & s(\alpha) & 0 \\ -s(\alpha) & c(\alpha) & 0 \\ 0 & 0 & 1 \end{bmatrix} \times \begin{bmatrix} X \\ Y \\ Z \end{bmatrix}, R_z(\alpha) = \begin{bmatrix} c(\alpha) & s(\alpha) & 0 \\ -s(\alpha) & c(\alpha) & 0 \\ 0 & 0 & 1 \end{bmatrix} \quad \text{Eq. A1}$$

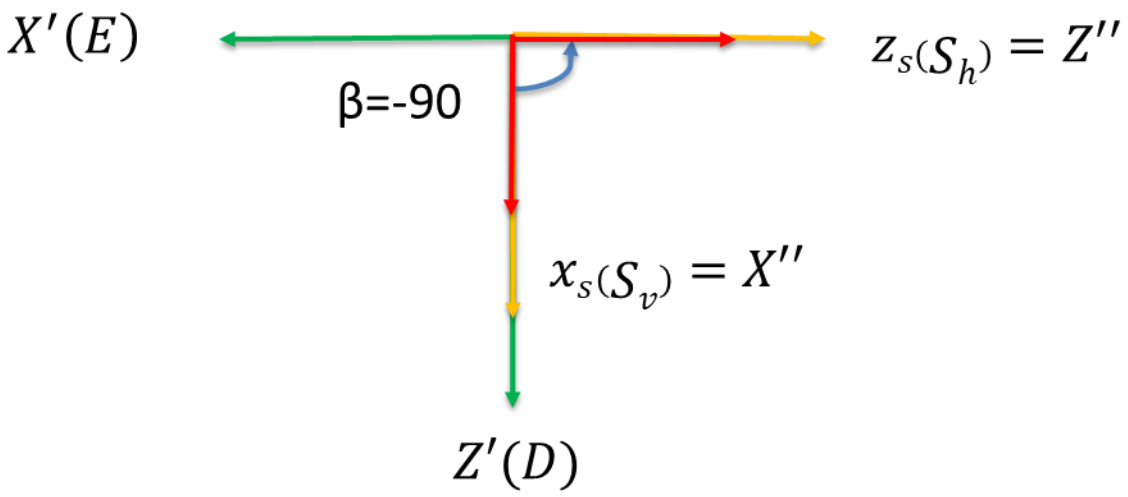

Fig. A3 The second rotation is around *Y'*. *X'*, *Y'*, *Z'* rotates towards *X''*, *Y''*, *Z''* with angle β. This rotation helps *X''* to become x_s and *Z''* to become z_s. The second rotation matrix R_y (β) rotates *X'*, *Y'*, and *Z'* by an angle of beta around the *Y'* axis.

$$\begin{bmatrix} X'' \\ Y'' \\ Z'' \end{bmatrix} = \begin{bmatrix} c(\beta) & 0 & -s(\beta) \\ 0 & 1 & 0 \\ s(\beta) & 0 & c(\beta) \end{bmatrix} \times \begin{bmatrix} X' \\ Y' \\ Z' \end{bmatrix}, R_y(\beta) = \begin{bmatrix} c(\beta) & 0 & -s(\beta) \\ 0 & 1 & 0 \\ s(\beta) & 0 & c(\beta) \end{bmatrix} \quad \text{Eq. A2}$$

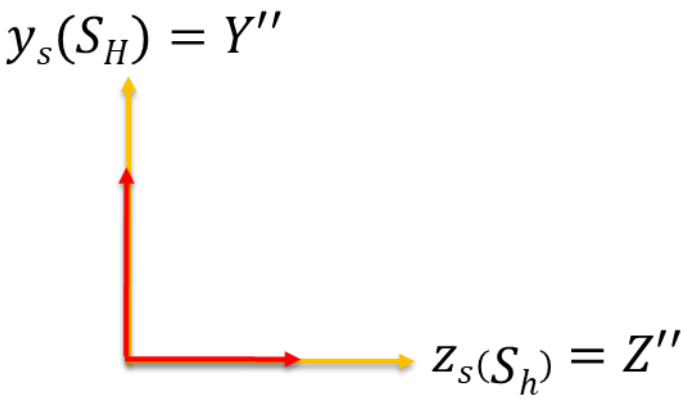

Fig. A4 The last rotation rotates around *X''* and since *X''*, *Y''*, *Z''* already become x_s, y_s, $z_s$at the previous rotation, the rotation gamma is 0. The third rotation matrix R_x (γ) rotates *X''*, *Y''*, and *Z''* by γ degrees around *X''* axis.

$$\begin{bmatrix} X''' \\ Y''' \\ Z''' \end{bmatrix} = R_x(\gamma) \times \begin{bmatrix} X'' \\ Y'' \\ Z'' \end{bmatrix}, R_x(\gamma) = \begin{bmatrix} 1 & 0 & 0 \\ 0 & c(\gamma) & s(\gamma) \\ 0 & -s(\gamma) & c(\gamma) \end{bmatrix} \quad \text{Eq. A3}$$

$$\begin{bmatrix} x_s \\ y_s \\ z_s \end{bmatrix} = \begin{bmatrix} X''' \\ Y''' \\ Z''' \end{bmatrix} = R_x(\gamma) \times R_y(\beta) \times R_z(\alpha) \times \begin{bmatrix} X \\ Y \\ Z \end{bmatrix} \quad \text{Eq. A4}$$

$$Rs = R_x(\gamma) \times R_y(\beta) \times R_z(\alpha) \quad \text{Eq. A5}$$

$$Rs = \begin{bmatrix} c(\alpha)c(\beta) & s(\alpha)c(\beta) & -s(\beta) \\ c(\alpha)s(\beta)s(\gamma) - s(\alpha)c(\gamma) & s(\alpha)s(\beta)s(\gamma) + c(\alpha)c(\gamma) & c(\beta)s(\gamma) \\ c(\alpha)s(\beta)c(\gamma) + s(\alpha)s(\gamma) & s(\alpha)s(\beta)c(\gamma) - c(\alpha)s(\gamma) & c(\beta)c(\gamma) \end{bmatrix} \quad \text{Eq. A6}$$

The R_s is the result of the rotation matrix multiplication of $R_x \times R_y \times R_z$ shown in Eq. A5. The order of rotation matrix multiplication is important. To examine the correctness of the rotation tensor R_s , the result of the R_s from my calculation is the same as the one driven by Zoback and Peska in their paper (1995). After ensuring the reliability of R_s, S_g can then be found successfully by applying Eq. A8.

$$Ss = RsSgRs^T \qquad \text{Eq. A7}$$

$$Sg = Rs^T SsRs \qquad \text{Eq. A8}$$

Rotation From Geographic Coordinates into Wellbore Coordinates

The same method applies to the rotation matrix R_b which rotates geographic coordinates (X, Y, Z) into wellbore coordinates (x_b, y_b, z_b). The process of calculating R_b is shown from Fig. A6to Fig. A8. Successful computing of R_b will be applied to Eq. A14 to calculate S_b.

In Fig. A5. an inclined wellbore geometry is shown. In wellbore coordinates, wellbore coordinates: (x_b, y_b, z_b), z_b is parallel to the wellbore axis. x_b points to the lowermost point on the cross-sectional plane that is perpendicular to the z_b. $x_b$is then 90 degrees from y_b. Since there is no way to define the direction of y_b by finding the intersection of cross section planes of the wellbore and horizon, $x_b$is found by using the toe direction of the well. Since the toe direction is the well azimuth direction, it also points to the highest point on the wellbore circumference. x_b is the opposite direction of the highest point of the wellbore, namely the lowest point on the wellbore. Thus, x_b is defined as the opposite direction of the well azimuth direction, shown in Fig. A6

In the well rotation matrix, angle δ is the azimuth of the well and it is also the direction of the well tow. δ is measured clockwise from the true north and this value can be found in the FMI log.

With known R_b rotation matrix and rotation angles δ and φ, S_g can be rotated to S_b by multiplying R_b and its inverse at its two sides. This equation is shown in Eq. A14.

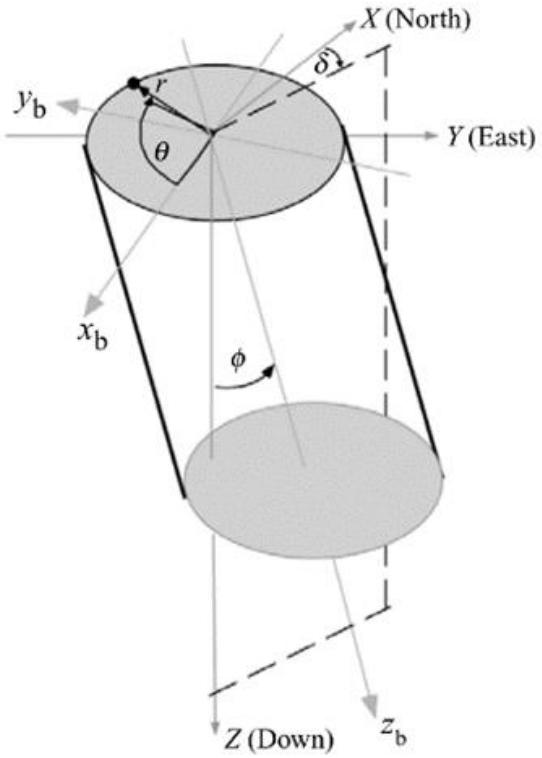

Fig. A5 Structure map showing wellbore geometry, wellbore, and geographic coordinates used by Zoback and Peska (1995).

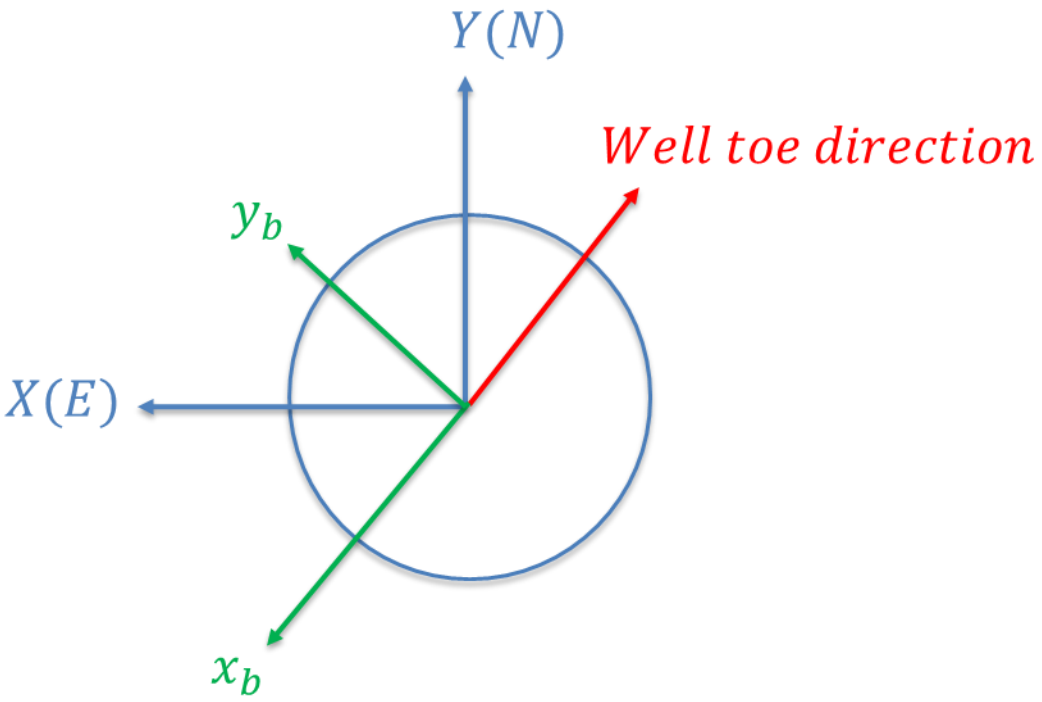

Fig. A6 x_b is found 180 degrees away from the well toe direction. y_b is 90 degrees from x_b direction.

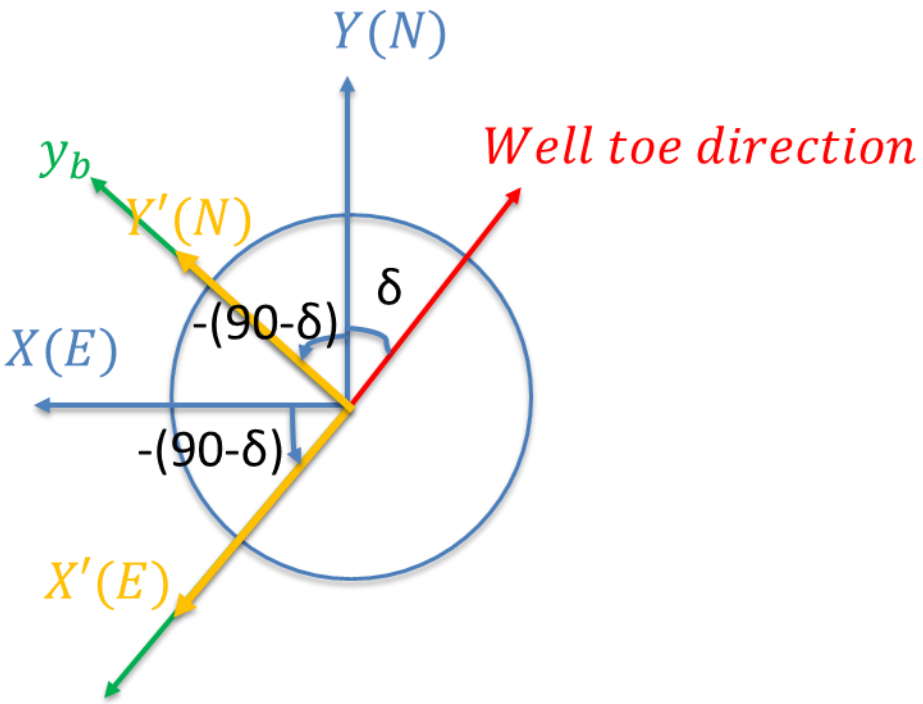

Fig. A7 The first rotation from geographic to wellbore coordinates. *X, Y, Z* are rotated to *X' Y'* and *Z'*. The equation used for rotation is the same as it is from *Rs*. The difference between Rsz and Rbz is the rotation angle.

$$\begin{bmatrix} x' \\ y' \\ z' \end{bmatrix} = \begin{bmatrix} c(-(90-\delta)) & s(-(90-\delta)) & 0 \\ -s(-(90-\delta)) & c(-(90-\delta)) & 0 \\ 0 & 0 & 1 \end{bmatrix} \times \begin{bmatrix} X \\ Y \\ Z \end{bmatrix},$$

$$R_z(\delta) = \begin{bmatrix} c(-(90-\delta)) & s(-(90-\delta)) & 0 \\ -s(-(90-\delta)) & c(-(90-\delta)) & 0 \\ 0 & 0 & 1 \end{bmatrix} \qquad \text{Eq. A9}$$

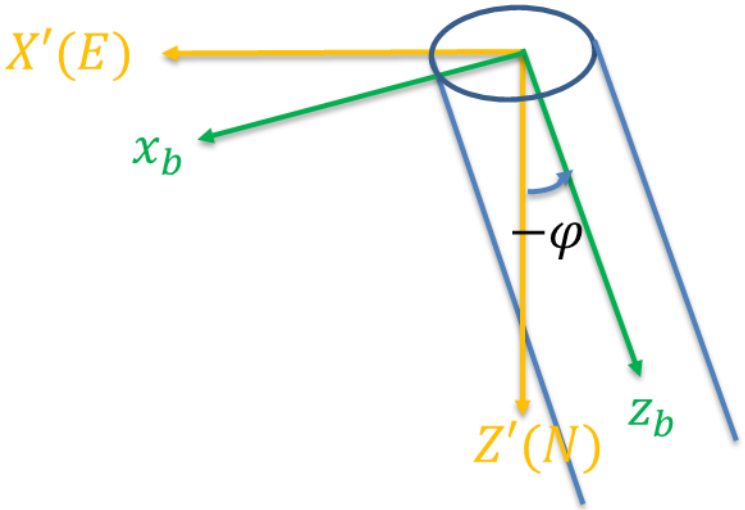

Case 1)

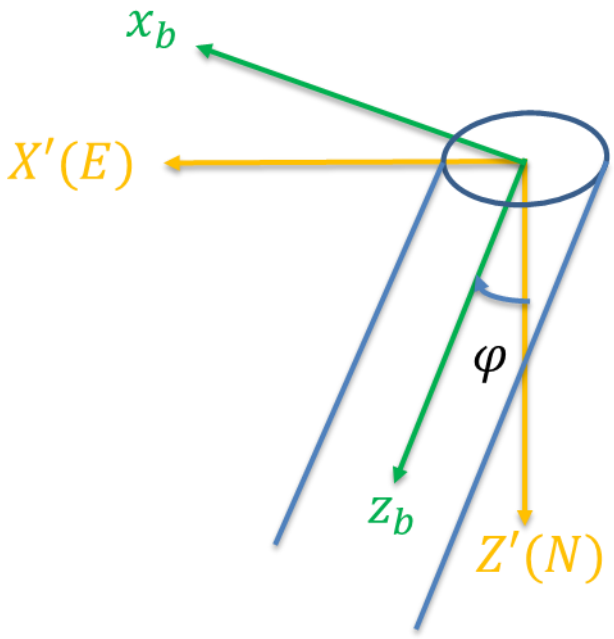

Case 2)

Fig. A8 The second rotation from geographic to wellbore coordinates. *X', Y', Z'* is rotated to x_b, y_b and z_b. The $R_y(\varphi)$ tensor used for rotation is the same as the $R_y(\beta)$ used in computing R_s. The difference between $R_y(\varphi)$ and $R_y(\beta)$ is the rotation angle φ. Case1 is for wellbore that inclines toward East and case2 is for the wellbore that inclines towards west.

$$\begin{bmatrix} xb \\ yb \\ zb \end{bmatrix} = \begin{bmatrix} c(-\varphi) & 0 & -s(-\varphi) \\ 0 & 1 & 0 \\ s(-\varphi) & 0 & c(-\varphi) \end{bmatrix} \times \begin{bmatrix} X' \\ Y' \\ Z' \end{bmatrix}, R_y(\varphi) = \begin{bmatrix} c(-\varphi) & 0 & -s(-\varphi) \\ 0 & 1 & 0 \\ s(-\varphi) & 0 & c(-\varphi) \end{bmatrix} \quad \text{Eq. A10}$$

$$\begin{bmatrix} xb \\ yb \\ zb \end{bmatrix} = R_y(\varphi) \times R_Z(\delta) \times \begin{bmatrix} X \\ Y \\ Z \end{bmatrix} \quad \text{Eq. A11}$$

$$R_b(\varphi, \delta) = \begin{bmatrix} \boldsymbol{c}(\varphi)s(\delta) & -c(\varphi)c(\delta) & s(\varphi) \\ c(\delta) & s(\delta) & 0 \\ -s(\varphi)s(\delta) & s(\varphi)c(\delta) & c(\varphi) \end{bmatrix}, \textit{case1} \quad \text{Eq. A12}$$

$$R_b(\varphi, \delta) = \begin{bmatrix} \boldsymbol{c}(\varphi)s(\delta) & -c(\varphi)c(\delta) & -s(\varphi) \\ c(\delta) & s(\delta) & 0 \\ s(\varphi)s(\delta) & -s(\varphi)c(\delta) & c(\varphi) \end{bmatrix}, \textit{case2} \quad \text{Eq. A13}$$

R_b is calculated by multiplying $R_y(\varphi)$ *and* $R_Z(\delta)$ in Eq. A12 to A13. Case 1 is for well inclination rotating counterclockwise around y_b. Case 2 is for well with inclination rotating clockwise around y_b.

$$S_b = R_b R_s^T S_s R_s R_b^T \quad \text{Eq. A14}$$

By finding R_b, the in-site stress tensor S_b in wellbore coordinate can be found from geographic stress tensor S_g by rotating from in situ stress coordinate into geological and then to wellbore coordinate.

STRESS TENSOR ROTATION BASED ON OKABE ET AL., 1998

Rotation From Geographic Coordinates into Wellbore Coordinates

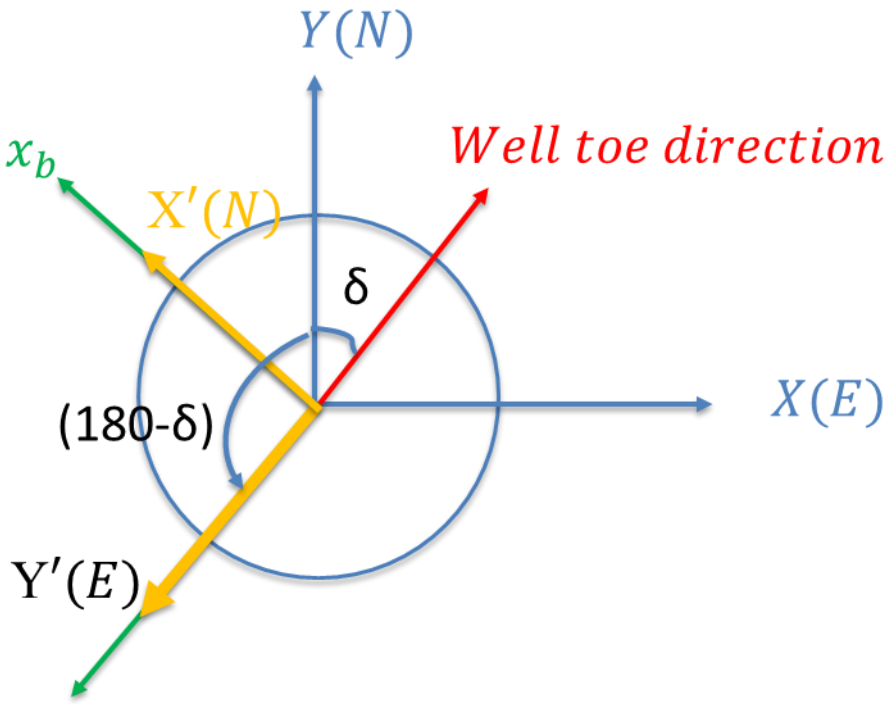

Fig. A9 The first rotation from geographic to wellbore coordinates around Z axis. *X, Y, Z* are rotated to *X' Y'* and *Z'*. The equation used for rotation is the same as it is from *Rs*. The difference between Rsz and Rbz is the rotation angle.

$$\begin{bmatrix} x' \\ y' \\ z' \end{bmatrix} = \begin{bmatrix} c(180-\delta) & s(180-\delta) & 0 \\ -s(180-\delta) & c(180-\delta) & 0 \\ 0 & 0 & 1 \end{bmatrix} \times \begin{bmatrix} X \\ Y \\ Z \end{bmatrix},$$

$$R_z(\delta) = \begin{bmatrix} c(180-\delta) & s(180-\delta) & 0 \\ -s(180-\delta) & c(180-\delta) & 0 \\ 0 & 0 & 1 \end{bmatrix} \quad \text{Eq. A15}$$

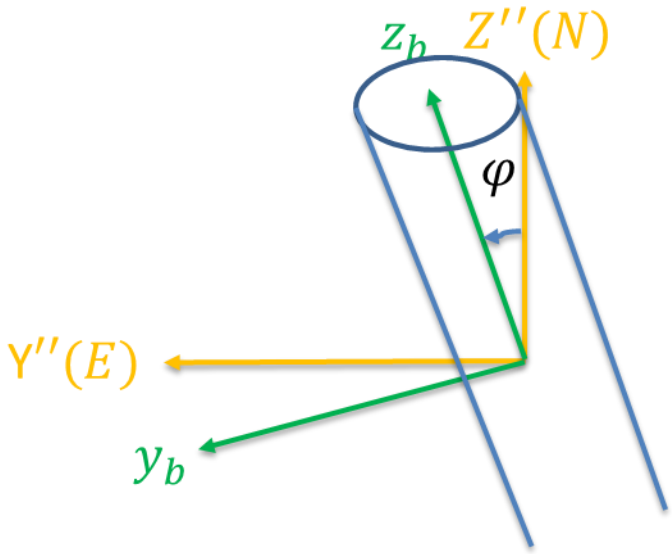

Fig. A10 The second rotation is around *X''*. *X'*, *Y'*, *Z'* is rotated to x_b, y_b and z_b. The $R_x(\varphi)$ tensor used for rotation is the same as the $R_x(\beta)$ used in computing R_s. The difference between $R_x(\varphi)$ and $R_x(\beta)$ is the rotation angle φ.

$$\begin{bmatrix} xb \\ yb \\ zb \end{bmatrix} = \begin{bmatrix} 1 & 0 & 0 \\ 0 & c(-\varphi) & -s(-\varphi) \\ 0 & -s(-\varphi) & c(-\varphi) \end{bmatrix} \times \begin{bmatrix} X' \\ Y' \\ Z' \end{bmatrix}, R_z(\varphi) = \begin{bmatrix} 1 & 0 & 0 \\ 0 & c(-\varphi) & -s(-\varphi) \\ 0 & -s(-\varphi) & c(-\varphi) \end{bmatrix} \quad \text{Eq. A16}$$

$$\begin{bmatrix} xb \\ yb \\ zb \end{bmatrix} = R_x(\varphi) \times R_Z(\delta) \times \begin{bmatrix} X \\ Y \\ Z \end{bmatrix} \quad \text{Eq. A17}$$

$$R_b(\varphi, \delta) = \begin{bmatrix} -\boldsymbol{c}(\delta) & s(\delta) & 0 \\ -s(\delta)c(\varphi) & -c(\delta)c(\varphi) & -s(\varphi) \\ -s(\delta)s(\varphi) & -c(\delta)s(\varphi) & c(\varphi) \end{bmatrix}, case1 \quad \text{Eq. A18}$$

LINEAR REGRESSION METHODS

According to Thorsen, the extended linear principal stress failure criteria can be used to calculate in situ stress with the use of drilling induced fracture angles and trace angles (2011). In Eq. A19 σ_1, σ_2, σ_3 are principal stresses and L function is failure criteria function. By the definition of extended linear principal stress failure criteria, once failure criteria L equals 0 failure will occur (Thorsen, 2011).

$$L(\sigma_1, \sigma_2, \sigma_3) = \begin{cases} c_1\sigma_1 + c_2\sigma_2 + f(\sigma_3), & \text{in compression} \\ c_1\sigma_3 + c_2\sigma_2 + f(\sigma_1), & \text{in tension.} \end{cases}$$

Eq. A19

The difference that separates Thorsen's method from the method used by such as Okabe is that Thorsen uses the principal stresses located on the coordinate of a fracture rather than the principal stresses on the wellbore (2011). They both require the rotation of in situ stresses from geographic coordinate into wellbore coordinates. Thorsen then further rotates wellbore stresses to the coordinates of the wellbore fractures (2011). Below in Eq. A20 are the principal stress equations in the fracture coordinates. α angle is the trace angle of the fracture and is measured from wellbore axis to the fracture plane (Thorsen, 2011).

$$\begin{aligned} \sigma_r^P &= \sigma_r \\ \sigma_\theta^P &= \sigma_\theta \cos^2\alpha + \sigma_z \sin^2\alpha + \sigma_{\theta z} \sin 2\alpha \\ \sigma_z^P &= \sigma_\theta \sin^2\alpha + \sigma_z \cos^2\alpha - \sigma_{\theta z} \sin 2\alpha. \end{aligned}$$

Eq. A20

Then plug in three principal stresses into extended linear principal stress equation L in Eq. A19 and equate it to 0. Then the equation becomes Eq. A21. According to Thorsen, wellbore pressure

P_w is σ_r in Eq. A20 and is one of the principal stresses on the fracture. P_w reaches the maximum when a fracture occurs. P_w reaches the minimum when a breakout occurs (Thorsen, 2011).

When the wellbore pressure causes the failure and $P_w = P_{wf}$, as well as when fracture initiation location is reached and $\theta = \theta_f$, L equation can be fulfilled. By taking the derivatives with respect to θ and α the locations of failures are defined, the L failure criteria is reached in Eq. A22 (Thorsen, 2011).

$$L = f(P_w) + (c_1\sigma_\theta + c_2\sigma_z)\cos^2\alpha + (c_1\sigma_z + c_2\sigma_\theta)\sin^2\alpha + \\ + (c_1 - c_2)\sigma_{\theta z}\sin 2\alpha = 0. \qquad \text{Eq. A21}$$

$$\partial_\theta L = 2\{[(c_1 + c_2)(1+\nu) + (c_1 - c_2)(1-\nu)\cos 2\alpha] \times \\ \times [(\sigma_X - \sigma_Y)\sin 2\theta - 2\sigma_{XY}\cos 2\theta] - \\ -(c_1 - c_2)\sin 2\alpha(\sigma_{XZ}\cos\theta + \sigma_{YZ}\sin\theta)\} = 0,$$

$$\partial_\alpha L = (c_1 - c_2)[2\sigma_{\theta z}\cos 2\alpha + (\sigma_z - \sigma_\theta)\sin 2\alpha] = 0. \qquad \text{Eq. A22}$$

$$\text{error} = \sum_{i=1}^{3}\left(a_{iH}\sigma_H^* + a_{ih}\sigma_h^* - a_{if}\right)^2 \qquad \text{Eq. A23}$$

After substituting three far field principal stresses into L functions by rotating geographic stress tensors into wellbore stress tensors. L equation then is a function of principal stress S_{Hmax}, S_h, S_v, and constants c, borehole orientation, principal in situ stress orientation, failure data (P_{wf}, α, θ_f), Poisson's ratio, and failure criterion parameters (c1, c2, f). For vertical wellbore, there are 4 unknowns, and they are S_{Hmax}, S_h, S_v, and in situ stress azimuth. They can be found by using linear regression of Eqs. A21 to A22 and then secondly by solving the error function in Eq. A23 (Thorsen, 2011).

However, if the well is inclined and there are at most 5 unknowns: S_{Hmax}, S_h, S_v, in situ stress rise direction, situ stress inclination and situ stress rise plane angle direction. Then at least 2 fractures can be used to calculate the in-situ stress solution for an inclined wellbore (Thorsen, 2011).

$$a_{\mathrm{H}}\sigma_{\mathrm{H}} + a_{\mathrm{h}}\sigma_{\mathrm{h}} = a_{\mathrm{f}}, \qquad \text{Eq. A24}$$

$$\sigma_i = s_i\sigma'_{\mathrm{ob}} + \beta P_{\mathrm{o}}, \quad \text{for } i \in \{\mathrm{H}, \mathrm{h}, \mathrm{v},\}, \qquad \text{Eq. A25}$$

In the inclined wellbore if the in-situ stress gradients are constant throughout the reservoir, Eq. A24 can generate 3 equations corresponding to three principal stresses equation in Eq. A25 at each failure. Then using at least 2 failures there will be 6 equations to produce a unique solution (Thorsen, 2011).

THE USE OF MTFIT PROGRAM

Step 1: Input

Input data is from the existing moment tensor components; they are 6 elements representing the moments in all directions on the fault plane. In this project, the convention is North (x), East(y), and Down(z). In this project, the moment tensor is given as an element in Excel. I used Python to rearrange tensor elements into a matrix format (Fig. A11).

Table. A1 Example of the header for the moment tensor inputs.

Mxx	Mxy	Myy	Mxz	Myz	Mzz
-0.191	-0.0231	-0.168	0.168	0.0959	-0.0672
-0.203	0.177	-0.155	-0.0704	0.0614	-0.0244
-0.0472	0.209	0.216	0.0856	-0.0548	0.0386

When tensor elements are fed into Python in the order presented above, the program below will rearrange the tensor into matrixes and then plug in the matrix into the MTfit function. In the last line, the outputs of the MTfit function will also be collected and stored in a new Excel sheet. Table. A2 shows an example of the output from MTfit.

```
pip install MTfit
```

...

```
import MTfit
```

```
import numpy

data=numpy.loadtxt(open("3by3tensorEQ.csv", "rb"), delimiter=",", skiprows=1)
                                    #"3by3tensorEQ.csv" is the csv file you created
data                                # disply the content in the file
```

```
MT=(0)*3                        #construct a new empty array with three 0s. MT=moment tensor
for row in data:                #loop through each row of the input file
    Ipt=[[row[0],row[1],row[3]],  # then rearrange each element in a row into a shape of 3 by 3 tensor
        [row[1],row[2],row[4]],
        [row[3],row[4],row[5]]]
    mt=MTfit.convert.moment_tensor_conversion.MT33_SDR(Ipt)  #apply MTfit ready to use funciton and plug in the tensors
                                # save the first result
    MT=numpy.vstack([MT, mt])   # stack each array of result into the empty array MT


MT=numpy.delete(MT,0)           #delet the first row becaue it is empty
#print(numpy.shape(MT))
MT=numpy.reshape(MT, (54,3))    # reshape MT array into 54 by 3 matrix
```

```
numpy.savetxt('sample.csv',RST, delimiter=",") #save the results of strike,slip angle and rake.
                                    #The file name "sample.csv" will be created after the running of the code
```

Fig. A11 Python program used to convert elements of moment tensors into fault plan angles and store them in Excel. The blue notations explain the function of each line of the code.

Output

Table. A2 The output from the MTfit program is the strike, dip angle, and the rake of the fault where seismic events are present.

Strike, radians	Dip Angles, radians	Rake, radians
3.74	0.52	0.15
3.88	0.89	-0.71
2.10	1.57	1.84
3.46	0.90	-0.65

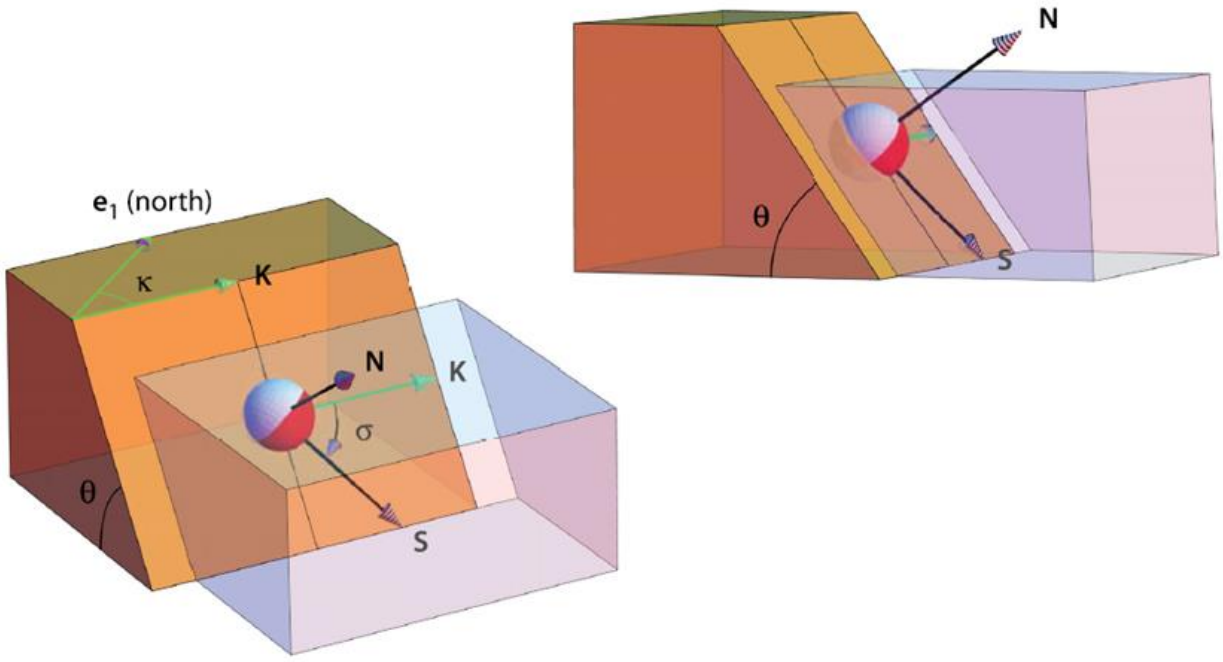

Fig. A12 Fault plane geometries and angles used in the MTfit package (Tape and Tape, 2012).

MTfit Functions

MTfit can convert moment tensor into fault plane angles, and they are fault strike, slip angle, and rake. The function I used is called: **MTfit.convert.moment_tensor_conversion.MT33_SDR(MT33)**. Below the table represents the processes and the mathematical explanation of this function.

Table. A3 The sub-functions used by the main function: MT33_SDR(MT33), which converts moment tensor to strike, dip, and rake angles (SDR) (Pugh, 2017).

In this project, only the main function mentioned above is used for calculating fault plan solutions. The steps below only apply specifically to this function.

Input	Main Function	Outputs
Moment Tensor – M	**MT33_SDR(M)**	**Strike, dip, and rake angles.**
	Subfunctions	
Moment Tensor – M	**MT33_TNPE(M)**	**T, N, P axes vectors and Eigenvalues**
T, P axes vectors	**TP_FP (T, P)**	**Fault normal (N1) and slip vectors(N2)**
Fault normal (N1) and slip vectors(N2)	**FP_SDR (N1, N2)**	**Strike, dip, and rake angles.**

MT33_TNPE(M)

Since the input moment tensor M is symmetric, and thus it has eigenvalues and eigenvectors (Eq. A26). T, N, and P axes vectors (e_1, e_2, e_3) is calculated from the eigenvalues of the moment tensor (Eq. A28). T axis vector (e_1) is the eigenvector of the largest eigenvalue of the moment tensor: Λ_1.

N axis vector (e_2) is the eigenvector of the intermediate eigenvalue: Λ_2. P axis vector (e_3) is the eigenvector of the smallest eigenvalue: Λ_3 (Eq. A27) (Tape and Tape, 2013).

$$M = \begin{pmatrix} \Lambda_1 & 0 & 0 \\ 0 & \Lambda_2 & 0 \\ 0 & 0 & \Lambda_3 \end{pmatrix} \quad \text{Eq. A26}$$

$$\Lambda_1 \geqslant \Lambda_2 \geqslant \Lambda_3 \quad \text{Eq. A27}$$

$$M = \Lambda_1 \boldsymbol{e}_1 \boldsymbol{e}_1^{\mathsf{T}} + \Lambda_2 \boldsymbol{e}_2 \boldsymbol{e}_2^{\mathsf{T}} + \Lambda_3 \boldsymbol{e}_3 \boldsymbol{e}_3^{\mathsf{T}}. \quad \text{Eq. A28}$$

TP_FP (T, P)

With given T and P axis vectors, the normal vector and slip vector on the fault plane can be calculated using the equations listed in the Table. A4.

Table. A4. The table presents the process of using T, and P axes vectors to calculate normal and slip vectors on the fault plane.

Symbols	**Equations** (Pugh, 2017)
N, normal vector on fault plane	$N = \frac{T + P}{\lvert T + P \rvert}$
S, slip vector on fault plane	$S = \frac{T - P}{\lvert T - P \rvert}$
T and P axes vectors	Given as input

FP_SDR (normal, slip)

With the given normal and slip vectors, based on the following equations in the Table. A5 the final results of strike angle, dip angle and rake can be found.

Table. A5. This table presents the process of calculating fault plane angles using fault normal and slip vectors.

Symbol	Definition	Equations (DE Smith, 2006)
K, Strike Angle	Measured from North to the strike	$\boldsymbol{\kappa = -tan^{-1}(\frac{n_N}{n_E})}$
θ, Dip Angle	Angle between fault plane and horizontal	$\boldsymbol{\theta = tan^{-1}(\frac{\sqrt{n_E{}^2 + n_N{}^2}}{n_U})}$
σ, Rake	Measured from horizontal to slip direction	$\boldsymbol{\sigma = cos^{-1}(\frac{\bar{n}\bar{u}}{\|\bar{n}\|\|\bar{u}\|})}$
$\boldsymbol{n_E, n_N, n_U}$	Fault normal vector (Pugh, 2015)	Given as input
$\boldsymbol{\bar{u}}$	Slip vector (Pugh, 2015)	Given as input

THE USE OF THE SASTI PROGRAM

Processes Overview

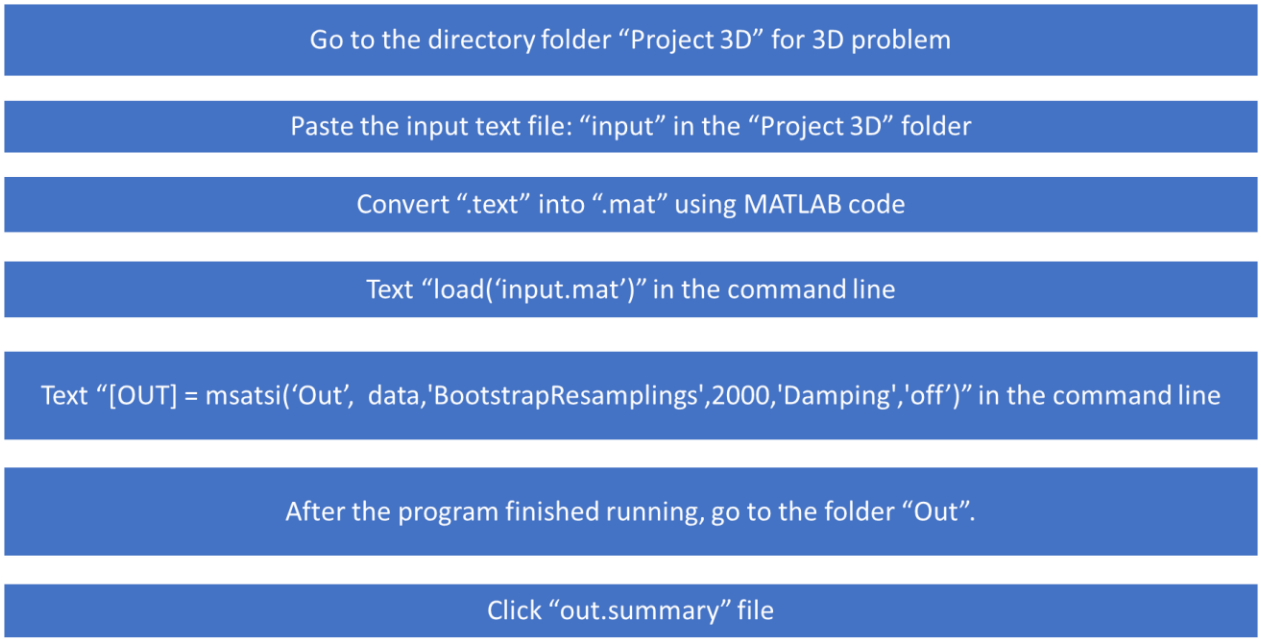

Fig. A13 This figure listed the essential processes of computing stress inversion in SASTI.

Step1: Input

The input data for MSATSI are dip direction, dip angle, and rake and they are the output from the MTfit program. The dip is the direction of the fault dipping; the direction of the dip is orthogonal to the strike of a fault plane, and thus the dip direction in degree is measured from north to the direction of the dip; the dip direction is the same as the azimuth of the dip. The dip angle is the angle of dip relevant to a horizontal plane. The rake is the angle between the axis of fault movement and the strike line. These angles are illustrated in Fig. A15.

When using the MSATSI package, the input data will be grouped into different subareas over different dimensions represented by grid points. For example, a single grid represents the 0D problem and it provides a set of the static stress field. The 1D problems have a series of grids and can display a temporal change of stress tensor change. 2D problem displays stress tensors in a surface. If the problem is 3D there will be an additional grid index to represent the special distribution of stress tensors.

```
0.0000000e+000  0.0000000e+000  2.7300000e+002  4.1000000e+001 -7.7000000e+001
0.0000000e+000  0.0000000e+000  1.1700000e+002  4.3000000e+001 -7.7000000e+001
0.0000000e+000  0.0000000e+000  1.2100000e+002  5.8000000e+001 -4.0000000e+001
0.0000000e+000  0.0000000e+000  2.6500000e+002  6.8000000e+001 -9.7000000e+001
0.0000000e+000  1.0000000e+000  1.6000000e+002  5.5000000e+001 -9.0000000e+001
0.0000000e+000  1.0000000e+000  2.0000000e+002  7.1000000e+001 -6.0000000e+001
0.0000000e+000  1.0000000e+000  3.3600000e+002  5.7000000e+001  1.5000000e+002
0.0000000e+000  1.0000000e+000  1.3500000e+002  7.1000000e+001  1.6800000e+002
```

Fig. A14 A sample input data for a 1D problem. The input format is in [X Y DIP_DIR DIP_ANGLE RAKE]. Xs are 0 and Ys are in the range of the number of grid points.

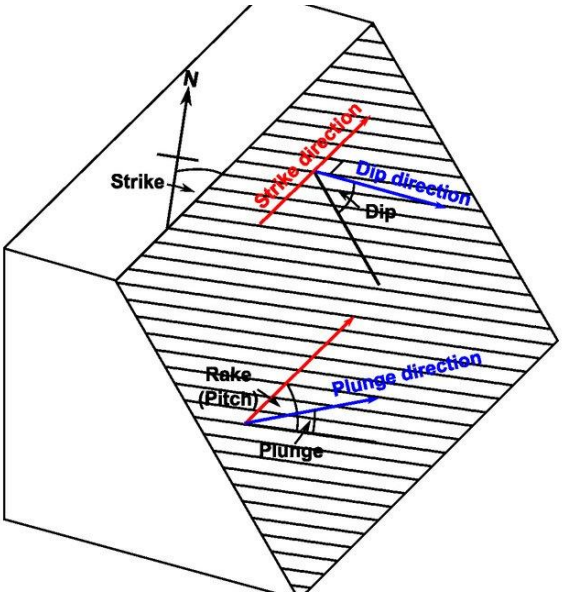

Fig. A15 Dip is the direction of the fault dipping; the direction of the dip is orthogonal to the strike of a fault plane, and thus the dip direction in degree is measured from North to

the direction of the dip. The dip angle is the angle of dip relevant to a horizontal plane. The rake is the angle between the axis of fault movement and the strike line (Duboeuf, 2018).

Default Requirements

There are some basic requirements and values for inputting data into the SASTI program. Fig. A16 displays these default values.

Table 1
Default and Typical Values of Parameters Controlling the Formal Stress Inversion with MSATSI

Description	Typical Values	Default Value
Minimum number of seismic events per grid point	30–45	20
Fraction of correctly picked fault planes	0.5–1	0.5
Number of bootstrap resamplings	1000–5000	500
Confidence interval	68%, 95%	95%

Fig. A16 The number of focal mechanisms should be 20 per grid point. For the second value, about 50% of the fault plane data can be accepted as inaccurate. The third value sets the number of iterations for resampling for uncertainty analysis (Martínez-Garzón et al., 2014).

Step 2 (Optional): Deciding the Damping Parameter. The damping parameter is processed in the file "satsi_tradeoff.exe". "satsi_tradeoff.exe" runs a function that calculates the dependency between model length and data misfit. The damping parameter is chosen when it results in the minimization of the combination of data misfit and model length.

Method: The minimum value of the combination of data misfit and model length is found on the Tradeoff curve (Fig. A18). The interaction between data misfit and model length is the best value of the damping parameter.

Step 3: Performing Stress Inversion. "satsi.exe" is then performed to calculate damped formal stress inversion. For each grid, the best deviatoric stress tenor orientations and the three principal stress axes are determined. The mathematics of stress inversion is explained in the later section of Damped Stress Inversion Mechanisms. The inversion takes place on each data grid at the same time. At last, it provides the relative magnitudes which are represented in terms of φ.

$$\varphi = 1 - R = \frac{\sigma_2 - \sigma_3}{\sigma_1 - \sigma_3} \quad \text{Eq. A29}$$

Step 4: Uncertainty Assessment. After the results of the best stress orientations and magnitudes are outputted from: "satsi.exe", the "bootmech.exe" operates uncertainty assessment. It randomly resamples from the original data, runs formal stress inversion, and creates new subsets.

Step 5: Final Results. Finally, the "bootuncert.exe" selects the subsets that are within a certain range of confidence. The best minimum and maximum values of stress magnitudes and orientations are the output of the program.

Output

For the output, the stress inversion results are stored in a matrix called [OUT]. The stress-related results can be extracted from the [OUT] matrix in a data format or they can also be represented graphically. Just by clicking on the [OUT] file in the result section of MATLAB. Inside [OUT], different results and their content can be found in the manual of the SASTI or Table. A6 below.

The second and third method is to use command code or you can get it directly from the dictionary folder. These results are the best solutions from each grid point. You can also get stress tensor output from a corresponding text file and they can be downloaded in the dictionary folder.

Table. A6 The selected outputs from the program. One can find them in the directory folder once the program is run.

Text files name	Content
Filename. out	The best result of stress tensor on each grid.
Filename. slboot_tensor	Stress tensor coordinates for each grid point and bootstrap.
Filename. slboot_trpl	Trend and plunge of the three principal stresses.
Filename. summary	Best min and a max of φ. Best values of principal stress axes.

The last method of extracting output is by plotting. By using msatsi_plot.m program, you can plot results for 0D to 3D problems.

For 0D to 1D results, you can plot the principal stress directions on a *Stereonet*. There are three principal stresses, which are σ_1, σ_2 and σ_3. *Profile* function can plot the directions variations of principal stresses directions over all grid points. The directions of principal stresses are plunge (dip angle) and trend (Azimuth).

For 2D results, *Seteromap* can be used to plot the axis of three principal stresses. *WSM* can plot the directions of S_{Hmax} according to the nearby faulting regime.

For 3D results, *Seterovolume* can be used to plot the rose diagram of three principal stresses.

STRESS INVERSION MECHANISMS IN MSASTI

This method of stress inversion is based on Wallace-Bott criterion. The assumption of this methodology is to minimize the differences between the slip vector ($\vec{s}$) and the calculated shear stress on each fault plane ($\vec{\tau}$). The slip vector is composed of the direction and the magnitude of the slip. The slip direction is towards the upper block moving with respect to the lower block on a fault. Shown in Eq. A30, the shear stress ($\vec{\tau}$) should be the same as the slip vector ($\vec{s}$) for an earthquake to happen on a fault plane.

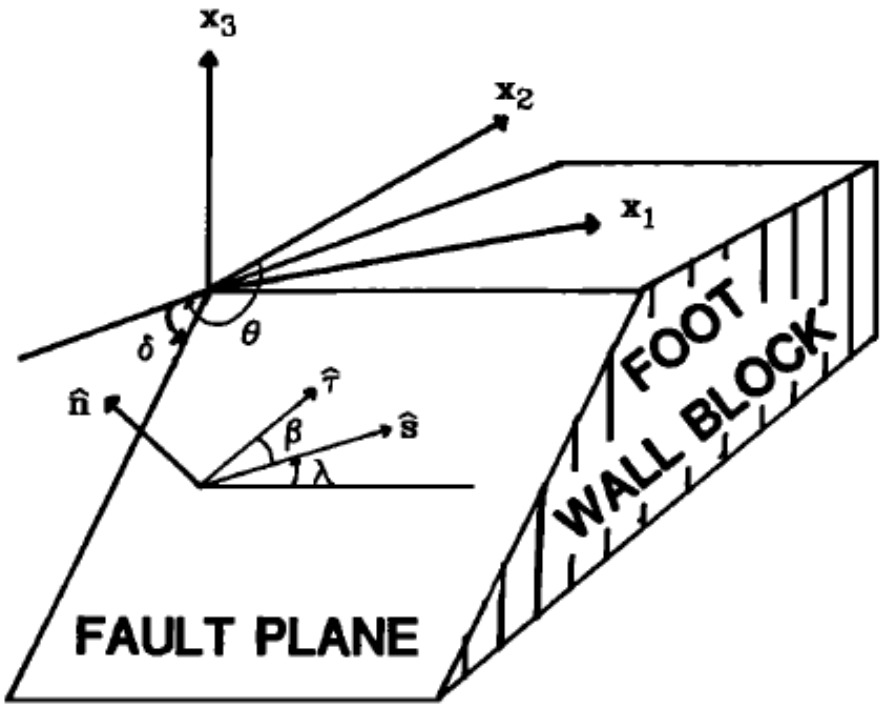

Fig. A17 Fault plane geometry and the representation of angles and vectors (Michael, 1984)

$$\vec{\tau} = \frac{\vec{\tau}}{|\vec{\tau}|} = \vec{s}$$ Eq. A30

The shear stress ($\vec{\tau}$) is calculated from stress tensor σ. First, the normal traction must be subtracted from total stress. It is represented in Eq. A31.

$$\vec{\tau} = \sigma\hat{n} - [(\sigma\hat{n}) * \hat{n}] * \hat{n}$$ Eq. A31

The inversion problem is solved using linear least square regression. However, $\vec{\tau}$ is linearly related to σ and thus the magnitude $|\vec{\tau}|$ is nonlinearly related to σ. To avoid nonlinearity, $|\vec{\tau}|$ is set to be 1. Then the problem becomes the minimization of $|\vec{\tau}| - 1$.

$|\vec{\tau}|$ represents the magnitude of the shear stress or the slip on a fault. $|\vec{\tau}|$ is set to be 1 because it is assumed that the slip motion happens during earthquakes, and it has a constant magnitude on each fault plan. Also, because only the relative magnitude of stresses can be estimated it is reasonable to assume all shear stress is 1.

$$\vec{\tau}=\vec{s} = \sigma\hat{n} - [(\sigma\hat{n}) * \hat{n}] * \hat{n}$$ Eq. A32

Then Eq. A30 becomes $\vec{\tau}=\vec{s}$ as $|\vec{\tau}|$ becomes 1, the final equation of the stress inversion problem becomes Eq. A32. In the matrix format, the equation is written as $Gm = d$.

$$d = \begin{pmatrix} s_{11} \\ s_{12} \\ s_{13} \\ \dots \\ s_{i1} \\ s_{i2} \\ s_{i3} \end{pmatrix}$$ Eq. A33

The d is the unit slip vector tensor; it contains all the unit slip vector components of all the faults. The slip vector S_{ij} has three components. I is the number of focal points; it ranges from 1 to K. J is the index of the stresses; it ranges from 1 to 3. The number of elements in d is 3*K; K is the number of focal mechanisms.

$$m = \begin{pmatrix} \sigma_{11} \\ \sigma_{12} \\ \sigma_{13} \\ \sigma_{22} \\ \sigma_{23} \end{pmatrix} \quad \text{Eq. A34}$$

The m matrix is the stress tensor. It has 5 stress components because the stress tensor is symmetric. It is also because knowing the slip vector on the fault can only constrain the deviatoric stress tensor, the isotropic tensor cannot be determined. Hence the isotropic tensor is assumed to be zero, and $\sigma_{33} = -(\sigma_{11} + \sigma_{22})$.

$$\begin{bmatrix} \sigma_{11} & \sigma_{12} & \sigma_{21} \\ \sigma_{21} & \sigma_{22} & \sigma_{23} \\ \sigma_{31} & \sigma_{32} & \sigma_{33} \end{bmatrix} = \begin{bmatrix} 0 & 0 & 0 \\ 0 & 0 & 0 \\ 0 & 0 & 0 \end{bmatrix} + \begin{bmatrix} \sigma_{11} & \sigma_{12} & \sigma_{21} \\ \sigma_{21} & \sigma_{22} & \sigma_{23} \\ \sigma_{31} & \sigma_{32} & \sigma_{33} \end{bmatrix} \quad \text{Eq. A35}$$

Eq. A33 shows the complete stress tensor and their separate parts: deviatoric stress tensor and isotropic stress tensor. In stress inversion, the isotropic tensor is assumed to be 0 and the inversion results give the deviatoric stress tensor or relative principal stress magnitude. However, the isotropic stress tensor can be calculated if S_v and S_h are known.

$$\mathbf{G} = \begin{pmatrix} n_{11} - n_{11}^3 + n_{11}n_{13}^2 & n_{12} - 2n_{11}^2 n_{12} & n_{13} - 2n_{11}^2 n_{13} & n_{11}n_{13}^2 - n_{11}n_{12}^2 & -2n_{11}n_{12}n_{13} \\ n_{12}n_{13}^2 - n_{12}n_{11}^2 & n_{11} - 2n_{12}^2 n_{11} & -2n_{11}n_{12}n_{13} & n_{12} - n_{12}^3 + n_{12}n_{13}^2 & n_{13} - 2n_{12}^2 n_{13} \\ n_{13}^3 - n_{13}n_{11}^2 - n_{13} & -2n_{11}n_{12}n_{13} & n_{11} - 2n_{13}^2 n_{11} & n_{13}^3 - n_{13}n_{12}^2 - n_{13} & n_{12} - 2n_{13}^2 n_{12} \\ \cdots & \cdots & \cdots & \cdots & \cdots \\ n_{K1} - n_{K1}^3 + n_{K1}n_{K3}^2 & n_{K2} - 2n_{K1}^2 n_{K2} & n_{K3} - 2n_{K1}^2 n_{K3} & n_{K1}n_{K3}^2 - n_{K1}n_{K2}^2 & -2n_{K1}n_{K2}n_{K3} \\ n_{K2}n_{K3}^2 - n_{K2}n_{K1}^2 & n_{K1} - 2n_{K2}^2 n_{K1} & -2n_{K1}n_{K2}n_{K3} & n_{K2} - n_{K2}^3 + n_{K2}n_{K3}^2 & n_{K3} - 2n_{K2}^2 n_{K3} \\ n_{K3}^3 - n_{K3}n_{K1}^2 - n_{K3} & -2n_{K1}n_{K2}n_{K3} & n_{K1} - 2n_{K3}^2 n_{K1} & n_{K3}^3 - n_{K3}n_{K2}^2 - n_{K3} & n_{K2} - 2n_{K3}^2 n_{K2} \end{pmatrix},$$

Eq. A36

In matrix G, n is the faulting normal vectors from each focal mechanism. For each n_{ki}, k is the number of focal mechanisms and i is the number of the component of the fault normal vector. The equation in G is driven from Eq. A32. The solution to the linear regression is to use the least square and the solution is in the form of:

$$G^T G m = G^T d \qquad \text{Eq. A37}$$

The result is the stress tensor m. It is not the precise magnitude of the stress but the relative magnitude of each principal stress.

Damped Solutions

The solution to the damped stress inversion problem is solved in matrix multiplication shown in Eq. A38. In Eq. A38, the damping matrix D contains the identity matrix for each stress tensor. The damping parameter e is to reduce the variations between the stress components among neighboring grids.

$$\left\{\mathbf{G}_{\mathrm{ALL}}^T \mathbf{G}_{\mathrm{ALL}} + e^2 \mathbf{D}^T \mathbf{D}\right\} \mathbf{m}_{\mathrm{ALL}} = \mathbf{G}_{\mathrm{ALL}}^T \mathbf{d}_{\mathrm{ALL}}, \qquad \text{Eq. A38}$$

The value of e is selected as a result of the best weighting value for both data misfit and model length. This value is chosen from the tradeoff curve at the common minimum values of both data misfit and model length. For example, in the trade-off curve in Fig. A18, the best weighting value is selected when both data misfit and model length are the minimum.

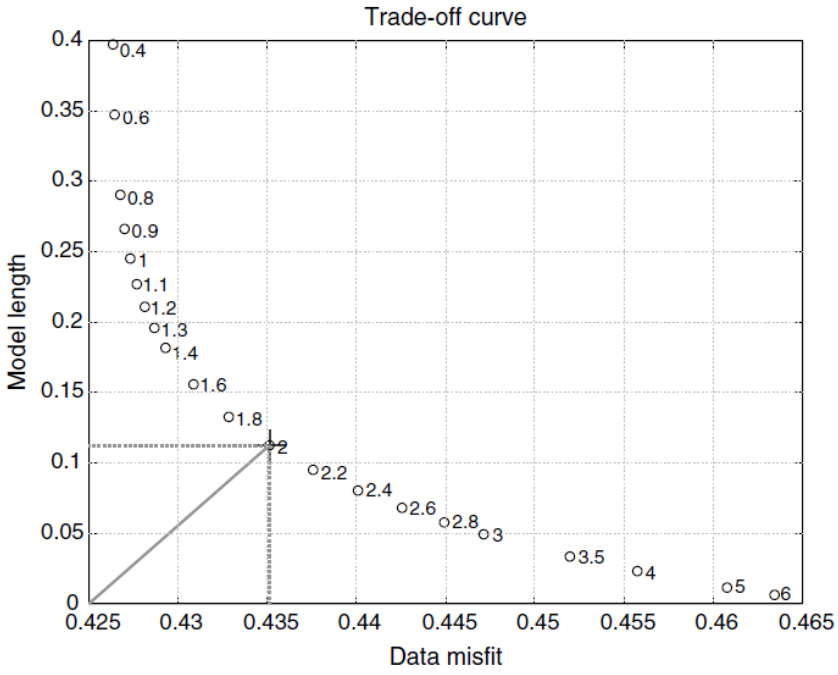

Fig. A18 The damping parameter e is found when the values of Data misfit and Model Length are at the minimum at the same time (MartíNez-Garzón et al., 2013).

Principal Stresses Directions Determination in MSASTI

A vertical plane is defined in geographic coordinates (G) by using its normal vector $\hat{n}$ and azimuth angle α. The α is measured from the north to the normal vector direction (Lund and John, 2007).

First a coordinate transfer tensor A_{SG} is defined to transfer normal vectors from geological coordinates to principal stress coordinates.

$$\mathbf{A}_{\mathbb{SG}} = \begin{pmatrix} \hat{\mathbf{s}}_1 \cdot \hat{\mathbf{g}}_1 & \hat{\mathbf{s}}_1 \cdot \hat{\mathbf{g}}_2 & \hat{\mathbf{s}}_1 \cdot \hat{\mathbf{g}}_3 \\ \hat{\mathbf{s}}_2 \cdot \hat{\mathbf{g}}_1 & \hat{\mathbf{s}}_2 \cdot \hat{\mathbf{g}}_2 & \hat{\mathbf{s}}_2 \cdot \hat{\mathbf{g}}_3 \\ \hat{\mathbf{s}}_3 \cdot \hat{\mathbf{g}}_1 & \hat{\mathbf{s}}_3 \cdot \hat{\mathbf{g}}_2 & \hat{\mathbf{s}}_3 \cdot \hat{\mathbf{g}}_3 \end{pmatrix} \quad \text{Eq. A39}$$

In the matrix A_{SG} in Eq. A40, the g is the base vector of geographic axes; s is the unit vector of principal stress coordinates. Thus, a normal vector with respect to the principal stresses is expressed as $\hat{n}s$.

$$\hat{\mathbf{n}}_{\mathbb{S}} = \mathbf{A}_{\mathbb{S}\mathbb{G}}\hat{\mathbf{n}}_{\mathbb{G}} = \begin{pmatrix} s_{1N}n_N + s_{1E}n_E \\ s_{2N}n_N + s_{2E}n_E \\ s_{3N}n_N + s_{3E}n_E \end{pmatrix} \qquad \text{Eq. A40}$$

$$\begin{aligned} \mathbf{s}_{\mathrm{n}} &= \left(\hat{\mathbf{n}}_{\mathbb{S}}^{T}\mathbf{S}_{\mathbb{S}}\hat{\mathbf{n}}_{\mathbb{S}}\right)\hat{\mathbf{n}}_{\mathbb{S}}, \\ &= \left[S_1(s_{1N}n_N + s_{1E}n_E)^2 + S_2(s_{2N}n_N + s_{2E}n_E)^2 \right. \\ &\quad \left. + S_3(s_{3N}n_N + s_{3E}n_E)^2\right]\hat{\mathbf{n}}_{\mathbb{S}} \\ &= S_n\hat{\mathbf{n}}_{\mathbb{S}}, \end{aligned} \qquad \text{Eq. A41}$$

In Eq. A41. s_n is the normal stress acting on the plan of the interest. In the SASTI program, the stress tensor Ss in Eq. A42 is not a complete stress tensor because the stress inversion result only gives a deviatoric stress tensor. Therefore, the deviatoric stress tensor D is used to calculate the horizontal component on the vertical plane. This results in the deviatoric stress in the horizontal direction of the vertical plane (Lund and John, 2007).

$$\mathbf{S}_{\mathbb{S}} = (S_1 - S_3)\begin{pmatrix} 1 & 0 & 0 \\ 0 & 1-R & 0 \\ 0 & 0 & 0 \end{pmatrix} + S_3\mathbf{I} = \mathbf{D} + S_3\mathbf{I}. \qquad \text{Eq. A42}$$

$$\mathbf{d}_{\mathrm{n}} = \left(\hat{\mathbf{n}}_{\mathbb{S}}^{T}\mathbf{D}\hat{\mathbf{n}}_{\mathbb{S}}\right)\hat{\mathbf{n}}_{\mathbb{S}}$$

$$= D_n\hat{\mathbf{n}}_{\mathbb{S}}. \qquad \text{Eq. A43}$$

Finally, the direction of the maximum horizontal stress can be found by taking the derivative of the magnitude of the horizontal stress equation in Eq. A44

Setting the derivative to 0 and two values can be found; one represents the minimum horizontal and another represents the maximum horizontal. Next, the second derivative is taken with respect to the angle to find the maximum horizontal stress magnitude. However, the magnitude cannot be determined. Instead, the angle at which the maximum horizontal stress is found in the direction of S_{Hmax} (Lund and John, 2007).

$$\alpha_{\mathrm{H}} = \begin{cases} \alpha & \text{if } S_n(\alpha) \text{ is a maximum} \\ \alpha + \pi/2 & \text{if } S_n(\alpha) \text{ is a minimum.} \end{cases} \qquad \text{Eq. A44}$$